

A Study of the  $^{12}\text{C}(\gamma, pd)$  reaction.

Thesis

submitted by

Stephen John McAllister

for the degree of

Doctor of Philosophy

Department of Physics and Astronomy,

University of Glasgow,

1997.

©S.McAllister, 1997.

ProQuest Number: 13818624

All rights reserved

INFORMATION TO ALL USERS

The quality of this reproduction is dependent upon the quality of the copy submitted.

In the unlikely event that the author did not send a complete manuscript and there are missing pages, these will be noted. Also, if material had to be removed, a note will indicate the deletion.



ProQuest 13818624

Published by ProQuest LLC (2018). Copyright of the Dissertation is held by the Author.

All rights reserved.

This work is protected against unauthorized copying under Title 17, United States Code  
Microform Edition © ProQuest LLC.

ProQuest LLC.  
789 East Eisenhower Parkway  
P.O. Box 1346  
Ann Arbor, MI 48106 – 1346

GLASGOW  
UNIVERSITY  
LIBRARY

GLASGOW UNIVERSITY  
LIBRARY

11318 (copy 1)

## Abstract

The work presented in this thesis describes the first experimental study of the  $^{12}\text{C}(\gamma, pd)$  reaction using tagged photons in the energy range 110MeV to 400MeV. The experiment was carried out using the MAMI-B c.w. electron accelerator at the Institut für Kernphysik, Mainz, Germany.

Bremsstrahlung photons were produced on a thin nickel foil and are tagged by momentum analysing the recoiling electrons using the Glasgow tagging spectrometer. The Tagger tags photons with an energy resolution of 2MeV and a photon flux of  $\sim 10^8\text{s}^{-1}$ . The  $^{12}\text{C}$  target was in the form of a 2mm thick graphite sheet. A plastic scintillator hodoscope PiP was used to detect the protons from the target and in three settings covered polar angles from  $22.7^\circ$  to  $156.7^\circ$  with a resolution of  $\sim 3.5^\circ$  and azimuthal angles from  $-22.8^\circ$  to  $+22.8^\circ$ . The coincident deuterons were detected in 3 banks of plastic time-of-flight(TOF) scintillator detectors, each made up of four layers. These were positioned opposite to PiP in a back-to-back two particle breakup kinematic configuration. The total TOF polar angle ranged from  $10.5^\circ$  to  $153.4^\circ$  with a resolution of  $\sim 2^\circ$ , and the azimuthal angle from  $162.5^\circ$  to  $192.7^\circ$ . The detector system has a missing energy resolution of  $\sim 6$  MeV for the  $(\gamma, pd)$  measurement allowing particle breakup from the  $(1p1p)$  shells and  $(1s1p)$  shells to be isolated.

Although  $2N$  absorption and quasifree pion production dominate photon absorption at intermediate energies there is some evidence in  $(\gamma, 2N)$  reactions of absorption on three correlated nucleons. This study of the photodisintegration of  $^{12}\text{C}$  has focussed on the coincident  $pd$  pairs which have been observed to be emitted with a strong back-to-back angular correlation. The similarity of this to the correlation observed in the dominant  $(\gamma, pn)$  yield (quasideuteron), suggests the possibility of a quasi- $^3\text{He}$  process, in which the photon is absorbed on a 3-nucleon

cluster. This is important because, under certain kinematic conditions, three-body exchange currents can be linked by gauge invariance to the corresponding three-body forces. However the photon interaction with a  $3N$  cluster may not be the only or even the major absorption mechanism, the reaction may be an initial  $(\gamma, pn)$  event followed by  $(n, d)$  pickup in some final state interaction. The  $(\gamma, pd)$  reaction is an interesting but small part of the total photoabsorption cross-section and knowledge of the relative importance of the reaction mechanisms will provide constraints on microscopic theories.

The analysis of the experimental data, together with comparisons to measurements of other related photoreactions and predictions from Monte Carlo calculations have shown that the reaction mechanism is consistent with having some direct contributing process, similar to that observed in  ${}^3\text{He}$  two-body breakup.

## Declaration

The data presented in this thesis were obtained by the Experimental Nuclear Physics group at the University of Glasgow in collaboration with colleagues from the Nuclear Physics groups at the Universities of Edinburgh, Tübingen and Mainz. The experiment was performed at the Institut für Kernphysik at the University of Mainz. I participated fully in the execution of the experiment. The analysis and interpretation of the experimental data is entirely my own work. This thesis was composed by myself.

## Acknowledgements

I would first of all like to thank EPSRC for providing me with my research grant and the travelling expenses needed for carrying out the experiment in Germany. I would also like to thank Prof. Saxon, the head of the Physics Department at the University of Glasgow, for the additional funding he supplied to attend overseas conferences. I would also like to express my gratitude to Prof. Bob Owens, not only for his invaluable physics thoughts but also for the support provided towards the end of my studentship, which was greatly appreciated.

I would also like to say a big thankyou to my overseas collaborators, Peter Grabmayr, Torsten Hehl, Ralf Schneider, Tomas Lamparter, and Karen Spaeth with whom I spent many a long night-shift and whose subsequent help in matters of analysis was indispensable. Thanks is also due to my colleagues from Edinburgh, Derek Branford, John MacKenzie, Doug Johnstone and Tom Davinson for their help in setting up and running the experiment.

It is my pleasure to take this opportunity to thank all the members of the Glasgow University Nuclear Physics group for all their help and advice throughout my three (or four!) years of study. I have thoroughly enjoyed my time working within this group, and would probably not have got this far if it was not for the friendship and humour of those working with me.

I should single out a few souls for special thanks. Firstly to John Annand, without whom it can be safely said the experiment would never have been carried out. To Ian Anthony and Andy Sibbald for maintaining the computer system so effortlessly and for putting up with me knocking on their door, right on cue once a month when my quota ran out. I should also thank Scott Lumsden, but he supports Motherwell and really just needs my sympathy.

To Prof. Owens and Dr Douglas MacGregor whose patient reading of the text and subsequent thoughts improved this thesis immeasurably. My supervisor

Dr Cameron McGeorge is owed the biggest vote of thanks, along with Dr Peter Harty. Together they have taught me anything that I have learned in my time spent in the group and were always there to patiently answer even my most stupid questions. Without them I would never have completed the thesis and I am deeply grateful.

I should lastly thank my office mates, past and present, Dan Watts, who is unique in every way and will be glad to see the back of me, Tony Yau and Peter Clive. I hope we will all remain friends in the future. To various characters from other groups in the department, Paul McCallum, Andy Wood, Suzie Martland and all the 'lads' downstairs, Calum, Farouq, Iskender, Ken, Stefan, and Robin. I finally want to say a big thanks to my family and to Jacqui, without their encouragement I would have given up long ago. I want to dedicate this thesis to my Dad who will never be able to read it but who will nevertheless be the keenest to find out what its all about.

# Contents

<b>1</b>	<b>Introduction</b>	<b>1</b>
1.1	The Photon as a Probe of the Nucleus . . . . .	3
1.2	Photon Tagging Techniques . . . . .	4
1.3	The Total Photon Absorption Cross Section . . . . .	5
1.4	Review of Experiment and Theory . . . . .	7
1.4.1	Early Photonuclear Reaction Models . . . . .	7
1.4.2	Testing the Early Models . . . . .	9
1.5	Recent Theoretical Developments . . . . .	12
1.6	Motivation and aims of the Present Work . . . . .	13
1.6.1	Previous Measurements of the ( $\gamma$ ,pd) Reaction . . . . .	15
1.6.2	The Two-Body Breakup of $^3\text{He}$ . . . . .	15
1.6.3	Three-body Breakup of $^3\text{He}$ . . . . .	18
1.6.4	$^{12}\text{C}$ and $^{16}\text{O}$ . . . . .	21
1.6.5	Microscopic $^3\text{He}$ Photodisintegration Calculations . . . . .	22
1.6.6	Aims of Present Work . . . . .	24
<b>2</b>	<b>Experimental Apparatus</b>	<b>26</b>
2.1	Introduction . . . . .	27
2.2	The Mainz Microtron . . . . .	27
2.2.1	The Race Track Microtron . . . . .	27

2.2.2	MAMI-B . . . . .	28
2.3	Photon Production and Tagging . . . . .	30
2.3.1	The Glasgow Tagging Spectrometer . . . . .	31
2.3.2	The Focal Plane Detector (FPD) . . . . .	31
2.3.3	Photon Beam Collimation and Tagging Efficiency . . . . .	33
2.4	The Targets . . . . .	35
2.5	The Particle Detectors . . . . .	37
2.5.1	The $\Delta E$ Detector . . . . .	41
2.5.2	PiP . . . . .	42
2.5.3	TOF . . . . .	44
2.6	Data Acquisition . . . . .	44
2.6.1	Event Information in PiP/TOF . . . . .	45
2.6.2	Trigger Electronics . . . . .	46
2.6.3	The First Level Trigger . . . . .	47
2.6.4	The Second Level Trigger . . . . .	48
2.6.5	The Acquisition System . . . . .	51
<b>3</b>	<b>Detector Calibrations</b> . . . . .	<b>52</b>
3.1	General Concepts . . . . .	53
3.1.1	Pedestals . . . . .	53
3.1.2	Relation between pulse charge and number of scintillation photons . . . . .	54
3.1.3	Replacement QDCs . . . . .	55
3.1.4	Thresholds . . . . .	56
3.1.5	Discriminator Walk Corrections . . . . .	57
3.1.6	Position . . . . .	58
3.2	The Start Detector . . . . .	58

3.3	The Tagger . . . . .	60
3.4	PiP . . . . .	60
3.4.1	Position Calibration . . . . .	61
3.4.2	Energy Calibration: the relation between pulse height and particle energy . . . . .	62
3.5	TOF . . . . .	65
3.5.1	Position Calibration . . . . .	66
3.5.2	Time of Flight . . . . .	67
3.5.3	Gain matching . . . . .	68
3.6	Detector Performance . . . . .	69
3.6.1	Missing energy . . . . .	69
<b>4</b>	<b>Data Analysis</b>	<b>76</b>
4.1	PiP Proton Selection . . . . .	77
4.2	TOF Deuteron Selection . . . . .	79
4.2.1	Neutron selection . . . . .	82
4.3	Deuteron Energy Loss Correction . . . . .	82
4.4	Dealing with Randoms . . . . .	82
4.4.1	Dealing with Randoms in the tagger . . . . .	83
4.4.2	Randoms in the TOF Detector . . . . .	84
4.5	Tagging Efficiencies . . . . .	84
4.6	Subevents . . . . .	84
4.7	Background Corrections . . . . .	86
4.8	Cross Section Derivations . . . . .	87
4.9	Experimental Uncertainties . . . . .	87
4.9.1	Statistical Uncertainties . . . . .	87
4.9.2	Systematic Uncertainties . . . . .	88

4.10	Monte Carlo Simulations of the Experiment . . . . .	89
4.10.1	3N Photon Absorption Model . . . . .	89
4.10.2	The ${}^3\text{He}(\gamma, pd)$ cross section . . . . .	90
4.10.3	The Pickup Model . . . . .	91
<b>5</b>	<b>Results and Discussion</b>	<b>92</b>
5.1	Introduction . . . . .	93
5.2	Missing Energy . . . . .	95
5.3	Missing Momentum . . . . .	101
5.4	Photon Energy Dependence . . . . .	111
5.5	Angular Distributions . . . . .	113
5.6	Monte Carlo Simulations . . . . .	123
5.6.1	Missing Energy Distributions . . . . .	123
5.6.2	Recoil Momentum Distributions . . . . .	125
5.6.3	Momentum Difference . . . . .	133
5.7	Summary . . . . .	134
<b>6</b>	<b>Conclusions and Outlook</b>	<b>141</b>
6.1	Conclusions . . . . .	142
6.2	Outlook . . . . .	143
<b>A</b>	<b>F(P) Distributions</b>	<b>146</b>
A.1	Introduction . . . . .	147
A.2	The Radial Wavefunction . . . . .	147
A.3	The Wavefunction in Momentum Space . . . . .	147
A.4	Mixing Three Wavefunctions . . . . .	151
A.4.1	Three $p_{\frac{3}{2}}$ Shell Particles . . . . .	151
A.4.2	Mixing Two $p_{\frac{3}{2}}$ Particles with an $s_{\frac{1}{2}}$ Shell Particle . . . . .	154

A.5 Wavefuctions . . . . .	156
<b>B Table of Results</b>	<b>157</b>

# List of Figures

1.1	Total photon absorption cross section per nucleon . . . . .	6
1.2	Missing energy spectra of $^{12}\text{C}(\gamma, pn)$ and $^{12}\text{C}(\gamma, pp)$ . . . . .	10
1.3	Saskatoon results compared with earlier measurements. . . . .	16
1.4	Angular distributions from Saskatoon . . . . .	17
1.5	Daphne angular distributions . . . . .	19
1.6	Daphne angular distributions . . . . .	20
1.7	One, Two and Three-body force diagrams . . . . .	23
2.1	Schematic diagram of a racetrack microtron . . . . .	28
2.2	The MAMI-B facility . . . . .	29
2.3	Schematic of photon tagging . . . . .	30
2.4	Schematic of the tagging spectrometer . . . . .	32
2.5	Schematic view of the photon beam line . . . . .	34
2.6	Target orientations . . . . .	37
2.7	The experimental setup for PiP at FORWARD angle . . . . .	38
2.8	The experimental setup for PiP at CENTRE angle . . . . .	39
2.9	The experimental setup for PiP at BACKWARD angle . . . . .	40
2.10	A schematic of the $\Delta E$ Detector ring . . . . .	41
2.11	A schematic of PiP . . . . .	42
2.12	Another view of PiP . . . . .	43
2.13	Schematic of a TOF detector stand . . . . .	45

2.14	The First Level Trigger decoder . . . . .	47
2.15	The Second Level Trigger decoder . . . . .	49
2.16	$\Delta E$ - $E$ particle identification . . . . .	49
3.1	Determining the parameters needed for the reconstruction of miss- ing QDC's . . . . .	56
3.2	Pedestal and discriminator threshold . . . . .	56
3.3	The effect of 'Walk' . . . . .	57
3.4	Application of the start correction to the $\Delta E_{start}$ . . . . .	59
3.5	Tagger time spectrum . . . . .	61
3.6	Position calibration parameters . . . . .	62
3.7	Cosmic muons for gain monitoring . . . . .	64
3.8	Calculated proton energy (MeV) from deuterium kinematics vs the prot on energy measured by PiP in MeV. . . . .	65
3.9	TOF position calibration . . . . .	66
3.10	TOF $t_{zero}$ time-of-flight spectrum . . . . .	68
3.11	$CD_2(\gamma, pn)$ missing energy spectrum . . . . .	70
3.12	deuterium ridge cut on missing energy . . . . .	71
3.13	Proton energy resolution from $E_\gamma, \theta_n$ . . . . .	72
3.14	PiP polar angular resolution from $E_\gamma, \theta_n$ . . . . .	73
3.15	Neutron energy resolution from $E_\gamma, \theta_n$ . . . . .	74
4.1	Proton identification and selection. . . . .	79
4.2	Deuteron identification and selection. . . . .	81
4.3	Prompt and random regions in the tagger time spectrum . . . . .	83
4.4	tagging Efficiency as a function of Photon energy . . . . .	85
5.1	Opening Angle distributions for the $^{12}\text{C}(\gamma, pd)$ reaction in the cen- tre of momentum frame of the photon and a stationary $^3\text{He}$ . . . . .	94

5.2	Missing energy distributions for the $^{12}\text{C}(\gamma,\text{pd})$ reaction at central proton angles. . . . .	97
5.3	Missing energy distributions for the $^{12}\text{C}(\gamma,\text{pn})$ and $(\gamma,\text{pp})$ reactions	98
5.4	Missing energy distributions for the $^{12}\text{C}(\gamma,\text{pd})$ reaction at the backward PiP angle detector geometry . . . . .	99
5.5	Missing energy distributions for the $^{12}\text{C}(\gamma,\text{pd})$ reaction at the forward PiP angle detector geometry . . . . .	100
5.6	Superposition of the missing energy distributions for each detector setting for the $^{12}\text{C}(\gamma,\text{pd})$ reaction. . . . .	102
5.7	Recoil momentum distributions for the $^{12}\text{C}(\gamma,\text{pd})$ reaction at the central PiP angle detector geometry for low missing energy, $E_m < 44$ MeV. . . . .	104
5.8	Recoil momentum distributions for the $^{12}\text{C}(\gamma,\text{pd})$ reaction at the backward PiP angle detector geometry for low missing energy, $E_m < 44$ MeV. . . . .	106
5.9	Recoil momentum distributions for the $^{12}\text{C}(\gamma,\text{pd})$ reaction at the forward PiP angle detector geometry for low missing energy, $E_m < 44$ MeV. . . . .	107
5.10	Recoil momentum distributions for the $^{12}\text{C}(\gamma,\text{pd})$ reaction at the backward PiP angle detector geometry for higher missing energy, $44 \leq E_m \leq 70$ MeV . . . . .	108
5.11	Recoil momentum distributions for the $^{12}\text{C}(\gamma,\text{pd})$ reaction at the central PiP angle detector geometry for higher missing energy, $44 \leq E_m \leq 70$ MeV . . . . .	109
5.12	Recoil momentum distributions for the $^{12}\text{C}(\gamma,\text{pd})$ reaction at the forward PiP angle detector geometry for higher missing energy, $44 \leq E_m \leq 70$ MeV . . . . .	110

5.13	Photon energy dependencies. . . . .	112
5.14	$^{12}\text{C}(\gamma, pd)$ for missing energy $E_m < 44$ MeV. . . . .	115
5.15	$^{12}\text{C}(\gamma, pd)$ for missing energy 44-70MeV . . . . .	116
5.16	$^{12}\text{C}(\gamma, pn)$ data with missing energy $E_m < 40$ MeV. . . . .	117
5.17	$^{12}\text{C}(\gamma, pn)$ data with missing energy 40-70MeV . . . . .	118
5.18	$^{12}\text{C}(\gamma, pp)$ data with missing energy $E_m < 40$ MeV. . . . .	119
5.19	$^{12}\text{C}(\gamma, pp)$ data with missing energy 40-70MeV . . . . .	120
5.20	Comparison of angular distribuitons . . . . .	122
5.21	Missing energy distributions for the $^{12}\text{C}(\gamma, pd)$ reaction at central proton angles compared to the pickup model calculation. . . . .	124
5.22	Model predictions of the recoil momentum distributions . . . . .	126
5.23	Model predictions of the recoil momentum distributions . . . . .	127
5.24	Model predictions of the recoil momentum distributions . . . . .	128
5.25	Model predictions of the recoil momentum distributions . . . . .	129
5.26	Model predictions of the recoil momentum distributions . . . . .	130
5.27	Model predictions of the momentum difference distributions . . .	135
5.28	Model predictions of the momentum difference distributions . . .	136
5.29	Model predictions of the momentum difference distributions . . .	137
5.30	Model predictions of the momentum difference distributions . . .	138
5.31	Model predictions of the momentum difference distributions . . .	139
5.32	Model predictions of the momentum difference distributions into $4\pi$ . . . . .	140
A.1	Single particle distributions. . . . .	149
A.2	Single particle distributions. . . . .	150
A.3	Single particle distributions. . . . .	153
A.4	Single particle distributions. . . . .	155

# List of Tables

2.1	The targets. . . . .	36
2.2	Dimensions of the PiP E blocks . . . . .	44
3.1	Summary of detector performance . . . . .	75
B.1	$(\gamma, \text{pd})$ cross sections for $E_\gamma=175$ MeV and $E_m < 44$ MeV . . . . .	158
B.2	$(\gamma, \text{pd})$ cross sections for $E_\gamma=225$ MeV and $E_m < 44$ MeV . . . . .	159
B.3	$(\gamma, \text{pd})$ cross sections for $E_\gamma=275$ MeV and $E_m < 44$ MeV . . . . .	160
B.4	$(\gamma, \text{pd})$ cross sections for $E_\gamma=325$ MeV and $E_m < 44$ MeV . . . . .	161
B.5	$(\gamma, \text{pd})$ cross sections for $E_\gamma=375$ MeV and $E_m < 44$ MeV . . . . .	162
B.6	$(\gamma, \text{pd})$ cross sections for $E_\gamma=175$ MeV and $E_m=44-70$ MeV . . . . .	163
B.7	$(\gamma, \text{pd})$ cross sections for $E_\gamma=225$ MeV and $E_m=44-70$ MeV . . . . .	164
B.8	$(\gamma, \text{pd})$ cross sections for $E_\gamma=275$ MeV and $E_m=44-70$ MeV . . . . .	165
B.9	$(\gamma, \text{pd})$ cross sections for $E_\gamma=325$ MeV and $E_m=44-70$ MeV . . . . .	166
B.10	$(\gamma, \text{pd})$ cross sections for $E_\gamma=375$ MeV and $E_m=44-70$ MeV . . . . .	167

# Chapter 1

## Introduction

The subject of this thesis is the study of the  $^{12}\text{C}(\gamma, \text{pd})$  reaction at photon energies between 110 and 400 MeV. This is an interesting reaction because it has already been shown that three-body forces play an important role in the  $^3\text{He}(\gamma, \text{pn})$ [1],  $^3\text{He}(\gamma, \text{pp})$ [2, 4] and  $^3\text{He}(\gamma, \text{pd})$ [5] reactions. The study of three nucleon interactions in heavier nuclei is more difficult but one way is to study the  $(\gamma, \text{pd})$  reaction which may yield more information about the nature of three body forces and reveal something about the cluster states of the nucleus. In this chapter the background to the present investigation is reviewed by introducing some theoretical concepts as well as outlining some previous experimental work. The motivation for the present study is described within this context.

The atomic nucleus is a collection of protons and neutrons bound together by the strong nuclear interaction and the nature of this basic interaction between nucleons is of great interest to nuclear physicists. A large part of the structure of atomic nuclei can be described by the nuclear shell model theory. In analogy with the atomic shell model, each nucleon moves as an independent particle in a potential well generated by the other nucleons in the nucleus leading to an orbit picture in which the nucleons move around in well defined states. This is at first a surprising picture because it is not clear how such strongly interacting particles can go around the nucleus in complete orbits without colliding with each other. The independent particle motion description of the nucleus is only possible because of the Pauli exclusion principle which limits the available final states in the nucleus into which nucleons can scatter. With the further inclusion of a spin-orbit interaction, the shell model successfully accounts for many properties of nuclei.

The shell model is a macroscopic mean field theory of the nucleus reproducing nuclear properties which depend on the average properties of all the nucleons such as binding energies and the magic numbers associated with shell closures.

However, it does not provide realistic information about the short range correlations between nucleons at a microscopic level. The nucleon-nucleon interaction is thought to be mediated by the exchange of virtual mesons and many microscopic theories attempt to incorporate this explicitly in order to derive a more realistic nucleon-nucleon potential in contrast to the mean field potential defined by the nuclear shell model. Photonuclear reaction studies provide important tests of microscopic models incorporating explicit meson exchange currents and short range correlations. Work in this field has already confirmed features beyond the long range shell model description.

## 1.1 The Photon as a Probe of the Nucleus

The interaction of a photon with a nucleus is electromagnetic in nature and is, in principle, calculable to good accuracy therefore removing any uncertainty in the interpretation of experimental results arising from the interaction of the probe. The electromagnetic coupling between the photon and the nucleus is weak, enabling the photon to explore the entire volume of the nucleus without distorting it significantly. This is a major advantage over nucleonic probes which couple strongly to the nucleus resulting mostly in surface absorption. The photon is therefore able to interact with all of the main features of the nucleus, the nucleons themselves, the mesonic currents and the nucleon resonances formed by the excitation of individual nucleons. The relative weakness of the electromagnetic interaction however means small reaction cross sections and it is experimentally time-consuming to obtain good statistical accuracy.

## 1.2 Photon Tagging Techniques

Many early experiments employed techniques of photon production which did not measure the photon energy and so a full reconstruction of the photoreaction kinematics was not possible. The problem of producing intense high energy photon beams of known energy has been overcome by the photon tagging technique. Three main schemes for the production and tagging of photon beams are discussed below. In all three an initial electron or positron beam of known energy is used to produce the photon beam and one of the products of the interaction is detected in order to determine the photon energy.

- Positron Annihilation-in-flight;  $e^+ + e^- \rightarrow \gamma + \gamma$

A beam of positrons is produced from electron bremsstrahlung by pair production in a high  $Z$  target and momentum analysed to determine its energy. The positron beam is then passed through a low  $Z$  radiator in which positron annihilation with atomic electrons produces pairs of photons of equal energy in the center of mass frame. In the laboratory frame one photon generally has a higher energy than the other. The low energy photons are detected in coincidence with the reaction products, and from their laboratory angle the energy of the corresponding high energy photon, which interacts with the target, can be determined.

- Laser Backscattering;  $e^- + \gamma \rightarrow e^{-'} + \gamma'$

Low energy photons are produced by a laser and are then collided with a high energy electron beam. The laser photon undergoes inverse Compton scattering (inverse because the electron loses energy to the photon), gaining in energy due to the large electron momentum and the scattered photon emerges in a direction close to that of the electron beam. Detection and energy measurement of the recoil electron in coincidence with the reaction

products determines the energy of the scattered photon.

- Bremsstrahlung;  $e^- \rightarrow e^-' + \gamma + \text{nuclear recoil}$

In this process a high energy electron beam is passed through a thin radiator producing an intense forward peaked cone of bremsstrahlung photons. A measurement of the recoil electron energy determines the photon energy. This is the method employed in the present experiment and is discussed in more detail in section (2.3).

### 1.3 The Total Photon Absorption Cross Section

In investigating nuclear interactions one has to successfully resolve the details of interest and this implies using a probe of wavelength comparable in size to that of the particular feature and so the character of any photoreaction will vary with photon energy. This is illustrated in figure 1.1 absorption cross section per nucleon as a function of photon energy for various elements [41]. If the photon interacts with a body of size comparable to that of its wavelength then at around 10 MeV it sees the whole nucleus as a single entity, and as an ensemble of nucleons, mesons and resonances above  $\sim 100$  MeV. This explains why the cross section per nucleon is approximately the same for all complex nuclei between about 100 MeV and 1.5 GeV and why figure 1.1 is sometimes referred to as a universal curve.

Between about 10 and 30 MeV the cross section is dominated by collective excitations of the whole nucleus when the photon is mainly absorbed by electric dipole transitions within the nucleus, resulting in an oscillation of the protons relative to the neutrons. This effect, called the giant dipole resonance, is dependent upon the nuclear structure and is successfully described by collective models.

The second major peak in the cross section occurs at around 300 MeV and is known as the  $\Delta$ -resonance region. It arises from the excitation of the nucleon

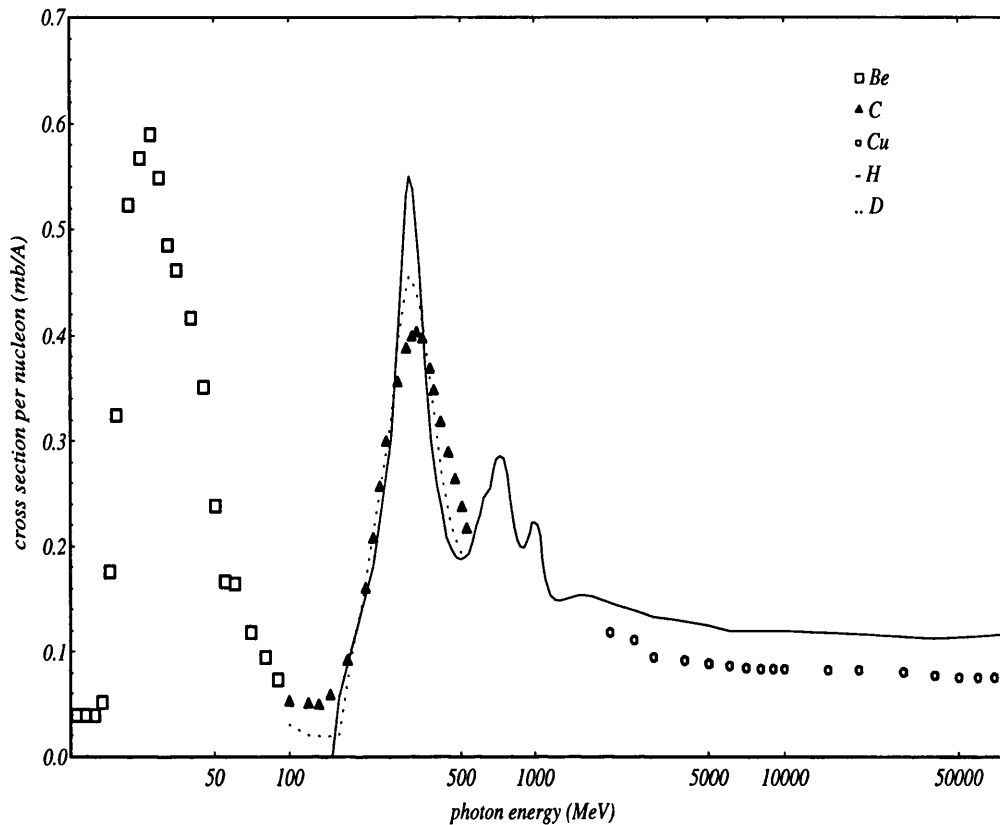


Figure 1.1: *Total photon absorption cross section per nucleon*

to its first excited state, the  $\Delta$  (1232) resonance, part of its width in a nucleus arising from the Fermi motion of the nucleons. This excitation is the result of the interaction between the photon's electromagnetic field and the quark constituents of the nucleon and decays to a pion and a nucleon. The higher resonances of the proton shown on figure 1.1 are not evident for complex nuclei and are perhaps washed out by the Fermi motion or by Pauli blocking of the decay nucleons.

In the intermediate range of photon energies between  $\sim 50$  and  $\sim 200$  MeV the cross section is relatively weak and has been shown to arise mainly from the absorption of the photon by two interacting nucleons [17, 18, 19, 20, 21]. Conservation of momentum suppresses the photon absorption on a single nucleon and the photon is instead absorbed on a correlated proton-neutron pair. This

basic assumption has led to the development of the Quasideuteron Model[6] which describes the general features of the cross section in this intermediate energy region.

## 1.4 Review of Experiment and Theory

### 1.4.1 Early Photonuclear Reaction Models

The earliest intermediate energy photonuclear experiments [7, 8] found that the spectrum of photoprotons produced had distinct characteristics depending on the photon energy. Low energy photons produced low energy protons with a weak angular dependence. This phenomenon is successfully accounted for by the Giant Dipole Resonance when the collective excitation of the nucleus de-excites via the emission of a nucleon. However, higher energy photons produced a strongly forward peaked distribution of protons. It was suggested[9] that this high energy characteristic results from the absorption of the photon on a single nucleon which explained the angular distribution but not the momentum of some of the produced protons, which required the initial nucleon momenta to be far greater than the Fermi momentum. Levinger[6] however proposed that the photon was instead absorbed on a nucleon pair, leading to the development of the quasi-deuteron model (QD). He argued that for the proton to have a large momentum in the initial state it must have been close to another nucleon to interact with a strong mutual force. This model assumes that the pair is proton-neutron in order to provide an electric dipole to which the photon can couple while the residual  $(A-2)$  nucleons act as spectators to the reaction. In this phenomenological model the  $(\gamma, pn)$  cross section  $\sigma_{QD}$  is parameterised in terms of the free deuteron cross

section  $\sigma_D$  in the following way

$$\sigma_{QD}(E_\gamma) = L \frac{NZ}{A} \sigma_D(E_\gamma) \quad (1.1)$$

where  $\frac{NZ}{A}$  corresponds to the density of the quasideuteron pairs. The Levinger parameter  $L$  represents the relative probability of two nucleons interacting with each other in a complex nucleus compared with that in a free deuteron. Levinger calculated this parameter to be 6.4 for 150 MeV photons on carbon, however the experimental estimation of the value from fits of equation 1.1 to the total photon absorption cross sections produced widely varying results[10, 11, 12, 13]. The original model does not take into account the effects of Pauli blocking or of final state interactions (FSI).

A more sophisticated model was proposed by Gottfried[16] who showed that the cross section for the photoproduction of correlated neutron proton pairs could be factorised as

$$d\sigma = \frac{1}{(2\pi)^4} F(P) S_{fi} d^3 k_1 d^3 k_2 \quad (1.2)$$

where  $k_1$  and  $k_2$  are the momenta of the ejected nucleons. The factor  $F(P)$  is proportional to the probability of finding two nucleons at zero separation with momentum  $P = |k_1 + k_2 - \omega|$ , where  $\omega$  is the incident photon momentum.  $F(P)$  can be derived from the shell model wavefunctions of the initial nucleons. The factor  $S_{fi}$  is analogous to the free deuteron cross section in the QD model and explicitly contains the details of the short range correlations (SRC), the change in the nuclear wavefunctions produced by the forces between nucleons at much closer than average separation. The factorisation of the  $(\gamma, pn)$  cross section into the above form assumes that the residual excitation energy is small compared to the photon energy, that the other nucleons do not influence the reaction, that three nucleon effects can be ignored and that the ground state wavefunction of the bound pair is the product of short range pair correlation functions and the Slater

determinant of the shell model wavefunctions of the pair. It further assumes that the photon is absorbed by a  $pn$  pair in a relative  ${}^3S_1$  state.

### 1.4.2 Testing the Early Models

Early photonuclear experiments [10, 11, 12, 13] utilising the untagged bremsstrahlung technique to determine the photon energy provided qualitative confirmation of the QD model by confirming the frequent emission of correlated proton-neutron pairs. The average  $pn$  opening angle was the similar to that for the deuteron in a number of light elements while the opening angle distributions in these light elements were wider than that in the deuteron, due to the initial momentum of the nucleon pair.

The advent of high duty cycle accelerators and the use of tagged photons significantly improved the quality of the experimental data allowing a complete reconstruction of the reaction kinematics. The Glasgow group in collaboration with Edinburgh, Mainz and Tübingen Universities [17, 18, 19, 20, 21, 22] investigated the  $(\gamma, NN)$  reaction on  ${}^4\text{He}$ ,  ${}^6\text{Li}$ ,  ${}^{12}\text{C}$  and  ${}^{16}\text{O}$  in the photon energy range 80 MeV to 157 MeV with a missing energy resolution of  $\sim 7$  MeV enabling them to identify the shells from which the nucleons were emitted. The most extensive measurements were made on  ${}^{12}\text{C}$  and some missing energy ( $E_m$ ) spectra obtained for  ${}^{12}\text{C}(\gamma, pn)$  and  ${}^{12}\text{C}(\gamma, pp)$  are shown in figure 1.2. The  $(\gamma, pn)$  reaction shows a peak near the reaction threshold indicating that the residual nucleus is often left in or near the ground state. For the  $(\gamma, pn)$  case, the shape of the missing energy spectra can be simulated by folding together two single nucleon missing energy spectra obtained from high resolution  $(e, e'p)$  experiments on  ${}^{12}\text{C}$  [19]. This supports the view that the residual nucleus acts as a spectator during the reaction. The results of a simulation based on the spectator model and the relative strengths of the  $s$  and  $p$  shells calculated from the number of nucleons in

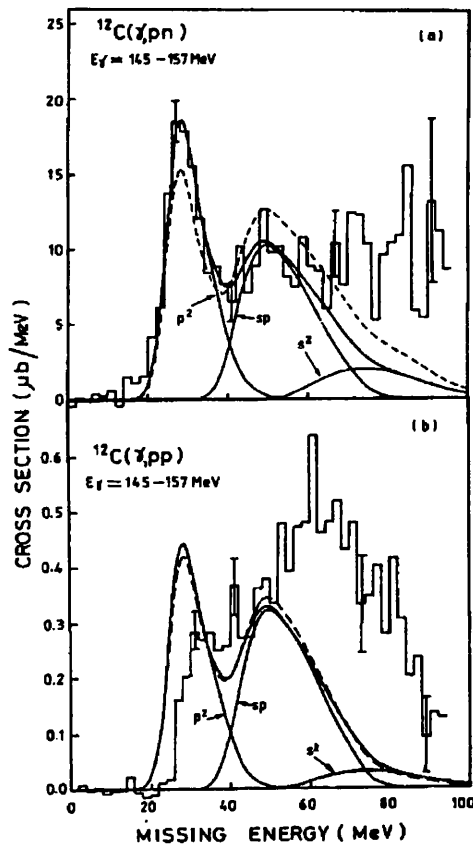


Figure 1.2: Missing energy spectra of  $^{12}\text{C}(\gamma, pn)$  and  $^{12}\text{C}(\gamma, pp)$  for  $E_\gamma = 145-157 \text{ MeV}$ . The smooth lines are the result of folding together spectra from high resolution  $^{12}\text{C}(e, e'p)$  data. The dashed lines are the calculated  $pp, sp$  and  $ss$  absorption strengths at  $E_\gamma = 151 \text{ MeV}$  [19].

each shell is shown by the smooth solid line. For the dashed line the relative  $pp$ ,  $sp$  and  $ss$  absorption strengths calculated by Ryckebusch [23] at  $E_\gamma = 151 \text{ MeV}$  are used.

The  $(\gamma, pp)$  reaction shows no evidence of a peak at threshold and coupled with the results of the simulation suggests that most of the strength does not originate from direct absorption on proton-proton pairs. Neither assumption about the relative strength of  $pp$ ,  $sp$  and  $ss$  absorption succeeds in reproducing the shape of the missing energy spectrum. The observed strength at higher missing energies indicates that the recoil system is left in an excited state. This can arise from FSI

following a  $(\gamma, pn)$  reaction or the onset of virtual pion mechanisms, which are located at high missing energy, such as  $(\gamma, N\pi)$  followed by  $(\pi, 2N)$  or  $(N, 2N)$  which can result in the emission of a third undetected particle.

The observed recoil momentum spectra from the  $(\gamma, pn)$  and to some extent the  $(\gamma, pp)$  reaction can also be described by a simulation based on the spectator model [19]. The spectator model was tested quantitatively by comparing the predicted pn pair momentum distribution from Gottfried's factorised framework,  $\mathbf{P}^2\mathbf{F}(\mathbf{P})$ , with the observed recoil momentum spectra from the  $^{12}\text{C}(\gamma, pn)$  reaction. The measured recoil momentum is derived from

$$\mathbf{P}_{recoil} = \mathbf{P}_\gamma - \mathbf{P}_p - \mathbf{P}_n = -\mathbf{P} \quad (1.3)$$

where  $\mathbf{P}_{\gamma,p,n}$  are respectively the measured photon, proton and neutron momenta. In this model, assuming there are no FSI, the momentum of the recoiling system is equal and opposite to the initial momentum of the nucleon pair in the nucleus.  $\mathbf{F}(\mathbf{P})$  was derived from harmonic-oscillator nucleon wavefunctions [14] and is sensitive to the shells from which the two nucleons emerge. The direction of the initial pn pair was assumed to be isotropic. For absorption on two p-shell nucleons

$$\mathbf{F}_{1p1p}(\mathbf{P}) = \frac{8}{15\sqrt{2}\beta^3\pi} \left( 3 - \frac{\mathbf{P}^2}{\beta} + \frac{\mathbf{P}^4}{4\beta^2} \right) \exp\left(-\frac{\mathbf{P}^2}{2\beta}\right) \quad (1.4)$$

and if one nucleon was originally in the s-shell

$$\mathbf{F}_{1p1s}(\mathbf{P}) = \frac{2}{3\sqrt{2}\beta^3\pi} \left( \frac{\mathbf{P}^2}{\beta} \right) \exp\left(-\frac{\mathbf{P}^2}{2\beta}\right) \quad (1.5)$$

The parameter  $\beta$  has the value  $0.302\text{fm}^{-2}$  for  $^{12}\text{C}$  in order to give the correct rms radius.

One important finding from these measurements is the absence of any significant tail of events with large recoil momenta which indicates that FSI do not introduce significant distortion to the measured events, since large recoil momenta

and missing energies are likely to be caused by final state scattering and energy loss [19]. The factorised form of the cross section has been extremely successful in qualitatively and quantitatively describing the experimental results.

The strength of final state nucleon absorption, was investigated by Harty [24] *et al.* who made a comparison of the  $^{12}\text{C}(\gamma, pn)$  and  $^{12}\text{C}(\gamma, p)$  reaction yields. The results provide an estimate of the neutron transmission in  $^{12}\text{C}$ . An average transmission of  $\sim 0.80 \pm 0.08$  was found for neutrons of energies 20-45MeV. This indicates that final state absorption is a relatively small effect in this energy range.

## 1.5 Recent Theoretical Developments

More recent theoretical models have moved away from the models of Levinger and Gottfried in an attempt to understand the 2N absorption mechanism on a microscopic level. The validity of the factorised approach taken by Gottfried has been tested by Ryckebusch [25] *et al.* Their calculations include the effects of the different meson exchange currents and the isobar current. The two-body terms seagull, pion-in-flight and delta-excitation were not considered in the earlier models where it was assumed that the photon coupled to one nucleon which shared its momentum with a second through short range correlations. They showed that absorption on singlet pairs was not negligible but that the factorised approach was justifiable at higher energies where the  $\Delta$  resonance becomes more dominant and the pn pairs seem to behave more like quasideuterons. Their calculations have been extended to include some FSI effects and have shown that the main effect is a reduction in the cross section and not a distortion of the angular distribution. This group have recently extended their calculations to include the effect of heavier  $\rho$ -meson exchange currents which further reduce the

magnitude of the cross section through interference effects with the other two-body mechanisms. They suggest that the angular distributions of the outgoing nucleons are particularly sensitive to the contributing meson exchange currents. This has been confirmed in a study by Yau *et al.* [51] which examined the angular distributions of  $^{12}\text{C}(\gamma, \text{NN})$  reactions and observed effects beyond one pion exchange.

## 1.6 Motivation and aims of the Present Work

Although previous experiments have confirmed that 2N mechanisms dominate at intermediate photon energies a previous unpublished study of the photodisintegration of  $^{12}\text{C}$  by the Glasgow group, in the photon energy range 133-158 MeV, observed a significant number of coincident proton-deuteron pairs with a strong back-to-back angular correlation. The similarity of this to the correlation observed in the dominant  $(\gamma, \text{pn})$  yield (quasideuteron), suggests the possibility of a quasi- $^3\text{He}$  process, in which the photon is absorbed on a  $^3\text{He}$  cluster inside the  $^{12}\text{C}$  nucleus, suggesting a strong interaction between the three nucleons in the initial state.

Under certain kinematic conditions, three-body exchange currents can be linked to the corresponding three-body forces [37]. The nature and importance of three-body forces in nuclei is still an unresolved problem but such mechanisms are needed in order to explain the observed binding energies of light nuclei [15]. Comparisons between experimental work on the photodisintegration of  $^3\text{He}$  and theoretical calculations by Laget [37] have also demonstrated the need for three nucleon absorption mechanisms. It has been shown that the cross section is dominated by two-body absorption but that three-body mechanisms play an increasingly important role as the photon energy increases and the cross section

moves towards more backward proton angles.

Any observed similarities between  ${}^3\text{He}(\gamma, \text{pd})$  and  ${}^{12}\text{C}(\gamma, \text{pd})$  would therefore suggest the same mechanisms also contribute in  ${}^{12}\text{C}$ . However, the work by Yau *et al.* has shown that the  ${}^{12}\text{C}(\gamma, \text{pn})$  reaction exhibits a different angular distribution to that of the photodisintegration of deuterium, implying different underlying mechanisms.

The photon interaction with a 3N cluster however, may not be the only or even the major absorption mechanism contributing to the  ${}^{12}\text{C}(\gamma, \text{pd})$  reaction. It may, for example, be an initial  $(\gamma, \text{pn})$  event followed by  $(\text{n}, \text{d})$  pickup in some final state interaction, or indeed a  $(\gamma, \text{pp})$  event followed by  $(\text{p}, \text{d})$  pickup. In the study by Yau *et al.* the angular distributions for  $(\gamma, \text{pn})$  and  $(\gamma, \text{pp})$  were seen to be significantly different in character. Comparisons between the angular correlations of the emitted particles from the  $(\gamma, \text{pn})$  and  $(\gamma, \text{pp})$  reactions in  ${}^{12}\text{C}$  and  ${}^{12}\text{C}(\gamma, \text{pd})$  may help resolve the contributing mechanisms. In addition, the magnitude of the cross section for the  $(\gamma, \text{pd})$  channel relative to the  $(\gamma, \text{pn})$  and  $(\gamma, \text{pp})$  channels and will yield important information. If, for example, the cross section for  $\text{pd}$  is appreciable compared to that of  $\text{pn}$ , then it is unlikely that the reaction mechanism could be dominated by a final state pickup process.

The fact that an intact deuteron emerges unscathed from within a nucleus in which it may have undergone collisions is itself surprising given that the deuteron is a weakly bound system and is therefore a fragile object. The  ${}^{12}\text{C}$  nucleus is however mostly 'surface' and this may just indicate that this reaction takes place on the outer edge of the nucleus. It may also suggest that the cross section for  $\text{pd}$  emission will decrease with the size of the nucleus. In summary, the  ${}^{12}\text{C}(\gamma, \text{pd})$  reaction channel is a small but extremely interesting component of the total photon absorption cross section and a study of this reaction may provide some information on the nature of three body mechanisms in heavier nuclei.

### 1.6.1 Previous Measurements of the $(\gamma, \text{pd})$ Reaction

The present work is the first systematic study of the  $^{12}\text{C}(\gamma, \text{pd})$  reaction over the photon energy range 110-400 MeV. However, measurements have been made for the  $(\gamma, \text{pd})$  reaction predominantly on  $^3\text{He}$ , [27, 28, 29, 30, 31, 32, 33, 34] but also on  $^{12}\text{C}$  [40] and  $^{16}\text{O}$  [26].

The photodisintegration of  $^3\text{He}$  is an obvious testing ground for our theoretical understanding of the fundamental interactions between nucleons in a nucleus. Requiring that theory reproduce the main features of the two and three-body break-up of  $^3\text{He}$  as well as the photodisintegration of the deuteron places strict constraints on the microscopic calculations. Several experiments performed on a  $^3\text{He}$  target are discussed in the next two sections.

### 1.6.2 The Two-Body Breakup of $^3\text{He}$

In the past, several measurements of the cross sections for the two-body break-up of  $^3\text{He}$  [27, 28, 29, 30] and the inverse radiative capture reaction [31, 32, 33, 34] have been made as tests of time-reversal invariance. For photon energies greater than 150 MeV, the earliest specific measurement of the two-body photodisintegration of  $^3\text{He}$  was performed by Argan *et al* [28] at Saclay. In contrast to the photodisintegration of deuterium they observed a monotonically decreasing cross section with increasing photon energy without any apparent structure in the delta region. In the  $^3\text{He}(\gamma, \text{pd})$  reaction the excitation of a Delta is suppressed due to the influence of the final state deuteron form factor and the cross sections are dominated, at forward and central angles, by the two-body photodisintegration mechanisms [38] shown on figure 1.7A. Agreement with the Saclay data was found in a similar experimental study by Gassen *et al.* [29] at Bonn. Both of the above measurements however disagree with the radiative capture results on the

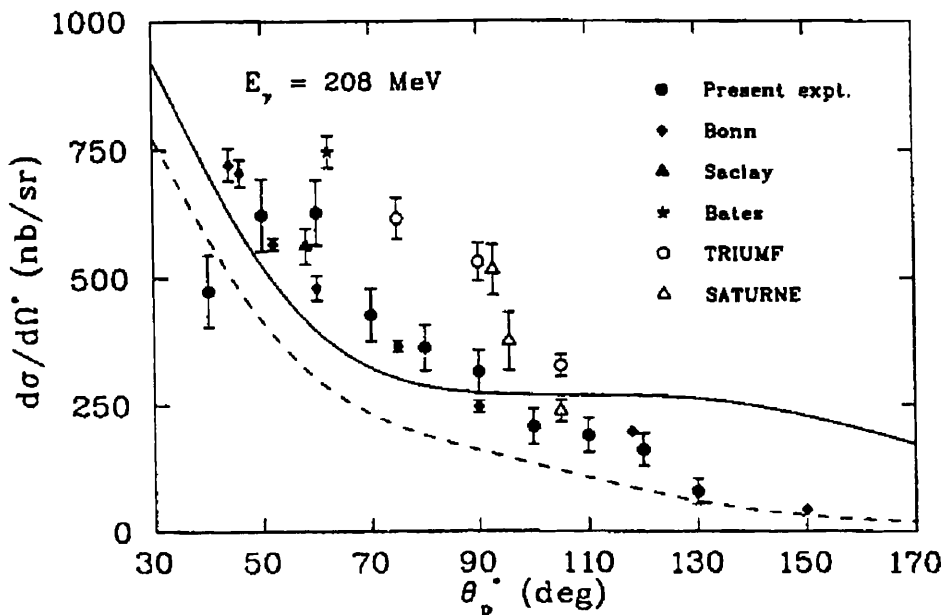


Figure 1.3: *CM system differential cross section for the two-body photodisintegration of  ${}^3\text{He}$  as a function of proton CM angle for  $E_\gamma=208$  MeV. The solid circles are from the Kolb *et al.* measurement [35]. Other results shown are from Bonn[29], Saclay[28], Bates[27], TRIUMPH[33] and SATURNE[34]. The curves are calculations by Laget including one and two-body mechanisms (dashed) and an additional meson double scattering term (solid).*

magnitude of the cross sections. One of the most recent photosintegration measurements at Bates [27], by Sober *et al.*, finds cross sections in agreement within errors with the radiative capture measurements and also shows the differential cross sections decreasing slowly with photon energy.

The first reported measurement of  ${}^3\text{He}(\gamma, \text{pd})$  with a tagged photon beam was performed by Kolb *et al.* [35] for photon energies in the range 166-213 MeV. Their results were in agreement with the earlier Bonn and Saclay data and for the first time were compared to theoretical calculations by Laget, see figure 1.3. The

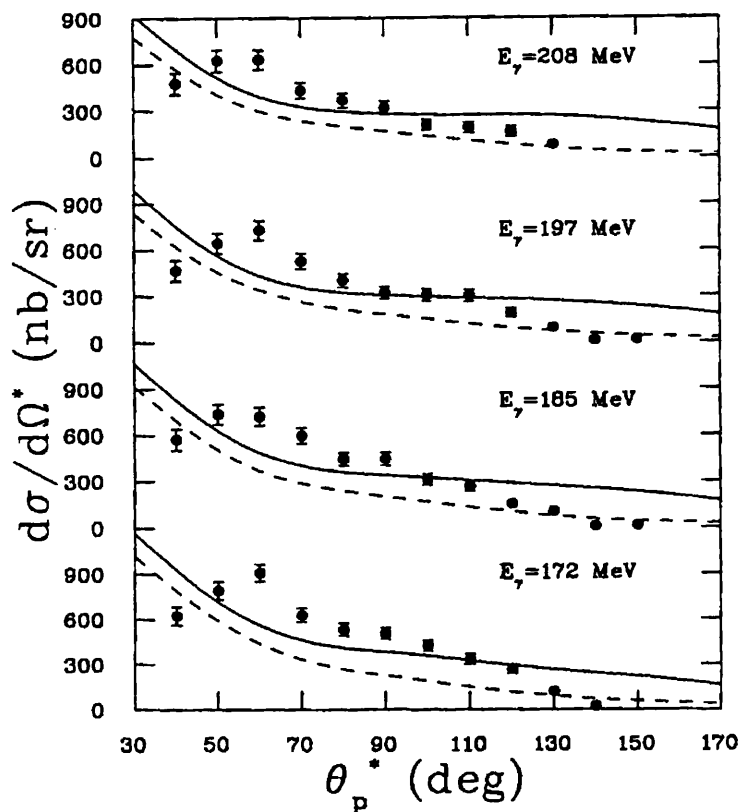


Figure 1.4: *CM system differential cross sections for the two-body photodisintegration of  $^3\text{He}$  as a function of proton CM angle for four photon energy bins, measured by Kolb et al. [35]. The curves are calculations by Laget including one and two-body mechanisms (dashed) and an additional meson double scattering term (solid).*

theoretical calculations by Laget [38], are described in a later section. It is clear that the one and two-body mechanisms are not enough to reproduce either the magnitude or the shape of the cross section. They found that the theory which included the contribution of the three-body mechanisms reasonably predicted the magnitude of the cross sections but differed somewhat in shape, particularly at the extreme angles of their measurement, as shown on figure 1.4.

Most recently the two-body photodisintegration of  ${}^3\text{He}$  between 200 and 800 MeV has been studied by Isbert *et al.* using the tagged photon facility at Mainz in conjunction with the large acceptance detector DAPHNE [5]. These results, some of which are shown on figures 1.5 and 1.6, confirmed a rapid decrease in the cross section at more forward proton angles with increasing photon energy while observing an enhancement in the cross section at more backward proton angles. Notably, the shapes of the proton angular distributions differed from those measured by Kolb *et al.*, although it should be noted that the range of photon energies employed in each experiment barely overlaps.

Isbert *et al.* observed a prominent bump in the cross section at backward angles for photon energies greater than 500 MeV. Again it is clear that, at backward proton angles, the one and two-body mechanisms do not describe the magnitude or the form of the cross sections, whilst the inclusion of the three-body processes [37] better represents the data.

### 1.6.3 Three-body Breakup of ${}^3\text{He}$

The study of the three-body photodisintegration of  ${}^3\text{He}$  to a  $ppn$  final state is complementary to the the study of the two-body breakup because it examines the same basic mechanisms but under different spin-isospin selection rules. The photodisintegration of  ${}^3\text{He}$  is dominated by absorption on a correlated  $pn$  pair but this pair mechanism is suppressed in the reaction  ${}^3\text{He}(\gamma,pp)n$  because of the absence of any dipole moment or meson exchange currents. This reaction is therefore an ideal candidate for the examination of weakly contributing processes such as the absorption of a photon by three nucleons. It is expected to be dominated by two-body  $pp$  absorption when the neutron takes away little energy but will show the additional contribution from three-body absorption when the neutron carries away a more equal share of the photon energy. In a study of this reac-

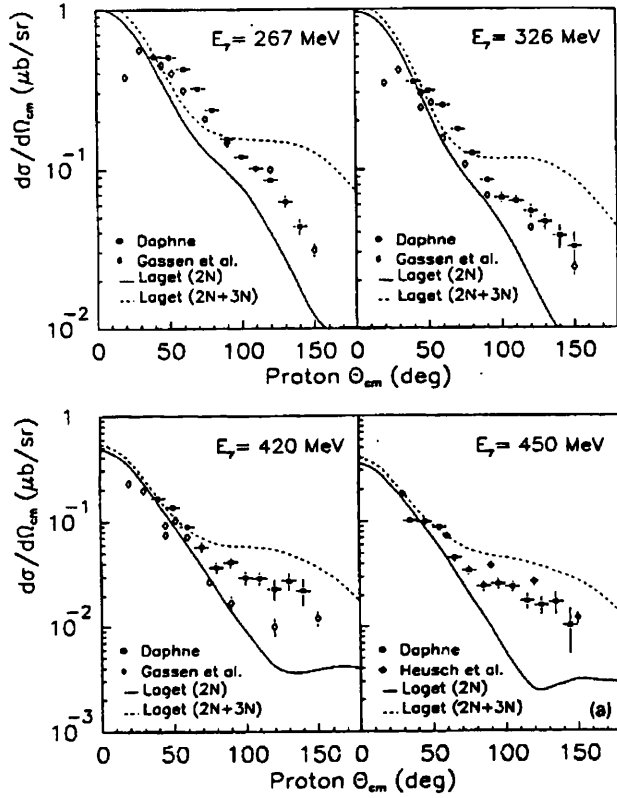


Figure 1.5: *Angular distributions for various photon energy bins up to 450 MeV measured by Isbert et al. [5] are compared to the previously published data [29, 36]. The calculations are by Laget [37]. The continuous curve gives the contribution from two-body mechanisms while the dashed curve also includes the contribution from three-body mechanisms.*

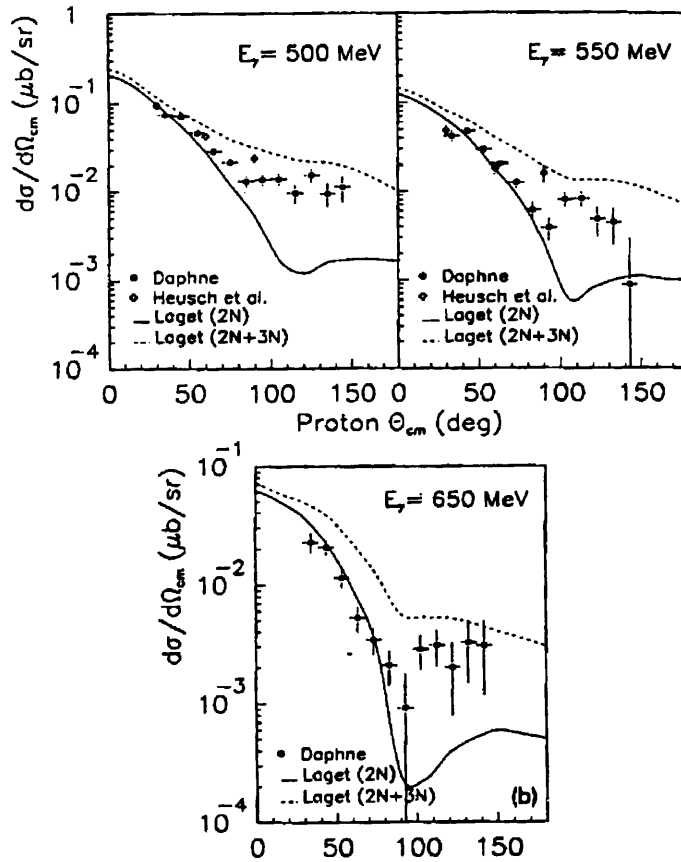


Figure 1.6: Angular distributions for various photon energy bins greater than 500 MeV measured by Isbert et al.[5] are compared to the previously published data [29, 36]. The calculations are by Laget [37]. The continuous curve gives the contribution from two-body mechanisms while the dashed curve also includes the contribution from three-body mechanisms.

tion by Audit *et al.* [3], again using the DAPHNE detector, in order to select 3N mechanisms, large momenta for the three outgoing particles were selected. The total cross section, integrated over the detector acceptance showed a pronounced peak at a photon energy around 320 MeV, indicating that in this region the  ${}^3\text{He}(\gamma,pp)n$  reaction is dominated by Delta excitation. This is in contrast to the two-body breakup channel which exhibits no structure in the Delta region. The theoretical calculations by Laget including the three-body mechanisms again follow the trends of the data and reproduce the main features of the total cross section.

#### 1.6.4 ${}^{12}\text{C}$ and ${}^{16}\text{O}$

In an experiment on the photo-deuteron emission from  ${}^{12}\text{C}$  using tagged photons from 360 to 600 MeV, Baba *et al.* [40] have shown that a moving-fireball model fits their data very well. In this process, when an energetic projectile is incident on a target nucleus, a massive hadronic cluster or fireball is formed with a specific temperature and mass. This fireball moves and eventually decays forming particles in the final state whose kinetic energy distributions obey the Boltzmann law of classical thermodynamics. They also attempted to fit their experimental data using a simple coalescence model where the deuteron is formed in the final state by the coalescence of a proton and neutron of similar momentum. They found that this model did not fit the data well. It should be noted however that this experiment is a single arm measurement and therefore did not measure back-to-back deuteron-proton pairs.

In the early measurement of the high energy photodisintegration of  ${}^{16}\text{O}$  by Hartmann *et al.* [26], in the photon energy range 100-450 MeV, a number of pd coincidence pairs were detected. The data were analysed under the assumption that the particles were emitted in a direct reaction. They found that this direct

model fitted the data well and that the energy dependence of the cross section was the very similar to that for the free process  ${}^3\text{He}(\gamma, p)d$ . However, this measurement suffered from a very small solid angle acceptance for protons (16 msr compared to 1 sr in the present study) and poor photon and emitted particle resolution.

### 1.6.5 Microscopic ${}^3\text{He}$ Photodisintegration Calculations

Microscopic calculations for the photodisintegration of  ${}^3\text{He}$  have been made by Laget [38]. In order to explain the observed binding of  ${}^3\text{He}$  it has been suggested that the effect of three-body forces needs to be considered [15]. Previous theoretical calculations [37, 38] by Laget demonstrated the importance of meson exchange currents in the both the two-body and three-body breakup but underpredicted the magnitude of the cross sections, especially at more backward angles. The dashed curves on figures 1.3 and 1.4 and the solid lines on figures 1.5 and 1.6 include all the most important two-body absorption mechanisms and they are shown diagrammatically on figure 1.7A. In addition to the two-body mechanisms the inclusion of a meson double-scattering term (figure 1.7B) in the calculations provides a closer match to the experimental data. This term, which includes all the nucleons, represents the photoproduction on one nucleon of a pion which is subsequently reabsorbed by the two remaining nucleons. Its contribution becomes more important than that of the two-body mechanisms when the momentum transfer increases as it is more likely to be shared between three rather than two nucleons. As indicated on figures 1.3-1.6 the calculation overestimates the cross section at forward and backward angles. Laget suggests that this is a hint that other mechanisms must be considered in the calculation and proposes a double pion production term as one such mechanism which will play an important role for photon energies in excess of 450 MeV. This term is shown on figure 1.7C.

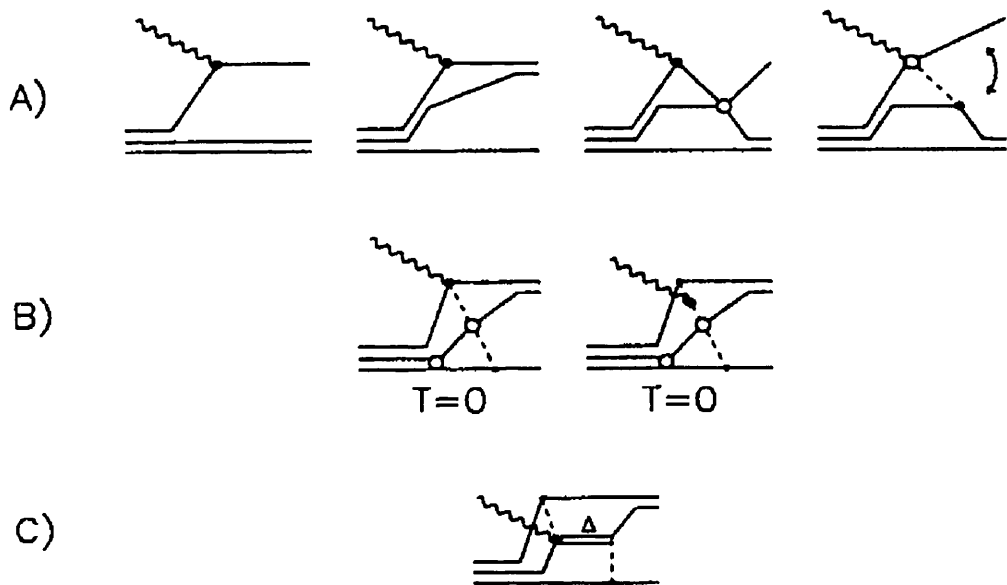


Figure 1.7: *The relevant diagrams included in the Laget calculations contributing to the two-body photodisintegration of  $^3\text{He}$ . (A) shows the one and two-body mechanisms, (B), the three-body meson double scattering term decomposed into its two dominant parts and (C) is the double pion production term which is not included in the calculations.*

Laget explains the absence of any structure in the Delta region for the two-body breakup channel as due to the  $pd$  final state having total isospin  $T = \frac{1}{2}$ . In the calculation, the photoproduced pion is absorbed by a  $T = 0$  nucleon pair which forbids the formation of a Delta, isospin  $T = \frac{3}{2}$ , at the first pion scattering vertex. If however, the pion is absorbed by a  $T = 1$  pair then a Delta can be excited and the resulting amplitude may interfere destructively with the more dominant amplitude (the absorption by  $T = 0$  pairs is six times larger than that of  $T = 1$  pairs [39]) and could account for the discrepancy between the model and the observed cross section at the more backward angles. The same underlying mechanisms are included in the calculations for the three-body breakup channel where the Delta excitation can be formed because the final state has three particles with total isospin  $T = \frac{3}{2}$ .

### 1.6.6 Aims of Present Work

The work presented in this thesis is a study of the  $^{12}\text{C}(\gamma, pd)$  reaction from data collected in 1993 over a wide range of photon energies and proton angles with an energy resolution of 6 MeV, which is enough to resolve the initial shells of the emitted nucleons. Two simulations of the experiment based on very different assumptions about the reaction mechanism have been developed and will be compared with the data in an attempt to shed more light on the way in which the reaction proceeds.

Direct comparisons will be made between the photon energy dependence of the  $^3\text{He}(\gamma, pd)$  reaction and that of  $^{12}\text{C}(\gamma, pd)$ . The underlying mechanisms in  $^3\text{He}$  are now reasonably well understood and the two-body breakup channel, unlike the three-body breakup channel, proceeds without the formation of a delta resonance in the intermediate state.

The angular dependencies of the emitted proton and deuteron from the  $^{12}\text{C}$

reaction will be compared with the observed angular distributions for the two-body photodisintegration of  $^3\text{He}$ . Similarities between the angular distributions would indicate that the reactions proceed through the same basic mechanisms. The examination of these energy and angle correlations will show the relative significance of the contributions from sequential reactions or from direct three-body absorption.

The next chapter is a description of the apparatus employed in the experiment and Chapter 3 is a detailed account of the calibrations of the various elements of the experimental setup. Chapter 4 outlines the stages in the data reduction and analysis and introduces the concepts involved in the Monte Carlo simulations of the experiment. The results of the study are presented in Chapter 5 with a discussion of the interpretation. The final chapter discusses the conclusions of the present work and suggests some developments which may be considered in any future work.

## **Chapter 2**

# **Experimental Apparatus**

## 2.1 Introduction

The ( $\gamma$ ,pd) experiment described in this thesis was performed at the Institut für Kernphysik at the University of Mainz in Germany in partnership with physicists from Edinburgh, Tübingen and Mainz. The Mainz Microtron (MAMI-B) produces an 855 MeV electron beam which is directed onto a radiator, producing Bremsstrahlung photons whose energies are determined using the Glasgow photon tagging spectrometer. The collimated photon beam is then directed onto the target inducing the ( $\gamma$ ,pd) reaction amongst many others. The protons are detected using PiP, a segmented plastic scintillator hodoscope, and the deuterons are detected with a large scintillator time-of-flight array, TOF.

## 2.2 The Mainz Microtron

The Mainz Microtron MAMI-B produces the highly stable 855 MeV, low emittance, 100% duty factor electron beam at currents of less than one picoamp to 100 microamps and consists of three successively larger race track microtron (RTM) stages.

### 2.2.1 The Race Track Microtron

Each RTM consists of a linear accelerating section (linac), two bending magnets and an array of return pipes, see figure 2.1. The linac is a series of cavities carrying radio frequency electric fields, powered by klystrons, which accelerate the electrons. The bending magnets recirculate the beam through the linac and on each pass the electron orbit radius is increased in such a way that the beam returns to the linac in phase with the accelerating field. The beam is recirculated many times, requiring only a small energy boost each time, and allows the accelerating

klystrons to be operated in continuous wave (c.w) mode. This c.w mode produces an essentially continuous beam because even though accelerating the electrons in phase with the electric field produces a microstructure in the beam, the 2.45 GHz field frequency is high enough that this is not distinguishable by the particle detectors. This continuous operation results in the 100% duty factor which, for a given average current, allows a much improved real to random coincidence ratio compared to previous technology using pulsed beams. Much reduced dead times, shortening the acquisition time needed to gain adequate statistics, are also an advantage of this mode of operation.

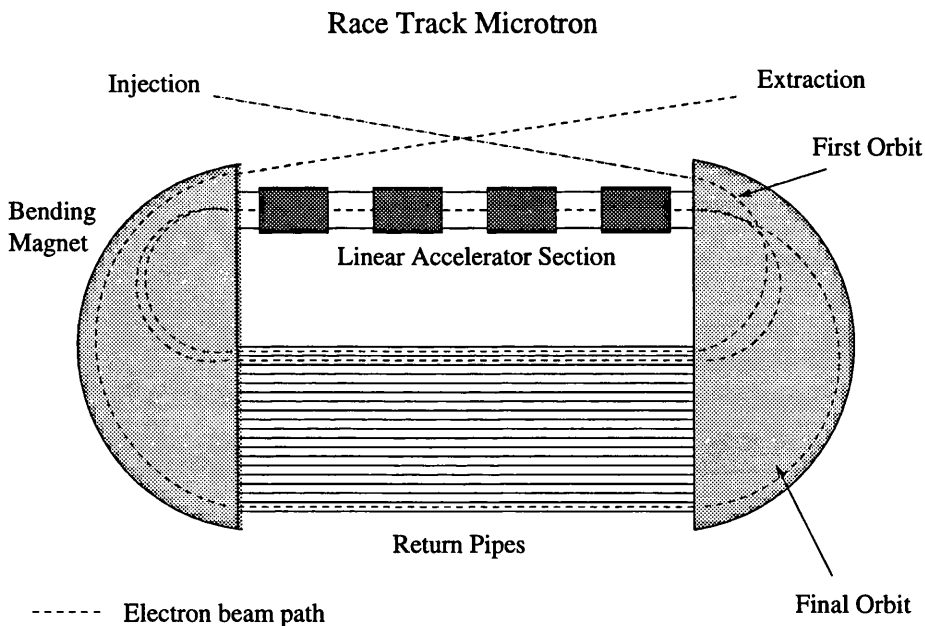


Figure 2.1: Schematic diagram of a racetrack microtron

### 2.2.2 MAMI-B

The MAMI-B facility is shown in figure 2.2. A 100 keV electron gun followed by three linac sections produces a 3.5 MeV electron beam which is fed into the 18 turn RTM1, increasing the beam energy to 14 MeV. The beam then enters the 51

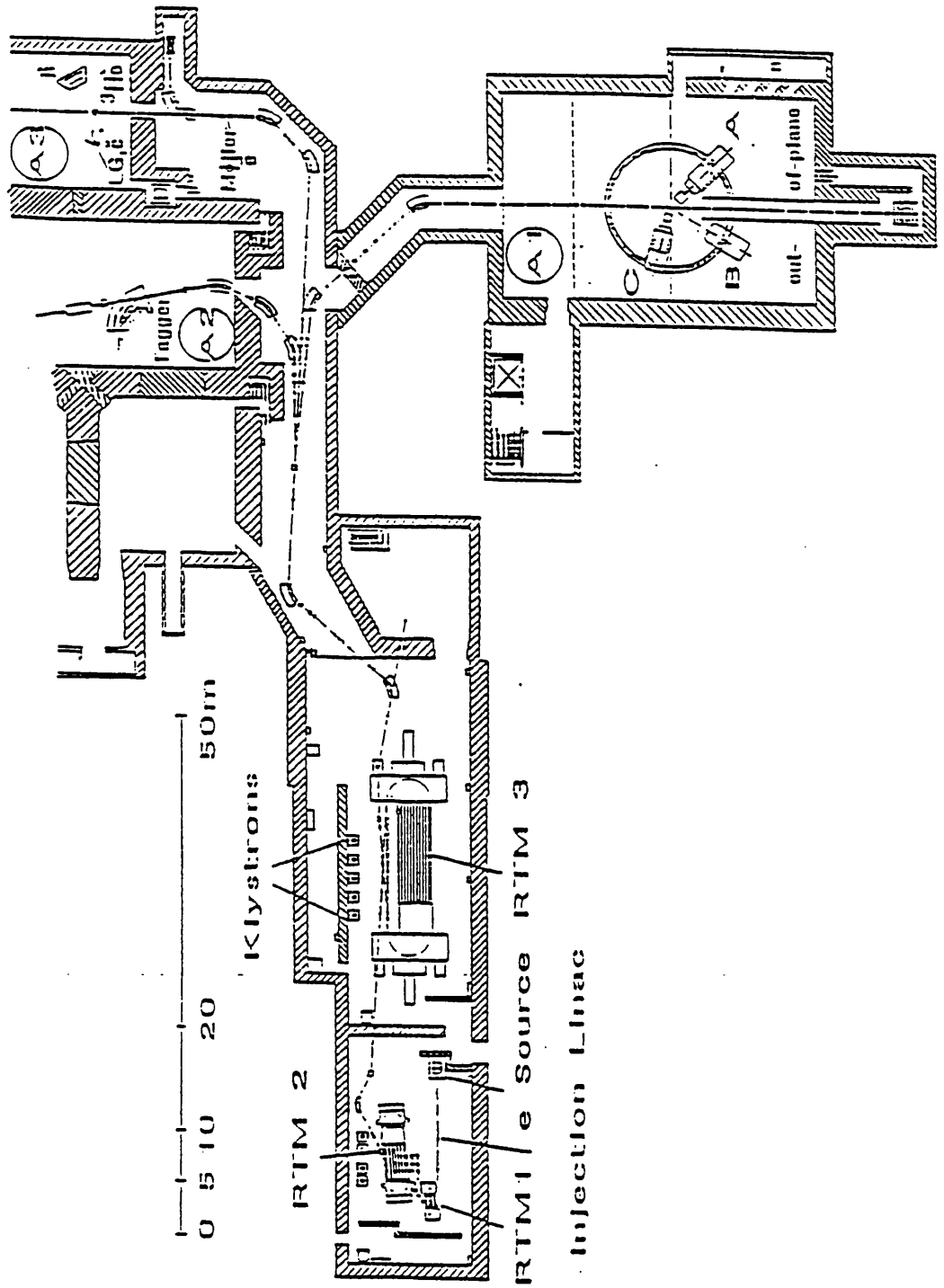


Figure 2.2: The MAMI-B facility

turn RTM2 increasing the beam energy to 180 MeV before finally entering the 90 turn RTM3 which boosts the beam to a final energy of 855 MeV. The emergent beam has a resolution of 60 keV and an emittance of less than  $0.14 \pi \cdot \text{mm} \cdot \text{mrad}$  in both the horizontal and vertical directions. The beam can then be steered by dipole magnets into any of the experimental halls shown in figure 2.2. The  $^{12}\text{C}(\gamma, \text{pd})$  reaction study was carried out in the A2 Tagger hall.

## 2.3 Photon Production and Tagging

Inside the A2 hall the 855 MeV electron beam is focused on to a  $4 \mu\text{m}$  Ni foil, producing a forward directed cone of Bremsstrahlung radiation with an energy distribution approximately proportional to  $1/E_\gamma$ . The energy of these Bremsstrahlung photons can be determined by a measurement of the energy of the electrons residual to the process, using the Glasgow Tagging Spectrometer [42, 43]. Given the incident electron energy  $E_e$  and the residual electron energy  $E'_e$  the photon energy is given by:

$$E_\gamma = E_e - E'_e \quad (2.1)$$

see figure 2.3.

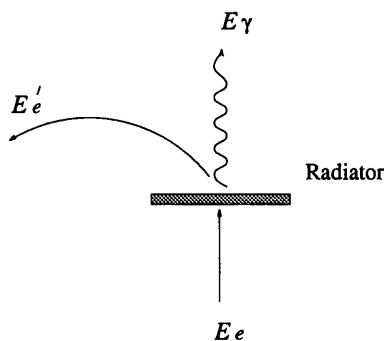


Figure 2.3: Schematic of photon tagging

### 2.3.1 The Glasgow Tagging Spectrometer

The Glasgow Tagger, a combined quadrupole-dipole, is a magnetic spectrometer designed to momentum analyse the recoiling electrons residual to the Bremsstrahlung process and is shown in figure 2.4. The quadrupole magnet provides vertical focusing, increasing the solid angle acceptance of the spectrometer and improving the resolution over the whole momentum range. The main dipole magnet bends and horizontally focuses the electrons onto a reasonably flat focal plane; it also acts to transport the main beam of electrons which have not interacted with the radiator away from the experimental hall and into the Faraday Cup beam dump in a neighbouring experimental hall. The design of the tagger provides a large momentum acceptance, the ratio  $p_{max} : p_{min}$  is  $\sim 16:1$  allowing the tagging of photons from 40 MeV to 790 MeV and the high homogeneity, better than 0.5%, of the dipole magnetic field gives the spectrometer an intrinsic resolution of  $\sim 120$  keV over this range [42, 43]. The position and time of arrival of the post-bremsstrahlung electrons on the focal plane is established by the focal plane detector array.

### 2.3.2 The Focal Plane Detector (FPD)

The focal plane detector [44] is an array of 353 scintillators spread along the focal plane, each equipped with its own photomultiplier tube, whose output is fed into a dual threshold discriminator which has a timing resolution of better than 1ns. The photon energy resolution, set by the width of the focal plane detectors, varies slightly over the tagging range around a 2.2 MeV average value. The detector elements overlap and a coincidence signal between neighbouring pairs is demanded in order to reduce the contribution from background electrons. The hit signals are counted by FASTBUS scalers, the sum corresponding to the total number

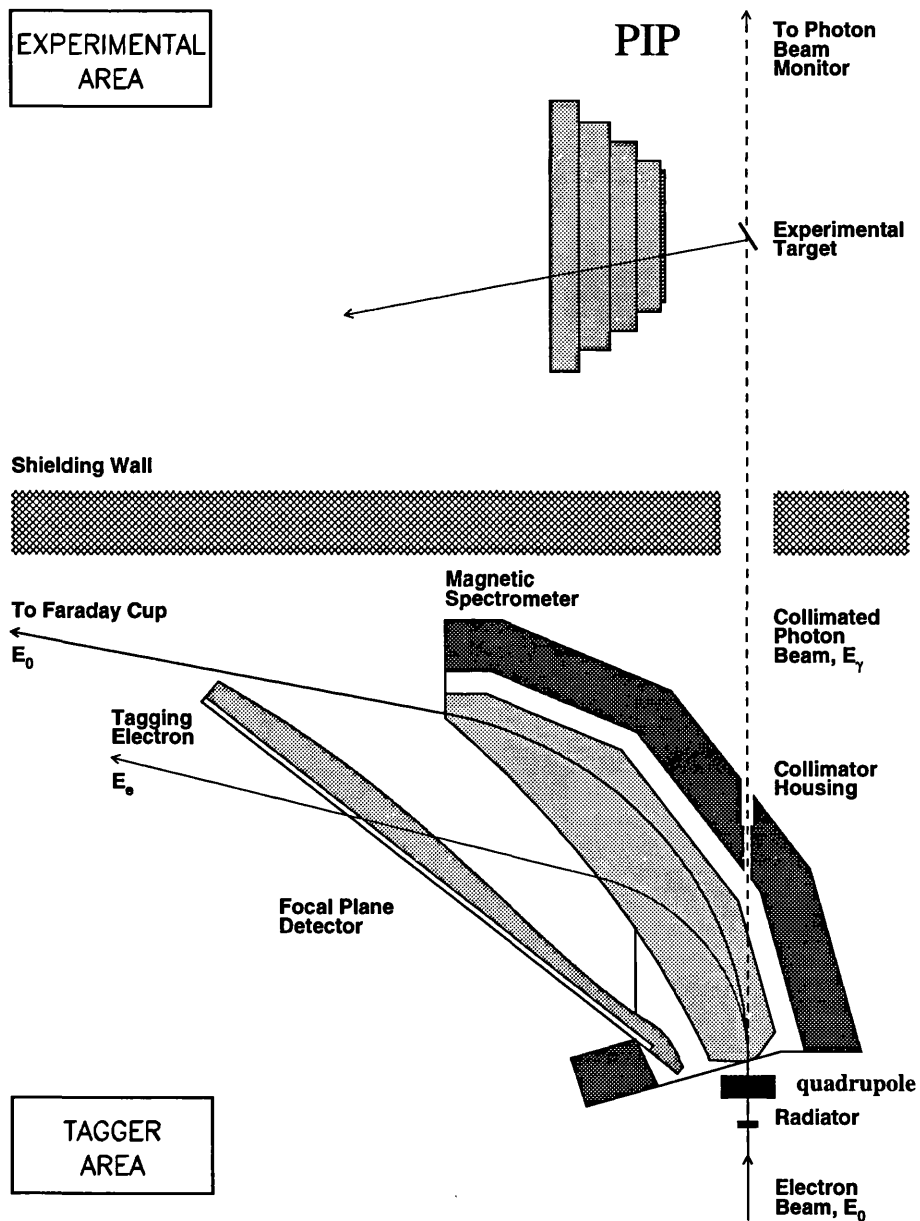


Figure 2.4: Schematic of the tagging spectrometer

of post-bremsstrahlung electrons striking the focal plane. These scalers are used to determine the photon flux through the target. The scalers are disabled by a PiP/TOF trigger (see below) and enabled again when the data acquisition system is ready for the next event. This avoids the need for any deadtime correction in the calculation of experimental cross sections. Correlation of the photoreaction with the tagged photon responsible needs a timing coincidence between the main detector system and the FPD. The timing information is recorded by time to digital converters (TDC's) gated by the trigger from the main detector systems.

### 2.3.3 Photon Beam Collimation and Tagging Efficiency

In order to minimise the uncertainty in the reaction vertex a well defined beam spot at the target is required and so the photon beam is collimated. The first collimator, and closest to the radiator, is positioned 250cm downline and is 5cm long and 5mm in diameter, defining a 15mm diameter beam spot at the target. Two more collimators of larger diameter placed further downline are designed to stop any charged particles produced in the first collimator reaching the  $\Delta E$  detectors (see below) which are placed close to the target.

Due to this collimation, some of the photons associated with detected electrons at the focal plane are removed from the beam and the fraction which reach the target is called the tagging efficiency. To calculate the photon flux at the target, a measurement of the tagging efficiency is made by placing a Pb glass detector directly in the photon beam, see figure 2.5. The Pb glass detector represents 30 radiation lengths and so effectively has a 100% photon detection efficiency. To avoid deadtime problems in this detector the electron beam current is reduced to  $\sim 0.5$  picoamps. Photons incident on the Pb glass detector generate triggers which start and gate the Tagger TDCs, recording the time of any coincident electrons on the FPD and so counting the number of photons reaching the target. As the

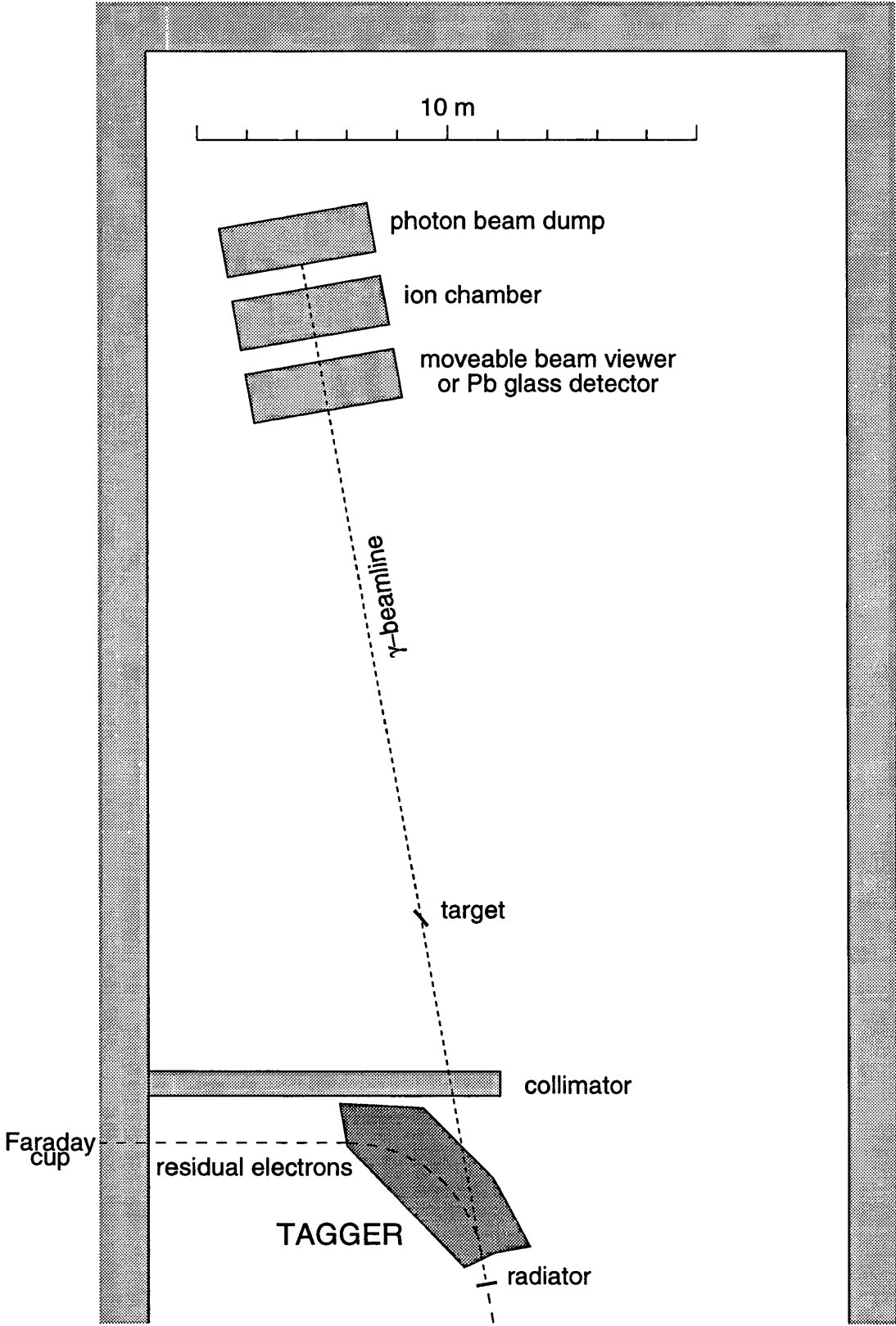


Figure 2.5: Schematic view of the photon beam line

Tagger scalers count the total number of electrons reaching the FPD, the tagging efficiency for each tagger element is:

$$\varepsilon_t = \frac{\text{TDCcounts}}{\text{SCALERcounts}} \quad (2.2)$$

The average tagging efficiency remained stable at  $\sim 55\%$ . There is a small photon energy dependence, see figure 4.4.

The majority of photons do not interact with the target and are dumped at the far end of the A2 hall as shown in figure 2.5. Also shown is the ionisation chamber used to give a rough on-line indication of the tagging efficiency by comparing the current in the chamber to the rate of electrons detected in the FPD. This monitors any drifts in the electron beam which would result in a decrease in the tagging efficiency.

## 2.4 The Targets

The targets used in this experiment were graphite, for the  $^{12}\text{C}(\gamma, \text{p})\text{d}$  measurement and  $\text{CD}_2$  for the  $\text{D}(\gamma, \text{p})\text{n}$  calibration data (see chapter 3). The carbon target is a graphite sheet and the  $\text{CD}_2$  is a piece of perdeuterated polythene, making the targets easy to handle and mount. Both targets were mounted on a mechanical ladder driven by a remotely controlled stepper motor. The thickness of the target has to be considered. A thicker target presents more nuclei/ $\text{cm}^2$  to the beam, increasing the reaction count rate but reducing the angular resolution by increasing the uncertainty in the reaction vertex within the target thickness. More importantly, a reduction in energy resolution also results as the charged reaction products must traverse more target material, consequently suffering more energy loss and introducing greater uncertainty in determining the particle's initial energy. The target thickness is then a compromise between high count rate and low energy loss. The  $^{12}\text{C}$  target thickness was chosen to be 2mm and the

number of target nuclei per  $\text{cm}^2$  was determined by a measurement of the surface area and weight. More information about the targets is given in table (2.1). By

target	$A$	thickness(mm)	$\rho_s(\text{mg}/\text{cm}^2)$	$n_{\text{target}}(\text{cm}^{-2})$
$\text{CD}_2$	16.02	2	216.0	$1.623 \times 10^{22}$
$^{12}\text{C}$	12.00	2	332.4	$3.336 \times 10^{22}$

Table 2.1: *The targets; for the  $\text{CD}_2$  target,  $n_{\text{target}} (\text{cm}^{-2})$  is the number of carbon nuclei.*

placing the target at a small angle to the beam the effective thickness of the target to the beam is increased while reducing the amount of material to be traversed by the reaction product emitted towards the PiP detector. In this experiment PiP was placed in three different positions and two target angles were used as shown in figure 2.6.

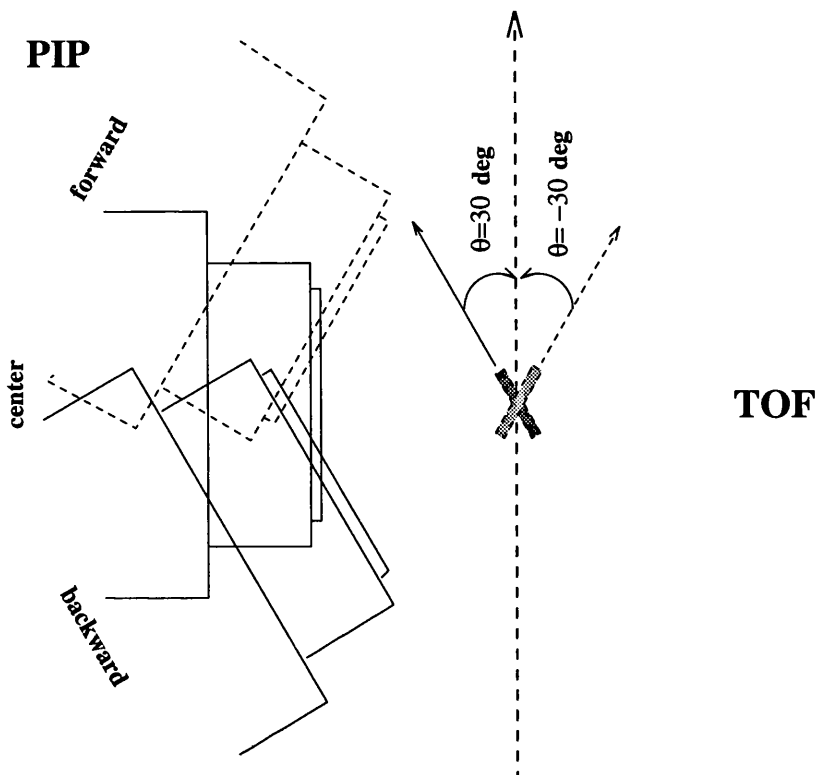


Figure 2.6: Target theta angle  $\theta = -30^\circ$  was used with PiP at Forward angle, while  $\theta = +30^\circ$  was used at central and backward angles.

## 2.5 The Particle Detectors

The PiP-TOF detector system will be discussed in detail. It consists of thin  $\Delta E$  detectors close to the target with thicker E detector arrays, PiP and TOF, further away. For this experiment the system was setup in three different angular settings. The layout of the particle detectors in the A2 hall for each setting is shown in figures 2.7-2.9.

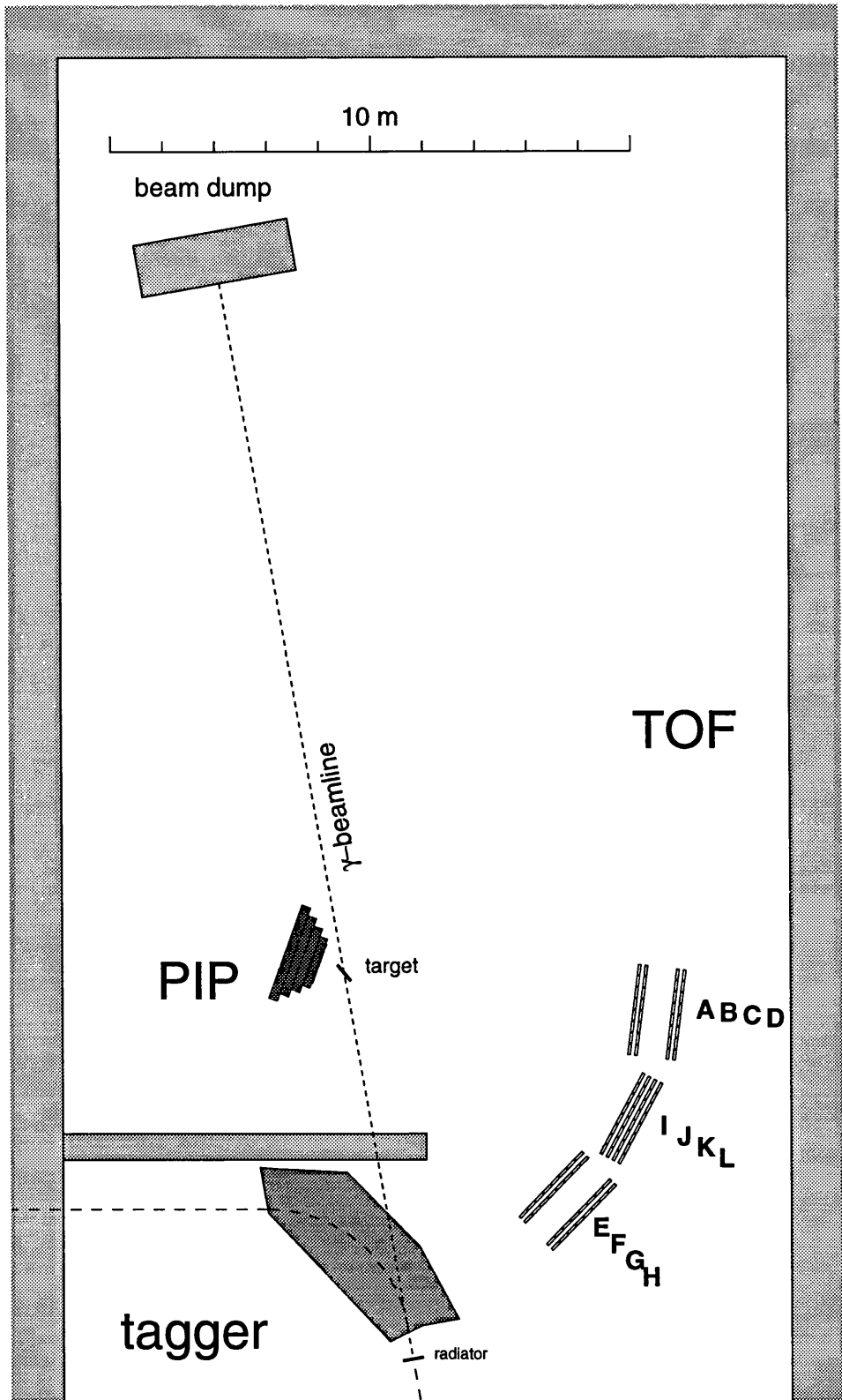


Figure 2.7: the experimental setup for PiP at FORWARD angle

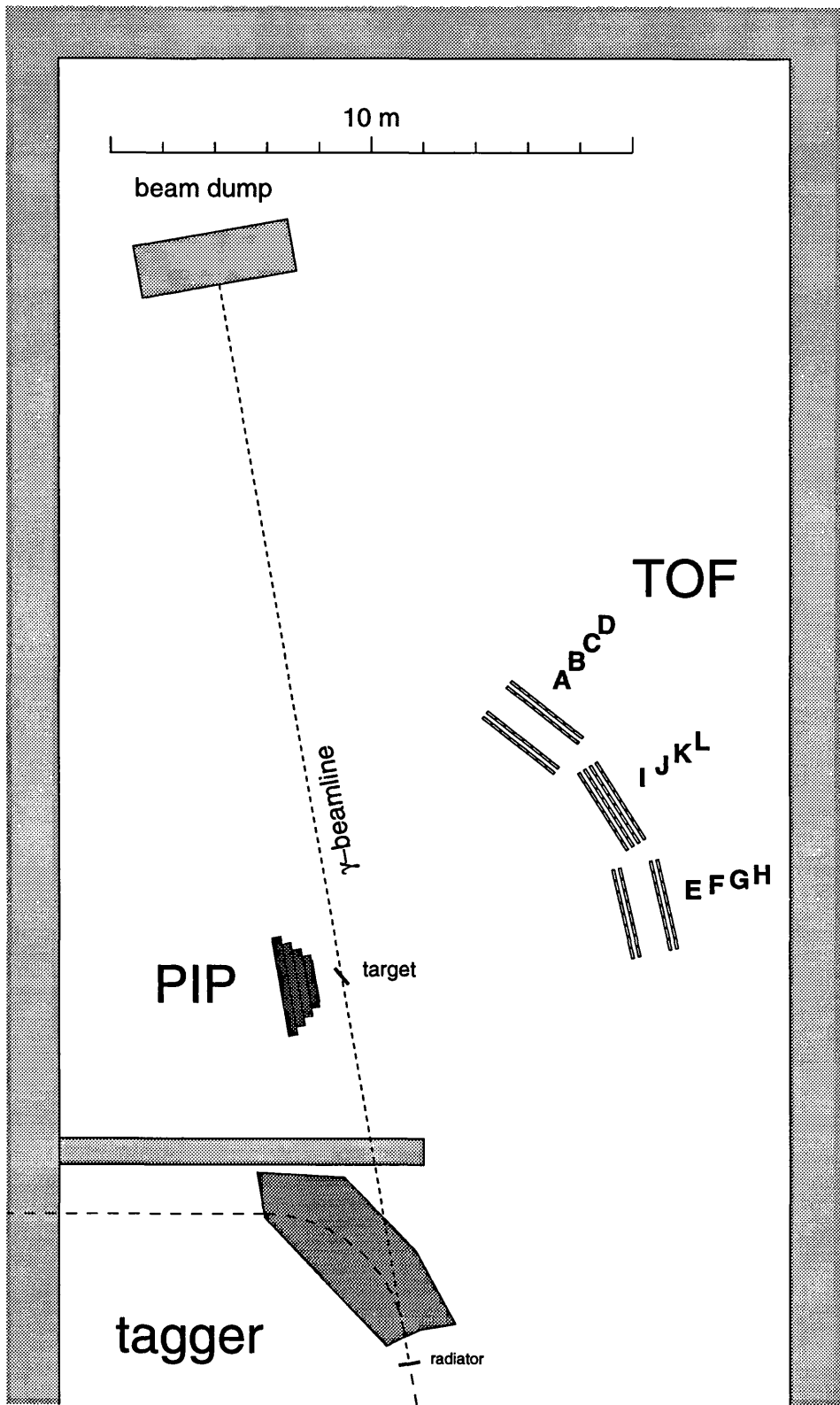


Figure 2.8: the experimental setup for PiP at CENTRAL angle

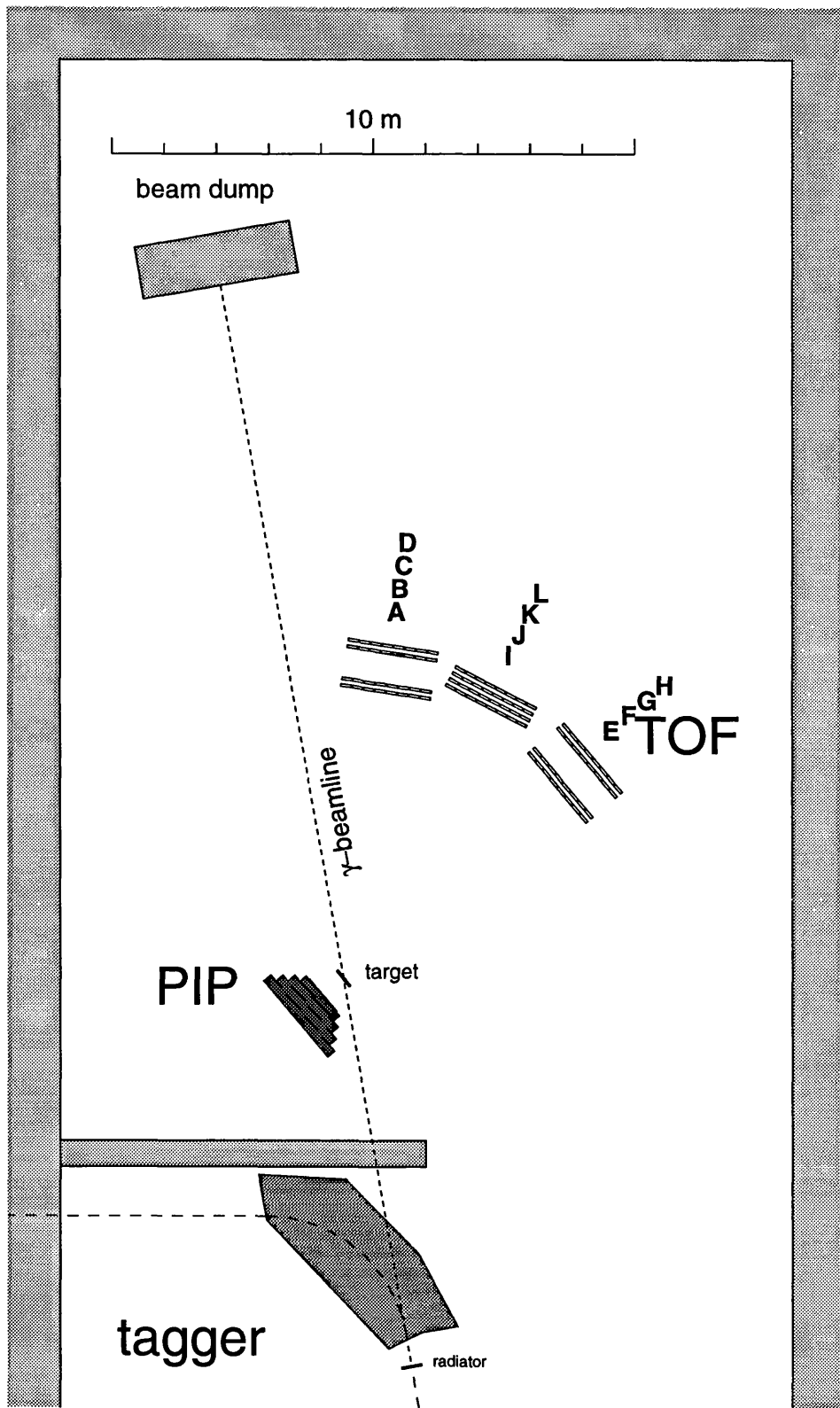


Figure 2.9: the experimental setup for  $PiP$  at BACKWARD angle

### 2.5.1 The $\Delta E$ Detector

The  $\Delta E$  detector ring is shown schematically in figure 2.10. It comprises seven

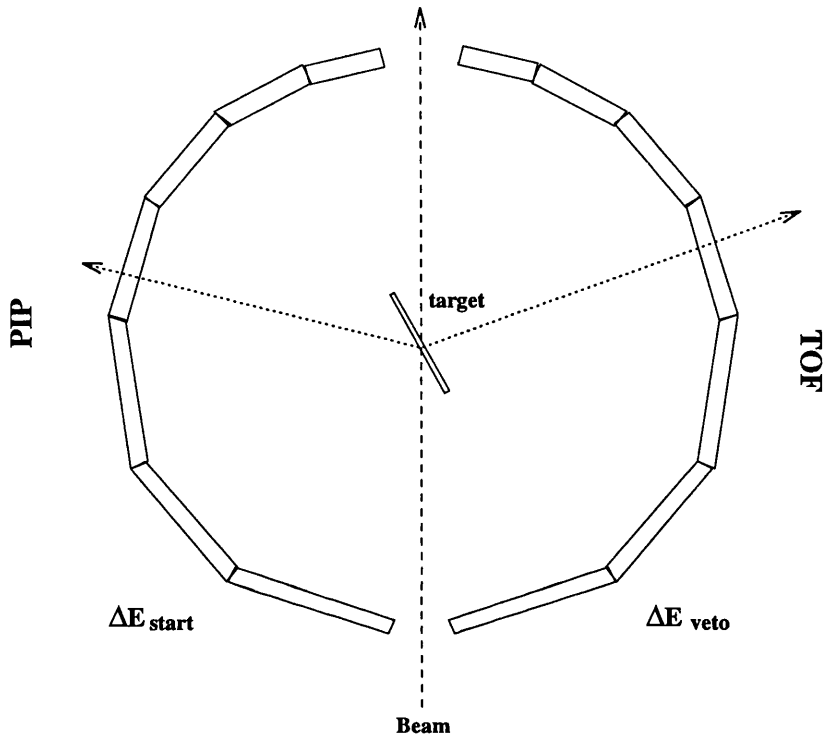


Figure 2.10: A schematic of the  $\Delta E$  Detector ring

segments of 2mm thin plastic scintillator on each side of the beam, centred on the target with a radius of  $\sim 11$  cm. The forward angle segments are smaller in width to compensate for the larger flux of particles produced mainly in atomic processes at forward angles. The segments on the PiP side of the ring,  $\Delta E_{start}$ , along with PiP, provide the first level trigger for the experiment. A coincidence between a  $\Delta E_{start}$  signal and PiP almost certainly means that a charged particle has come from the target and because of the ring's close proximity to the target, the time of this signal is closely correlated to the photoreaction time. This signal then generates the 'start' signal for all the TDCs and all times are measured relative to this. The segments on the TOF side,  $\Delta E_{veto}$ , identify charged particles on the TOF side in the offline analysis. The experimental trigger demands a signal from

the TOF detector, but ignores the  $\Delta E_{veto}$  veto.

### 2.5.2 PiP

PiP is a Pion-Proton plastic scintillator hodoscope [45] used in this experiment for the detection of protons. It is shown schematically in figures 2.11 and 2.12.

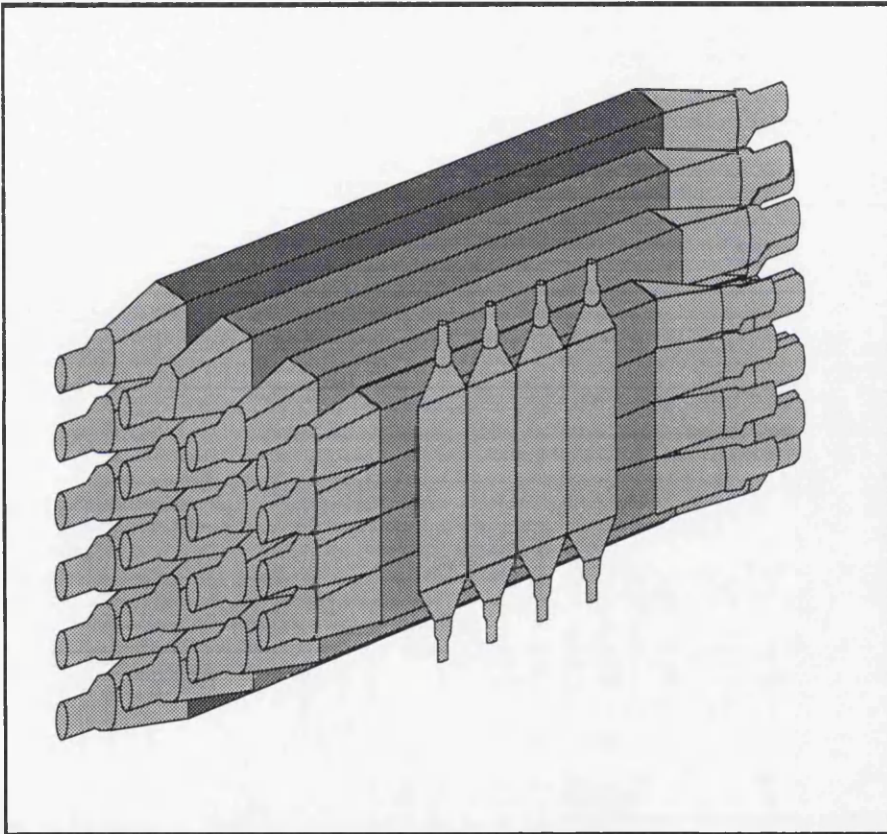


Figure 2.11: *A schematic of PiP*

It has a five layer segmented structure consisting of a thin  $\Delta E$  transmission layer, providing energy loss information, followed by four thicker E layers, E1 to E4, providing total energy and particle tracking information. The plastic scintillator used was NE110.

The thin  $\Delta E$  layer on the front face of PiP consists of four vertical scintil-

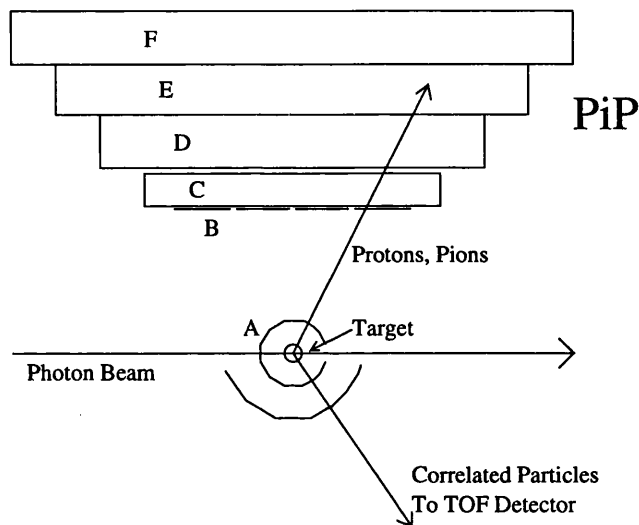


Figure 2.12: *Another view of PiP*

lators, each 2mm thick  $\times$  20cm wide  $\times$  42cm high, coupled to EMI 9954KB photomultiplier tubes by twisted strip light guides. This layer defines the solid angle of PiP as  $\sim 1$  sr. The time difference between signals from both ends of the  $\Delta E$  layer elements is used to define the vertical position of a particle in PiP, and this largely determines its azimuthal angle.

The E layers of PiP consist of scintillator blocks coupled to EMI 9823KB photomultiplier tubes by perspex light guides. These blocks are positioned horizontally at increasing distances from the target with each successive layer being larger than the previous one, minimising the loss of particles due to multiple scattering. The dimensions of the PiP E blocks are shown in table (2.2).

E layer	no of blocks	block L×D×H (cm)
E1	4	100 × 11.0 × 13.5
E2	4	130 × 17.5 × 17.5
E3	5	160 × 17.5 × 17.5
E4	6	190 × 17.5 × 17.5

Table 2.2: *Dimensions of the PiP E blocks*

Each scintillator element is individually wrapped to prevent light leaks and the detector is housed in a 5mm steel casing, acting as a barrier against low energy charged particles and as a second defence against light leaks.

### 2.5.3 TOF

The deuteron arm of the experiment is covered by TOF, an array of 96 NE110 plastic scintillator bars, measuring particle energy by the time-of-flight method. Each bar is 5cm thick × 20cm wide and 3m tall and is coupled to a Phillips XP 2312B photomultiplier tube at each end. The particles' positions are determined by the time difference between the signals at both ends. Each TOF photomultiplier tube is equipped with a flasher unit for the purpose of correcting the time walk of the leading edge discriminators, see Chapter 3. The bars are mounted onto 12 frames containing 8 bars each with the frames configured four deep. A TOF detector stand is shown in figure 2.13.

## 2.6 Data Acquisition

The signals generated at the photomultiplier tubes contain the energy and timing information of the photoreaction. From this information the trigger electronics identifies the events of interest and gates the ADCs and starts the TDC's that

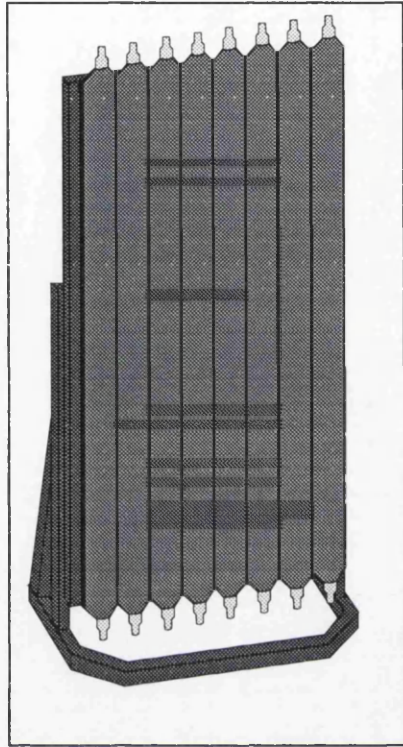


Figure 2.13: *Schematic diagram of a TOF detector stand showing a single frame of 8 detector bars.*

digitise this pulse charge and time information. The data acquisition process then stores this event information on a computer disk from where it can be written to tape.

### 2.6.1 Event Information in PiP/TOF

The charge in the pulses from the PM tubes contains the energy information. These are recorded by charge to digital converters (QDCs) which digitise the charge in the pulse by integrating over the limits, or gates, set by the trigger electronics. The QDCs used were the 10-bit, high density (32 channels) Phillips

Fastbus 10c2 units.

All the timing information is relative to a start time provided by the  $\Delta E_{start}$  which starts all the TDCs. The signal from each PM tube is fed into a leading edge discriminator which outputs a logic pulse when the signal rises over a preset threshold. This logic pulse then provides the stop signal to the TDC. The TDCs used were the 10-bit high density Phillips Fastbus 10c6 units.

## 2.6.2 Trigger Electronics

The electronic trigger must be able to identify the following events of interest:

- protons in PiP with an associated particle in TOF.
- cosmic muons entering PiP (used for calibration purposes)
- TOF flasher events (used for walk corrections)

The trigger is constructed with high density programmable CAMAC logic modules which allow the remote controlled setting of the trigger decoder. The trigger decoder consists of two Lecroy 4508 Programmable Logic Units (PLU). These constitute the brain of the trigger, each having eight logic inputs and eight logic outputs allowing any combination of inputs (triggers) to be programmed in, producing any combination of outputs.

Because this trigger logic needs time to identify the events of interest, the signals to the ADCs need to be delayed in order to arrive within the gate generated by the logic. To avoid a long delay time the trigger is split into two levels. The first level trigger makes a fast, simple decision. It also initiates a fast clear signal which is applied unless the event satisfies conditions derived from information which comes in later. Events meeting these conditions generate a second level trigger which vetos the fast clear signal.

### 2.6.3 The First Level Trigger

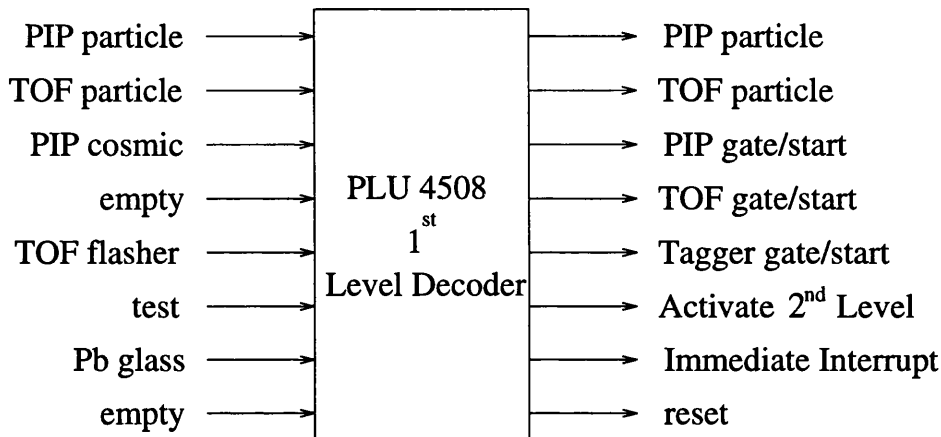


Figure 2.14: *The First Level Trigger decoder*

Figure 2.14 is a schematic of the first level trigger showing the inputs and outputs of the PLU. There are three active trigger inputs, on the arrival of which the PLU is immediately latched (disabled), preventing any further input. The active triggers are:

- The PiP particle trigger: Identifies charged particles in PiP originating from the target by demanding a coincidence between the  $\Delta E_{start}$ , the PiP  $\Delta E_2$  and the E1 layer.
- The cosmic trigger: Cosmic muons are identified by a coincidence between the top and bottom blocks in either the E2 or the E3 layers. Because of the close proximity to the target the cosmic trigger for the E1 layer requires a coincidence between all four blocks in the layer. These coincidence patterns are identified by another Lecroy 4508 PLU.
- TOF flasher trigger: This is used to correct for the time walk of the TOF leading edge discriminators. The whole flasher system is driven by an os-

cillator which also drives the flasher trigger.

The Pb glass trigger is used in the tagging efficiency runs and the remaining inputs are made redundant during the present measurement. The output of the PLU results in the following:

- The PiP particle trigger gates the ADCs so that analogue to digital conversion can begin and provides start signals to the TDC's. However the readout cycle is not yet initiated; instead the second level decoder is primed. This makes use of information arriving later.
- The cosmic/TOF flasher triggers provide ADC gates and TDC starts to PiP/TOF respectively. These triggers do not require any further decisions to be made and interrupt the data acquisition computer so it can proceed in reading out the ADCs and TDCs and store the event. The ADCs are then cleared and the system is reset, ready for the next event.
- If more than one trigger is present at the same time then the event is rejected. All the ADCs are fast cleared and the system is reset for the next event.

#### 2.6.4 The Second Level Trigger

The second level triggers are engaged when a charged particle has been identified in PiP. Figure 2.15 shows the second level trigger PLU inputs and outputs. There are four active second level trigger inputs:

- **Electron Reject:** Atomic processes like Compton scattering or pair production produce a large background of low energy electrons in PiP which would swamp the data if read out. Instead they are rejected by applying a diagonal  $\Delta E$ -E cut on a 2-D plot on-line. The effect of this cut is shown in

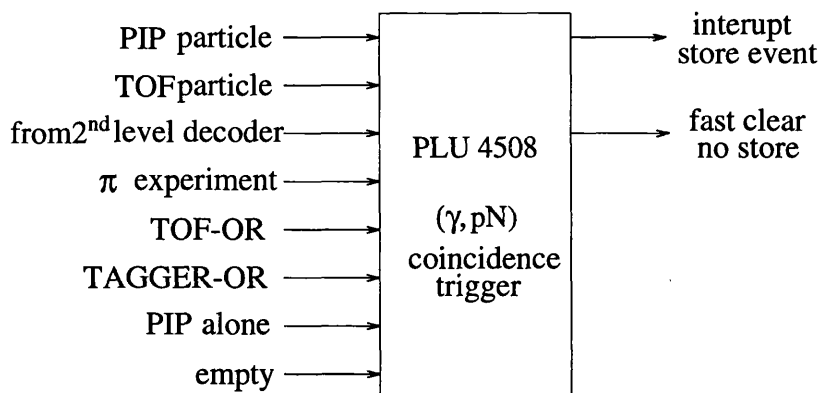


Figure 2.15: *The Second Level Trigger decoder*

figure 2.16. Electrons deposit very little energy in PiP and are located in

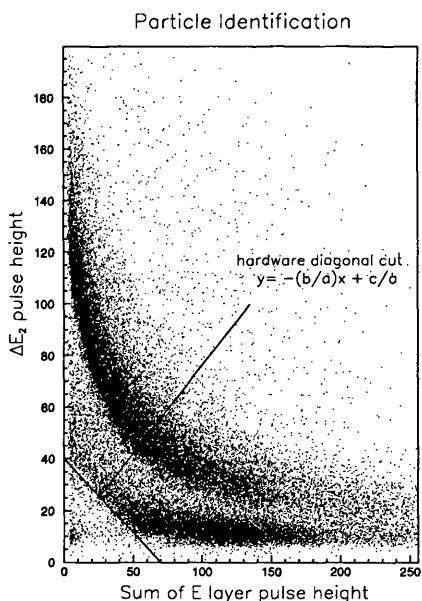


Figure 2.16:  *$\Delta E$ -E particle identification*

the bottom left corner of this plot. By performing a weighted sum of the two signals from the  $\Delta E$  and E1 layers,  $ay$  and  $bx$  say, and demanding the output to be above a certain discriminator threshold,  $c$ , an event will be

accepted if

$$ay + bx \geq c \quad (2.3)$$

then the line corresponding to the diagonal cut is

$$y = -\frac{b}{a}x + \frac{c}{a} \quad (2.4)$$

where  $a$  and  $b$  are weights determining the slope of the cut.  $a$  and  $b$  are set using attenuators. The effects of the cut can be gauged on-line allowing a fine tuning of the trigger. However, this cut alone might also veto some of the high energy protons that reach the E2 layer because of fold back when the E1 signal no longer corresponds to total energy and so a similar diagonal cut on E1 versus E2 is used to recover these events. All charged particles reaching E3 are accepted irrespective of whether the event exceeds these diagonal cuts.

- TOF-OR: Approximately 90% of events with a particle in PiP have no associated particle in TOF. This trigger is a gated OR of all 96 TOF bars and requires a particle to be detected in TOF within 400 ns of the initial PiP trigger.
- TAGGER-OR: This trigger is a gated OR of all 352 FPD elements and needs a PiP-Tagger coincidence within 80 ns of the initial PiP trigger. At normal data-taking beam currents there are usually several electrons present within this time window rendering the trigger effectively redundant.
- The remaining second level inputs were not programmed during this experiment.

The PLU then primes one of two output states:

- **Accept Trigger:** In the presence of all three active triggers the output will provide an interrupt signal to the data acquisition computer, the ADCs will be read out and the event stored. The trigger units are then reset.
- **Fast Clear:** If any of the three trigger conditions are not met, the event is rejected and the ADCs and trigger units are cleared. The whole system is reset and no interrupt is generated.

For  $\text{CD}_2$  calibration runs the TOF-OR requirement was withdrawn.

### 2.6.5 The Acquisition System

The acquisition system 'ACQU' [46] is run on an Eltec E7 single board computer housing a Motorola 68040 chip running an OS9 operating system. A VME-bus system controls the readout and data transfer to the storage medium is done via an ethernet TCP/IP connection. The control of the data acquisition is done remotely from outside the experimental hall using a console that connects to the E7 via ethernet. The adjustment of discriminator thresholds and the trigger logic requirements of the PLUs are done via the console. It also controls the high voltage power unit to all the PM tubes and the stepper motor of the target stand.

A DEC-VAX work station is used for the initial storage of the data onto disk ready for transfer onto exabyte tapes. For convenience the data is split up into files, each file containing the data collected during  $\sim 1$  hour of running. The work station also allows on-line preliminary analysis and monitoring of the incoming data using software written in 'C'.

## **Chapter 3**

# **Detector Calibrations**

Information from a typical  $^{12}\text{C}(\gamma, \text{pd})$  reaction event comes in the form of QDC and TDC indices and their channel contents. In order to extract physical quantities from this raw data it is necessary to calibrate the detectors. The calibration procedures for each detector are discussed in this chapter.

## 3.1 General Concepts

The physical processes enabling us to detect particles are different for charged and uncharged particles. For charged particles use is made of their electromagnetic interactions with the atomic electrons of the detector material, in this case, plastic scintillator. Neutrons can be detected through their strong interaction with atomic nuclei, producing charged secondary particles. The light produced by the primary or secondary ionizing particle is reflected onto a photomultiplier tube and the collected light is used to produce a QDC input pulse.

### 3.1.1 Pedestals

The integrated charge in the pulse is proportional to the number of photons produced in the scintillator and the QDC is used to convert this into a number. The integration time is controlled by a gating pulse and is set to be longer than the analogue pulses. A constant offset, the pedestal, arises from the integration over the gate time of the constant DC current in the QDC. This means that even when no analogue pulse is present every QDC registers a small output number  $p$  for every gate pulse. In normal operation this is not read out by setting a read-out threshold in the QDC just above the pedestal level. For QDC's which are read out the pulse charge  $Q$  is:

$$Q = Q' - p \quad (3.1)$$

where  $Q'$  is the number read out and the pedestal value  $p$  is obtained from runs where the readout thresholds are removed. See figure 3.2.

### 3.1.2 Relation between pulse charge and number of scintillation photons

Relating the number of photons generated by a particle,  $N_{par}$ , to the number of photons collected at the PM tubes at each end of a scintillator block is complicated by the attenuation of the light as it propagates along the detector block resulting in a position dependence of the detected photons. This attenuation is assumed to be exponential with decay constant  $k$  and if the pedestal subtracted pulse heights  $Q_1$  and  $Q_2$  are proportional to the number of photons,  $N_1$  and  $N_2$  collected at the PM tubes then:

$$N_1 = \frac{N_{par}}{2} \exp\left(\frac{-x}{k}\right) \quad (3.2)$$

$$N_2 = \frac{N_{par}}{2} \exp\left(\frac{x-l}{k}\right) \quad (3.3)$$

where  $x$  is the hit position along the block and  $l$  is the length of the block.

$$N_1 N_2 = \left(\frac{N_{par}}{2}\right)^2 \exp\left(\frac{l}{k}\right) = constant \times (N_{par}^2) \quad (3.4)$$

$$N_{par} \propto \sqrt{N_1 N_2} \propto \sqrt{Q_1 Q_2} \quad (3.5)$$

i.e the light produced by the particle is proportional to the geometric mean of the pulse heights from each end of the block. While this removes most of the position dependence there is still some residual droop indicating that the attenuation is not exactly exponential [48]. The residual droop is corrected using a parabolic function of position  $f_{droop}(x)$ :

$$N_{par} = constant \times \left[ \frac{\sqrt{Q_1 Q_2}}{f_{droop}(x)} \right] \quad (3.6)$$

The droop function is obtained from the data using cosmic muon events (see section 3.4.2 and figure 3.7.

Some high energy particles, near to one end of a block, produce signals which are greater than the range of the QDCs and so are not recorded. However the energy of these events can be recovered using the signal from the QDC at the opposite end. This procedure is described in the next section.

### 3.1.3 Replacement QDCs

Events which produce pulse heights large enough to 'overflow' the QDC can be 'rescued' using the information from the QDC at the opposite end of the detector block in order to estimate the 'missing' pulse height. The pedestal subtracted detected pulse heights,  $Q_1$  and  $Q_2$ , are given by

$$Q_1 = G_1 \frac{N_{par}}{2} \exp\left(\frac{-x}{k}\right) \quad (3.7)$$

$$Q_2 = G_2 \frac{N_{par}}{2} \exp\left(\frac{x-l}{k}\right) \quad (3.8)$$

where the parameters are as defined in equations 3.2 and 3.3 and  $G_1$  and  $G_2$  are the gains of the PM tubes. Taking the ratio of the above equations, with the gains matched, gives

$$\left[ \log\left(\frac{Q_1}{Q_2}\right) \right] \times \left( -\frac{k}{2} \right) = x - \frac{l}{2} \quad (3.9)$$

or  $\implies$  
$$ph = \log\left(\frac{Q_1}{Q_2}\right) \times ph1 + ph0 = position \quad (3.10)$$

where  $ph1 = -\frac{k}{2}$  and  $ph0 = \frac{l}{2}$ . Using 'complete' events where  $Q_1$ ,  $Q_2$  and the hit position are known (see section 3.1.6) the parameters  $ph1$  and  $ph0$  can be found for each bar by plotting  $(ph - position)$  against  $position$ .  $ph1$  is found by adjusting the slope of the ridge until it is horizontal, and the offset  $ph0$  is given by the condition that  $(ph - position) = 0$ . The right side of figure 3.1 shows the result plotted with the correct values of  $ph1$  and  $ph0$ .

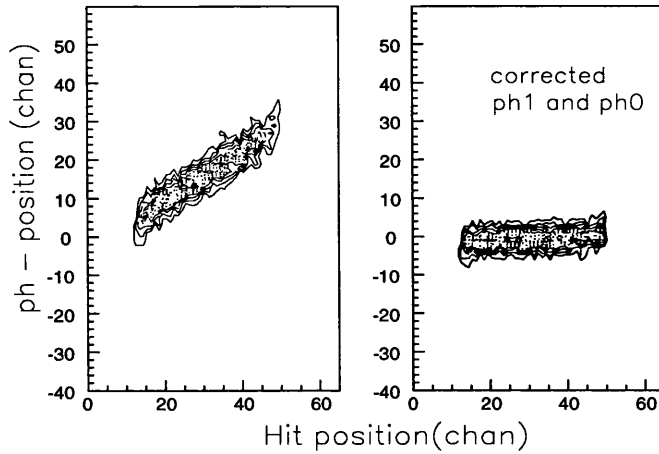


Figure 3.1: *Determining the parameters needed for the reconstruction of missing QDC's*

### 3.1.4 Thresholds

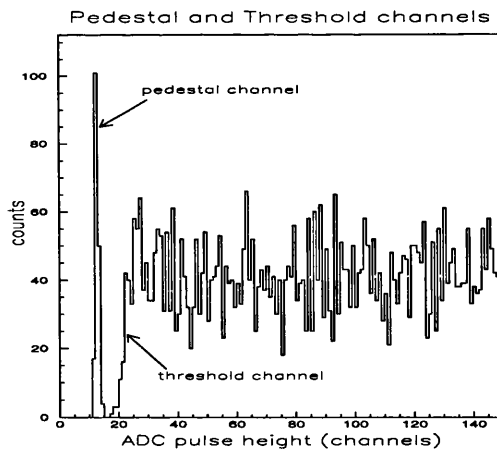


Figure 3.2: *Pedestal channel and discriminator threshold.*

The TDC value represents the time of a pulse relative to the start pulse. Both the TDC start and stop pulses are generated from leading edge discriminators whose thresholds define the acceptance of the detectors. These hardware thresholds are set high enough to cut out unwanted low energy background and electronic noise but low enough to detect most of the events of interest. The threshold value is

also needed for the discriminator walk corrections and is obtained by plotting the QDC spectrum under the condition that the corresponding TDC fires. Figure 3.2 shows a typical QDC spectrum with the discriminator readout threshold and its position relative to the pedestal value.

### 3.1.5 Discriminator Walk Corrections

The timing of signals produced by leading edge discriminators has an input pulse height dependence called 'walk' and corrections have to be made for the time slewing introduced. A knowledge of the threshold and the pulse 'risetime' are required. Figure 3.3 shows this effect.

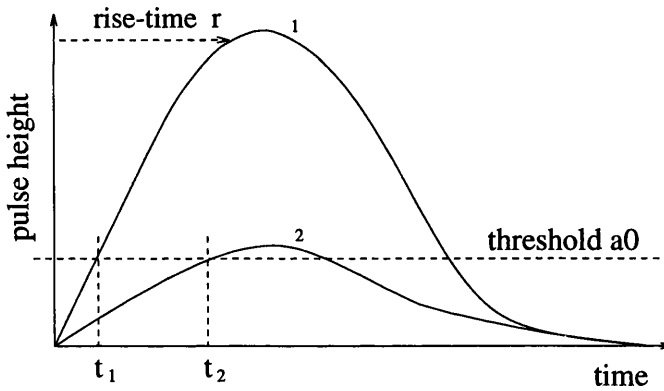


Figure 3.3: *The effect of 'Walk'*

As pulse shapes are approximately parabolic and independent of height the following parameterisation based on the work of Braunschweig [49] can be used to correct for the walk,

$$T' = T + r \left( 1 - \sqrt{\frac{a_0}{a}} \right) \tag{3.11}$$

where  $T'$  is the corrected TDC channel,  $r$  is the risetime in tdc channels, and  $a$  and  $a_0$  are the pulse height and threshold in qdc channels. The rise time was obtained

from the data and the different methods used for each detector are discussed in the relevant sections below.

### 3.1.6 Position

The walk corrected TDC times are used to determine the particle hit position relative to the centre of the detector block. The position,  $x$ , is derived from the time difference between the signals at each end of the block:

$$T_2 - T_1 = 2x/v + \text{constant} \quad (3.12)$$

where  $v$  is the velocity of the light along the block. Then:

$$x = (v/2)(T_2 - T_1) + \text{constant} \quad (3.13)$$

The factor  $v/2$  is obtained from the data as is the constant which reflects the cable delays in the system. This is discussed in more detail in section 3.4.1

## 3.2 The Start Detector

The start detector  $\Delta E_{start}$  is the PiP-side of the  $\Delta E$ -ring; it surrounds the target and generates the TDC start signals. Ideally the start pulse should occur at a time,  $t_{startpulse}$ , which is the same as the reaction time,  $t_{reaction}$ . In reality however corrections need to be made for discriminator walk, misalignments in the timing between the different start elements and the flight time of the particle between the target and the detector. The corrections are included in the term  $\Delta t_{start}$ :

$$\Delta t_{start} = \Delta t_{walk} + \Delta t_{flight} + \Delta t_{align} \quad (3.14)$$

Then the reaction time  $t_{reaction}$  is:

$$t_{reaction} = t_{startpulse} - \Delta t_{start} \quad (3.15)$$

The start detector rise time is obtained from a scatter plot of the pulse height from a start detector element against a tagger element TDC after first correcting for the variable flight time of particles of different energy moving between the target and the start detector. This flight time correction,  $\Delta t_{flight}$  can be deduced once the energy of the particle is determined using the methods described in the energy calibration section below. The walk is corrected using equation 3.11 Figure 3.4 shows the start detector pulse height versus the uncorrected and start corrected TDC.

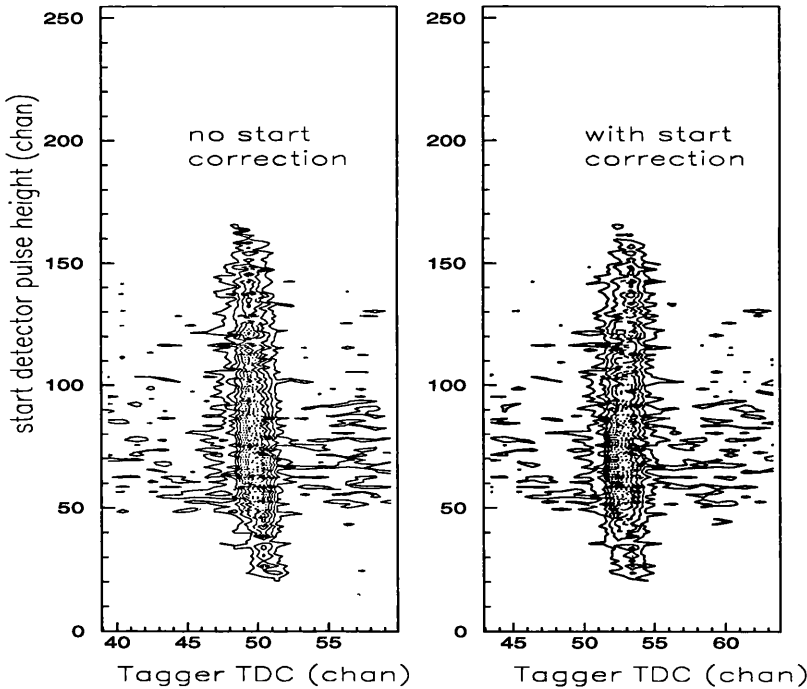


Figure 3.4: Application of the start correction to the  $\Delta E_{start}$

The ridge reflects the difference in transit times of the photon from the radiator to the target and of the residual electron from the radiator to the tagger’s focal plane. Since both the photon and the residual electron are relativistic particles this difference in transit time is a constant.

The parameter  $\Delta t_{align}$  is just an offset to align the timing of each of the

elements and is obtained by plotting one tagger element TDC spectrum for each of the start elements subject to the condition that just that particular element has a signal.

### 3.3 The Tagger

The tagger measures the residual electron energy and its time of arrival at the focal plane relative to the reaction time. The electron energy is calculated from the hit position along the focal plane with each focal plane detector element covering a small range of electron energy. The tagger utilises high/low dual threshold discriminators which exhibit negligible walk. The electron trajectory, and therefore the electron energy, is a function of the field strength of the bending magnet which is measured precisely using an NMR probe [50]. Knowing the residual electron energy together with the original electron beam energy leads directly to the photon energy which is just the difference between the two.

Electrons that are coincident with the photo-induced reaction products form a peak in each tagger element's TDC spectrum. By applying the start correction defined in section 3.2 this peak is sharpened and the corrected tagger TDC spectra are aligned to form the OR of all 352 channels. Figure 3.5 shows the aligned tagger TDC spectrum. The flat random background results from electrons which are not coincident with the photon that induced the reaction.

### 3.4 PiP

PiP covers the proton arm of the  $^{12}\text{C}(\gamma, \text{p})$  measurement.

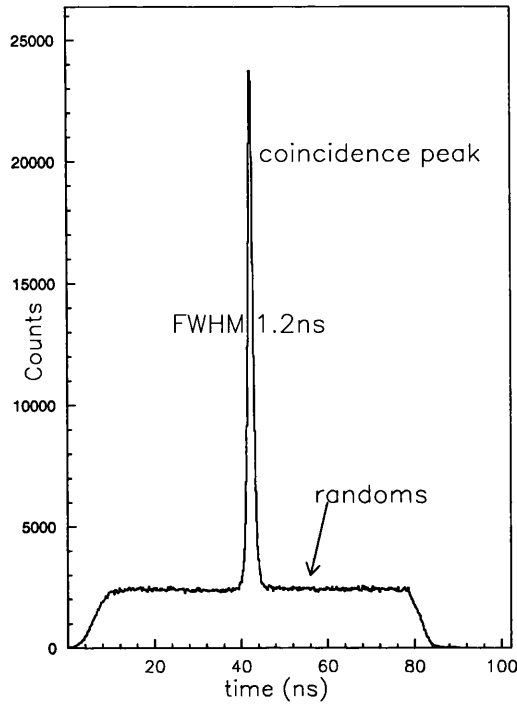


Figure 3.5: *Tagger time spectrum*

### 3.4.1 Postion Calibration

As shown in section 3.1.6 the particle position is related to the time difference between the signals from either end of a detector block by two calibration parameters. In PiP these coefficients can be obtained for the E blocks by exploiting the segmented design of the detector. By plotting the time difference spectra for each E block gated on the four PiP  $\Delta E$  elements and combining on one plot we can determine the intersections of the distributions. These intersections correspond to the joins in the PiP  $\Delta E$  elements, the exact positions of which are known. See Figure 3.6. The gradient parameter  $v/2$  in equation(3.13) is obtained by fitting a plot of position versus time difference. The converse process, gating on E blocks, is used to position calibrate the  $\Delta E$  elements.

The rise times needed for the walk corrections were taken from an experiment which ran concurrently with this measurement [51].

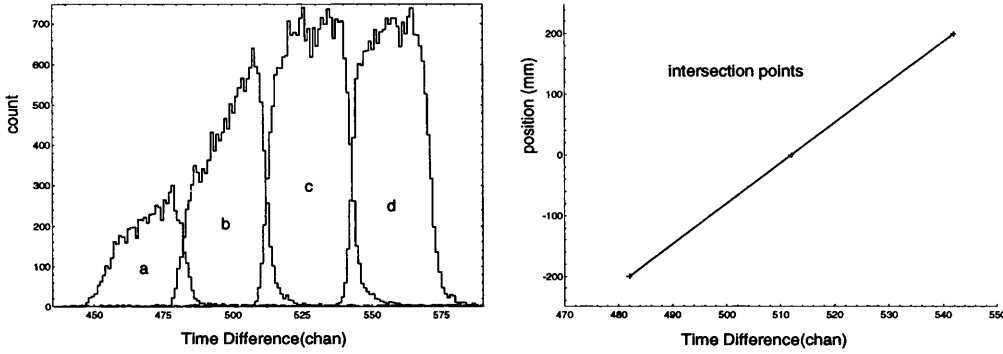


Figure 3.6: *Position calibration parameters*

### 3.4.2 Energy Calibration: the relation between pulse height and particle energy

The energy deposited by particles in the detector is obtained from the charge in the pulses which they produce. For a proton to reach PiP it must first travel through part of the target, the air, the scintillator wrappings and then the scintillator itself in all of which the proton will lose energy. To calculate the energy losses as a particle traverses a material, be it scintillator, target or air, the range method was used. The particle range in the given material is parameterised by:

$$R = aE^k \tag{3.16}$$

where R is the range and E is the particle energy. The coefficients a and k are medium dependent [52]. If  $E_i$  and  $E_f$  are the particle's initial and final energy respectively then the energy loss is:

$$E_{loss} = E_i - E_f \tag{3.17}$$

and the relationship between the incident and emergent particle energies is given by:

$$E_f = \left[ E_i^k - \frac{x}{a} \right]^{\frac{1}{k}} \tag{3.18}$$

where x is the thickness of the material.

The light output from the scintillator is converted to an electrical pulse by the PM tubes but the possibility of gain drifts in the PM tubes must be taken into consideration. Since cosmic muons are ultra-relativistic, minimum ionising particles, the energy they deposit in any PiP bar is proportional to the thickness of scintillator material traversed. Cosmic events therefore provide a stable source of light which can be used to measure the gain of each PM tube as a function of time. They can also be used to measure the attenuation along each block and to match the response of the D,E and F-layers to that of the C-layer.

The first task is to select out the cosmic events from all the other data by insisting that in each layer all four blocks register a valid hit because near vertical cosmic muons should enter the top of PiP and exit out the bottom tracing a path through all four blocks in the process. Once the angular dependence of the pathlength of the cosmic ray has been corrected for, the geometric mean of the pulse heights displays a characteristic Landau distribution which can be used to monitor and match the gains. The position of the mean channel of the geometric mean distribution provides a monitor of the gain drift. The dependence of the mean channel on the position along the block is used to determine the residual droop function,  $f_{droop}(x)$  [48] and is shown for a D-layer block on the left side of figure 3.7. The right side of figure 3.7 shows the mean of the Landau distribution for a single PM tube, averaged over the length of a C-layer block, as a function of time. The pulse height is seen to vary by  $\pm 1.4\%$  over the time period of a short experiment. The time variation of the average amplitude for each PM tube is corrected for on a file-by-file basis to reduce any loss of resolution due to gain drifts.

The energy calibration for PiP is obtained using the two body breakup reaction  $D(\gamma,p)n$ . The data are obtained in a separate run with a  $CD_2$  target. As the photodisintegration of deuterium has only two bodies in the final state, knowing

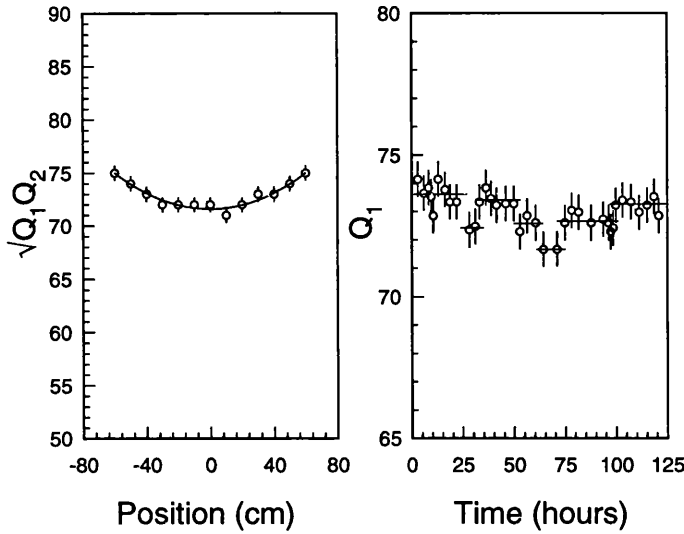


Figure 3.7: Cosmic muons provide a means of measuring the pulse height attenuation along each block and also of monitoring the stability of the gains of each PM tube

the photon energy and the proton angle completely defines the kinematics and the proton energy can be calculated from these variables. The proton's energy losses are taken into account as described above. The deuterium data extend up to proton energies of  $\sim 170$  MeV and allow calibration of the C and D-layers. Protons are selected as discussed in section 4.1. The nonlinearity of the light output at low proton energies is taken into account by converting the calculated proton energies into the equivalent electron energy [53]. For the C and D-layers, a plot of this calculated proton energy versus the observed gain matched pulse charge provides the necessary calibration parameters. Figure 3.8 is a plot of the calculated proton energy versus the proton energy measured by PiP; after calibration it shows that the response is linear. The background of events away from the ridge is due mainly to the  $C(\gamma,p)X$  reaction and other deuterium breakup channels above the pion production threshold.

As there is little yield from the  ${}^2\text{H}(\gamma,p)n$  reaction at proton energies above

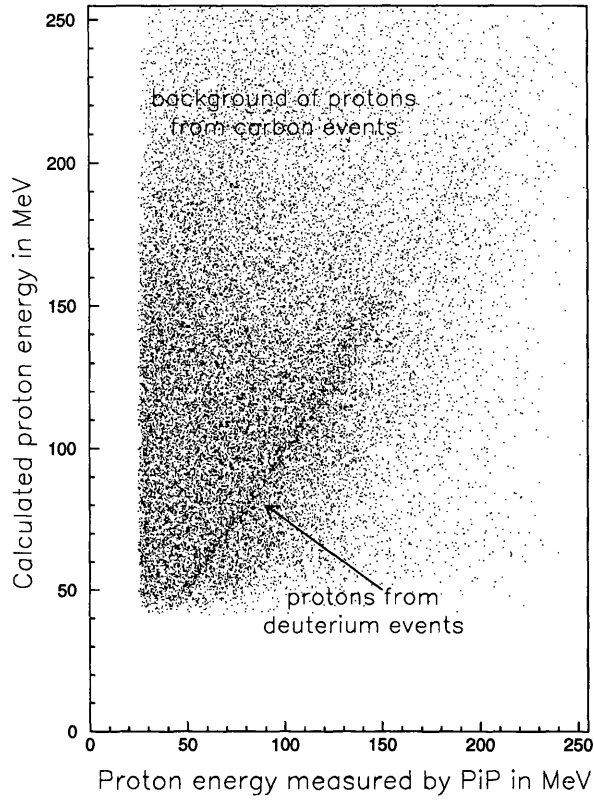


Figure 3.8: *Calculated proton energy (MeV) from deuterium kinematics vs the proton energy measured by PiP in MeV.*

~ 170 MeV using this method to calibrate the E-layer is difficult. Instead the E-layer was calibrated against the C and D-layers by using cosmic particles and matching the gains.

### 3.5 TOF

The TOF detector array covers the deuteron arm of the  $^{12}\text{C}(\gamma, \text{pd})$  measurement and the neutron arm of the deuterium breakup used for calibration purposes.

### 3.5.1 Position Calibration

By combining the physical position of a vertical TOF bar along with the hit position along the bar, the polar coordinates of a hit can be determined. The vertical hit position is also required to calculate the particle flight-path which in turn is used to evaluate the particle energy. To obtain the vertical position calibration a plot of the time difference spectrum is made. The extremes of the distribution correspond to the ends of the blocks. See figure 3.9. The physical

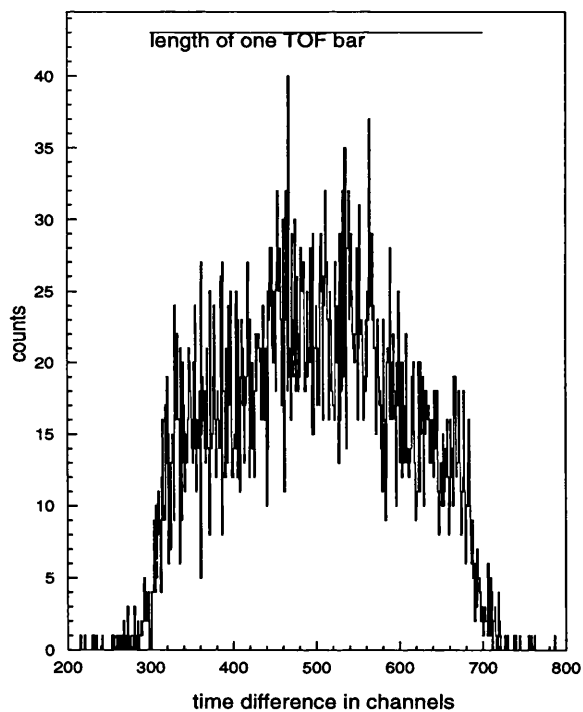


Figure 3.9: *TOF position calibration*

position of each bar with respect to the target is measured using an ultra-sound device.

### 3.5.2 Time of Flight

Particle energy is determined from time of flight. The particle time of flight from the target to the TOF array is:

$$tof = t_{mean} - t_{zero} \quad (3.19)$$

where  $t_{mean}$  is the walk and start corrected mean time (see section 3.2) from the TOF PM tubes and  $t_{zero}$  is the time corresponding to zero time of flight (i.e the time that would be recorded by the TDC if the TOF bar was located at the target) and therefore reflects the time due to cable delays and signal propagation times. The TOF walk corrections were obtained using LED flasher units [47]. The  $t_{zero}$  is obtained by first selecting neutral particles (see section 4.2.1) and then plotting the quantity:

$$t_{cal} = t_{mean} - \frac{flightpath}{c} \quad (3.20)$$

where  $c$  is the speed of light. An example is shown in figure 3.10. The sharp peak due to photons produced by atomic scattering in the target, gives the  $t_{zero}$  channel.

The particle kinetic energy,  $T$ , is determined from the flight path using relativistic kinematics as follows:

$$T = m(\gamma - 1) \quad (3.21)$$

where

$$\gamma = \frac{1}{\sqrt{1 - \beta^2}} \quad (3.22)$$

and

$$\beta = \frac{flightpath}{tof \times c} \quad (3.23)$$

Here  $m$  is the particle mass. While this is exact for neutral particles, charged particles like the deuteron continuously lose energy over the flight path and a

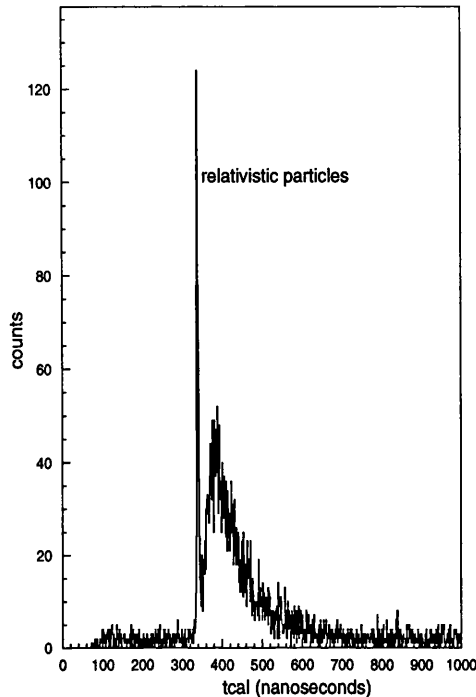


Figure 3.10: *TOF  $t_{zero}$  time-of-flight spectrum*

correction must be made for the fact that what is actually measured is not the particle's initial velocity but it's average velocity (see section 4.3).

### 3.5.3 Gain matching

Selection of deuterons is done by cutting on a plot of pulse height vs time of flight for the TOF detectors (see section 4.2). This requires the gain of each TOF bar to be aligned. The gain matching is done using the 'punch through' energy of protons, defined as the energy needed for the protons to pass through a TOF detector bar. For protons it is a constant and so it can be used as a reference point to align the gains of each PM tube [54].

## 3.6 Detector Performance

After calibration, comparison of measured and calculated quantities for the  $D(\gamma, pn)$  reaction also gives the energy and angular resolution of the detectors. The calibration parameters of PiP and TOF can be checked, cross-checked and fine tuned using the two-body breakup kinematics of the  $D(\gamma, pn)$  reaction. The kinematics of the two-body final state are fully defined in that once the photon energy and proton (or neutron) angle are known the other kinematic variables can be calculated by exploiting the conservation of energy and momentum. Before extracting any resolutions the background carbon events are separated from the deuterium breakup events. This is done using an observable called 'missing energy'.

### 3.6.1 Missing energy

For the  $(\gamma, pn)$  reaction the missing energy is defined as:

$$E_{miss} = E_{\gamma} - T_p - T_n - T_{recoil} = S + E_x \quad (3.24)$$

where  $E_{\gamma}$  is the photon energy,  $T_p$  and  $T_n$  are the kinetic energies of the proton and neutron, and  $T_{recoil}$  is the kinetic energy of the recoiling system.  $E_x$  is the excitation energy of the recoiling system and  $S$  is the separation energy for the reaction.

In deuterium breakup there is no recoil hence  $T_{recoil}$  and  $E_x$  are zero and the missing energy is simply the separation energy for the reaction:

$$S = m_p + m_n - M_D = 2.22 \text{ MeV} \quad (3.25)$$

Figure 3.11 shows the missing energy spectrum obtained from the  $CD_2$  target for  $E_{\gamma} = 110\text{-}400$  MeV. The peak at 2 MeV is due to the deuterium breakup. Its width arises from the overall resolution in energy. We can select the deuterium breakup events by cutting on this peak. The spectrum at higher missing energy,

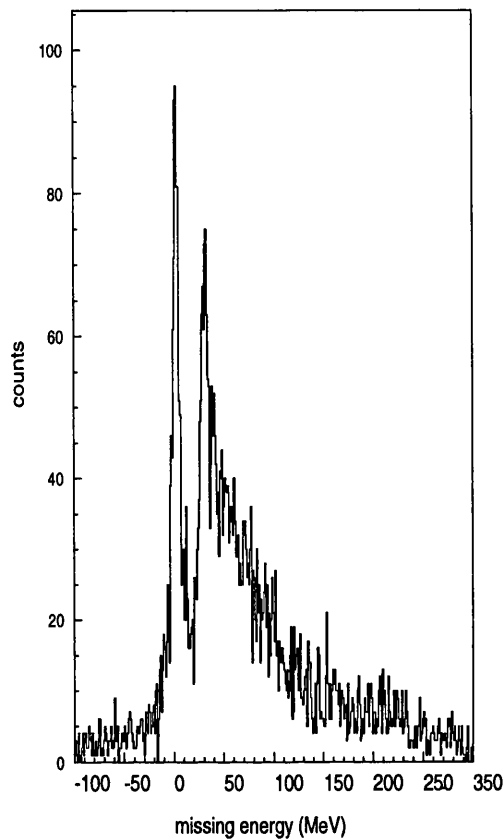


Figure 3.11:  $CD_2(\gamma, pn)$  missing energy spectrum

including the second peak at 28 MeV is from the carbon events. Replotting figure 3.8 with a cut on the deuterium peak in figure 3.11 now shows a much cleaner deuterium ridge. See figure 3.12

The resolution can be obtained by plotting the difference between the calculated and measured values. The best determined experimental parameters are the photon energy and the neutron angle. Using these two variables to calculate the proton energy and angle and plotting the difference between the measured and calculated values enables the proton energy and polar angular resolutions to be determined, see figures 3.13 and 3.14.

The TOF side neutron energy resolution is similarly determined, see Figure

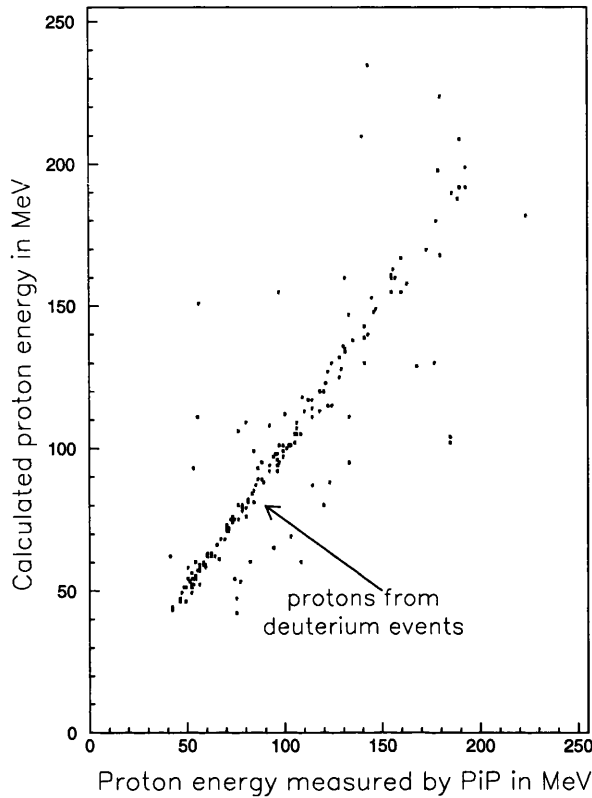


Figure 3.12: *deuterium ridge cut on missing energy*

3.15. There is expected to be a small improvement in the deuteron energy resolution arising from the fact that a deuteron will start scintillating immediately upon entering the detector whereas a neutron needs to produce secondary ionisation which may happen at any point along its path leading to an uncertainty in its flight path due to the 5cm thickness of a TOF bar.

The neutron polar angular resolution is defined by the 20cm width of a TOF bar which at average flight paths of 6m leads to a  $\theta_n$  resolution of about  $2^\circ$  (FWHM). The uncertainty in  $E_\gamma$  is  $\pm 1$  MeV. Both these uncertainties are then present in the quantities calculated above. The energy and angular resolutions are therefore not the intrinsic resolutions of the detectors. In order to extract the intrinsic resolutions of the PiP and TOF detectors we have to unfold these contributions.

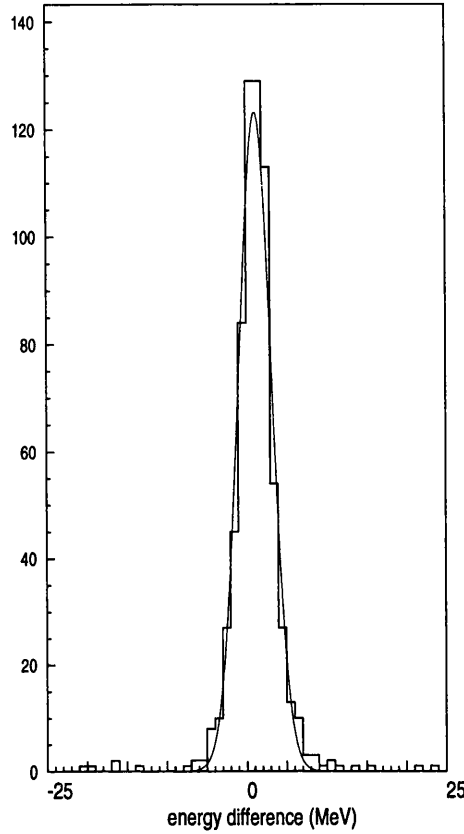


Figure 3.13: *PiP proton energy resolution for photon energies of 110MeV-400MeV, corresponding to proton energies of 30-330 MeV, particles stopped in any of the layers up to the E-layer, over the whole range of incident proton polar angle. The Gaussian fit gives FWHM = 4.5MeV.*

$$\sigma_{intrinsic} = \sqrt{\sigma_{measured}^2 - \sigma_{calculated}^2} \tag{3.26}$$

Where  $\sigma_{measured}$  is the measured resolution and  $\sigma_{calculated}$  is the uncertainty in the calculated quantity due to the uncertainty in  $E_\gamma$  and  $\theta_n$  and is obtained from

$$\sigma_{calculated}^2(x) = \left[ \left( \frac{\partial x}{\partial E_\gamma} \right) \Delta E_\gamma \right]^2 + \left[ \left( \frac{\partial x}{\partial \theta_n} \right) \Delta \theta_n \right]^2 \tag{3.27}$$

The proton azimuthal angular resolution  $\Delta\phi_p$  is obtained from an estimate of

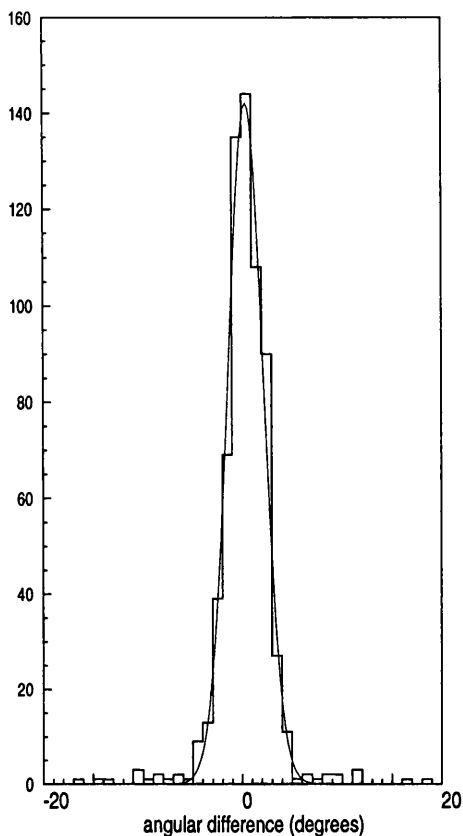


Figure 3.14: *PiP polar angular resolution for  $E_\gamma = 110\text{MeV}-400\text{MeV}$ . The Gaussian fit gives  $FWHM = 4.0^\circ$ .*

the vertical position resolution obtained from the overlap of the time difference spectra of the B-layer elements. It was found to be approximately  $5.4^\circ$  [51]. The neutron azimuthal angular resolution is obtained from the time difference spectrum of a TOF bar. The width of the rising edge at the ends of the bar gives an estimate of the vertical position resolution.  $\Delta\phi_n$  was found to be approximately  $1^\circ$ .

A summary of the detector performance is shown in table(3.1).

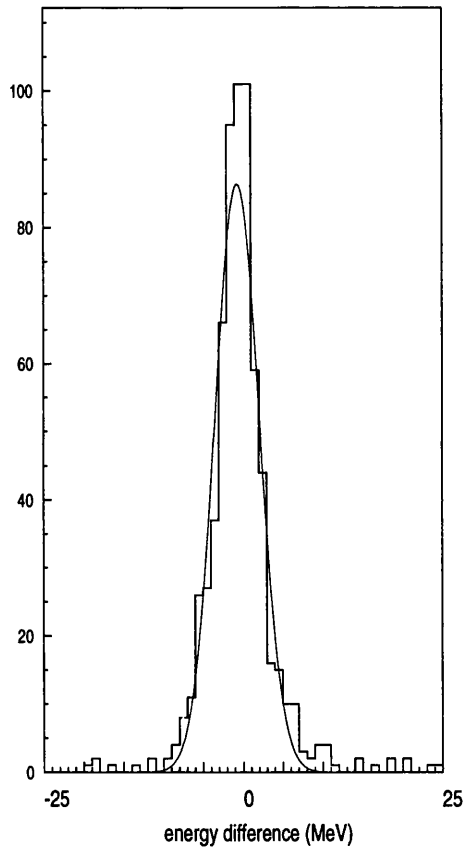


Figure 3.15: *TOF neutron energy resolution for photon energies of 110-400 MeV. The gaussian fit gives  $FWHM = 5.5MeV$ .*

Detector	Particle	Quantity	Acceptance	Resolution(FWHM)
Tagger	$\gamma$	$E_\gamma$	110MeV→400MeV	2 MeV
PiP	proton	$E_p$	30MeV→330MeV	4 MeV
		$fwd$	22.7° → 101.1°	3.5°
		$\theta_p \text{ cen}$	51.3° → 128.6°	
		$bck$	79.0° → 156.7°	
		$\phi_p$	+22.8° → -22.8°	5.4°
TOF	neutron/deuteron	$E_d$	≥ 45MeV	4 MeV
		$E_n$	≥ 17MeV	5 MeV
		$bck$	10.5° → 66.2°	~2.0°
		$\theta_{n,d} \text{ cen}$	39.6° → 95.4°	
		$fwd$	99.4° → 153.4°	
		$\phi_{n,d}$	162.5° → 192.7°	~1°
Combined	-	$E_{miss} (\gamma,pn)$	-	7 MeV
	-	$E_{miss} (\gamma,pd)$	-	6 MeV

Table 3.1: Summary of detector performance over the photon energy range 110MeV-400MeV . The resolutions quoted are the intrinsic values.

# Chapter 4

## Data Analysis

The procedures used in extracting the double arm differential cross sections for the  $^{12}\text{C}(\gamma, \text{pd})$  reaction are discussed in this chapter.

## 4.1 PiP Proton Selection

Although a  $\Delta E$ - $E$  plot like that of figure 2.16 can be used for particle identification in PiP, it is difficult to set up a consistent particle selection for all energies and the plots are contaminated with particles which have undergone inelastic hadronic interactions and consequently produce less scintillation light. The contamination is located below the main ridge and is energy dependent, making corrections complicated. In order to identify and then correct for the protons which have lost energy through inelastic collisions, a more systematic approach is required. The method only considers protons and pions.

For each particle type, the particle energy is calculated in two ways, first assuming the particle is a proton and then repeated assuming the particle is a pion.

- Calculated energy,  $E_{calc}$ : Starting with the energy deposited in the layer in which the particle stopped, the energy losses in the previous layers (including dead layers, wrappings etc.) are calculated back to the target using the range method discussed earlier.  $E_{calc}$  is then the particles' initial energy at the target.
- Measured energy,  $E_{meas}$ : The light output, converted into energy, from all the layers in PiP up to the stopping layer is added up, again with energy losses in the dead layers taken into account. This is the measured particle energy  $E_{meas}$ .

The particle identification is done by comparing the energies  $E_{calc}$  and  $E_{meas}$

for each particle type by defining the quantities:

$$E_{diff-proton} = E_{calc-proton} - E_{meas} \quad (4.1)$$

and

$$E_{diff-pion} = E_{calc-pion} - E_{meas} \quad (4.2)$$

For protons,  $E_{diff-proton} \approx 0$  while for a pion this quantity will be large because the calculated quantities (which assume the particle is a proton) will be mismatched with the measured light output. Similarly for pions,  $E_{diff-pion} \approx 0$  while being large for protons. However for events which have undergone an inelastic reaction energy loss, both these quantities are large because the energy-range relation cannot be met for protons or pions. Particle separation plots can be made by plotting  $E_{diff-pion}$  against  $-E_{diff-proton}$ . Figure 4.1 shows a typical particle separation plot of the difference between calculated and measured energy losses in the C-layer for particles stopping in the D-layer. As expected, there are three distinct regions in the plot, a proton region, a pion region and a region of inelastic events in between. By selecting on the appropriate region, using a simple one-dimensional cut, protons suffering little or no inelastic losses can be unambiguously separated from the pions and from the inelastic events. The lines indicate the energy acceptance windows used to reject those particles which have undergone inelastic losses. The window size was chosen to be  $\pm 7$  MeV which is twice the FWHM proton energy resolution for protons of energy 130 MeV. The yield of protons which have not undergone inelastic scattering is scaled up by a weight,  $\omega^{proton}$ , dependent upon the energy of the proton. These weights are produced in a simulation of the hadronic reactions of protons in PiP, using the GEANT package [56], which has shown that 3.5% of 50 MeV protons will undergo inelastic energy losses, rising to 26% for 200 MeV protons.

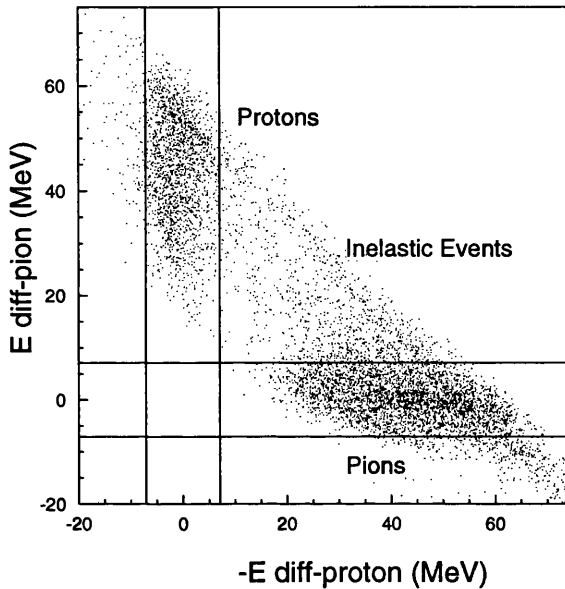


Figure 4.1: *Proton identification and selection is achieved by plotting the difference between calculated and measured energy losses assuming the particles are pions against the difference assuming that they are protons.*

## 4.2 TOF Deuteron Selection

Charged particles emerging from the target on the TOF side leave a signal in the  $\Delta E_{veto}$  detector array. Any coincidence between a  $\Delta E_{veto}$  signal and a particle in TOF is identified as a charged particle. Neutral particles will not leave a signal in the  $\Delta E$  array. The segmentation of the  $\Delta E_{veto}$  detector means that multiparticle events can be identified and analysed. Using events which register only one hit in the TOF array, the pattern of hits in the  $\Delta E$  ring for a hit in each individual TOF bar is used to determine which  $\Delta E$  elements lie in the path of each TOF

bar. In this way, charged hits are only analysed if a relevant  $\Delta E$  element has fired.

Once the gains of the TOF PM tubes have been matched (see section 3.5.3), the pulse heights from each bar in the charged particle trajectory are summed together and plotted against the time-per-metre as measured by the front bar. If the charged particle is sufficiently energetic it will punch through the front layer of TOF detectors, leaving signals in the layers behind. The possibility that these more energetic particles may scatter through appreciable angles is accounted for by tracking the particle through the TOF layers. Hits in a bar in the back layers are only classed as charged particles if the corresponding bar in the layer in front (going towards the target), or any of its directly adjacent neighbours also registers a hit. The time-of-flight used to calculate the particle energy is taken from the hit signal of the front TOF layer, the timing information from the back layers is made redundant. Figure 4.2 shows such a plot for a bank of TOF layers four deep, a so-called 'sail' plot. Deuterons, having a larger time-of-flight, for the same initial kinetic energy, than protons, are easily distinguishable, forming a deuteron 'ridge'. The selection of deuterons is achieved by cutting on this ridge.

In principle deuterons will also undergo hadronic interactions with the scintillator material and Measday and Schneider [58] have shown that up to particle energies of 100 MeV protons and deuterons exhibit comparable reaction loss cross sections. For the photon energies employed in this experiment the highest measured deuteron energy is  $\sim 120$  MeV. Deuterons of this energy are stopped in the first TOF layer after traversing up to a maximum of 5 cm of scintillator. Based on the results stated at the end of section 4.1 for protons in PiP, 1.8% of 50 MeV deuterons will undergo inelastic energy losses rising to 7.5% of 120 MeV deuterons. Although on the TOF side it is the particle time-of-flight which determines the particle energy, the pulse height is used for particle identification

and selection and a large enough degradation in energy may move the particle out of the selection window. The selection window around the deuteron ridge on the sail plot shown in figure 4.2 allows for an error of approximately  $\pm 25\%$  on the particle pulse height for a given time-of-flight. Hadronic reaction losses are therefore not a significant effect in the TOF detectors for this experiment and the efficiency of the TOF detectors in detecting deuterons is taken to be 100%.

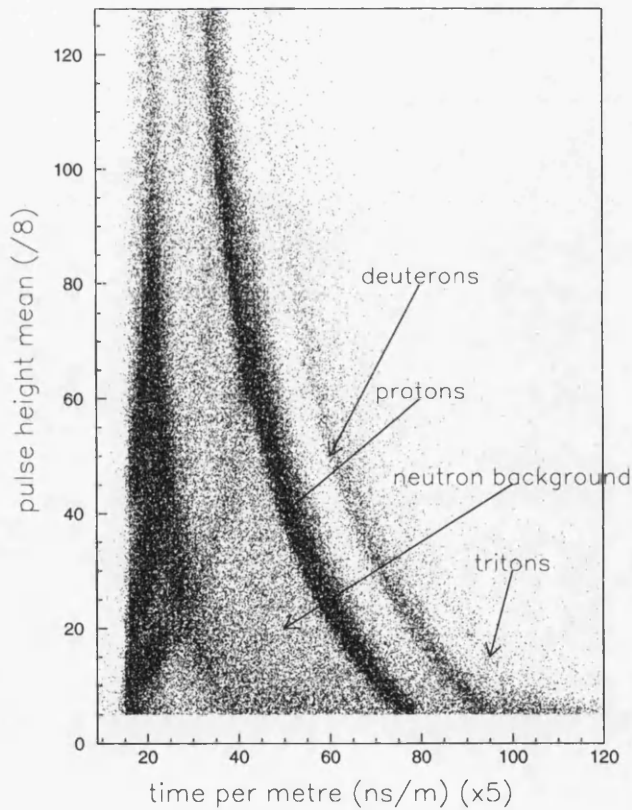


Figure 4.2: Deuteron identification and selection is achieved using plots of pulse height mean vs time per metre; so-called sail plots.

### 4.2.1 Neutron selection

The  $D(\gamma,p)n$  reaction used for calibration purposes requires a TOF side selection of neutrons. The first step is to accept any particles not classified as charged by the method above i.e the absence of a  $\Delta E_{veto}$  signal. Then, by imposing lower and upper thresholds on the time-of-flight to TOF, relativistic particles and random events can be rejected.

## 4.3 Deuteron Energy Loss Correction

As the deuterons fly towards TOF they lose energy in the target, the  $\Delta E_{veto}$  detectors and the air, resulting in a longer measured flight time than that of an uncharged particle of the same initial energy. This flight time then corresponds to an energy which has been 'averaged' over the flight path [59] and not to the initial kinetic energy at the target. To correct for this the initial kinetic energy of the deuteron is calculated from the 'average flight path' with the energy losses in the target and scintillators calculated using the range method described earlier.

## 4.4 Dealing with Randoms

Random events are detector hits not correlated with the photoreaction which generated the trigger. When the PiP trigger opens the gates for the tagger TDCs random electrons may fire the FPD elements and elements of the TOF array may also be fired by a random particle. The method of correcting for these random counts will now be discussed.

#### 4.4.1 Dealing with Randoms in the tagger

Figure 3.5 shows the tagger timing spectrum and as can be seen there are random events underlying the prompt peak of correlated tagger hits. To subtract these random events, three random regions are defined in the spectrum and the events

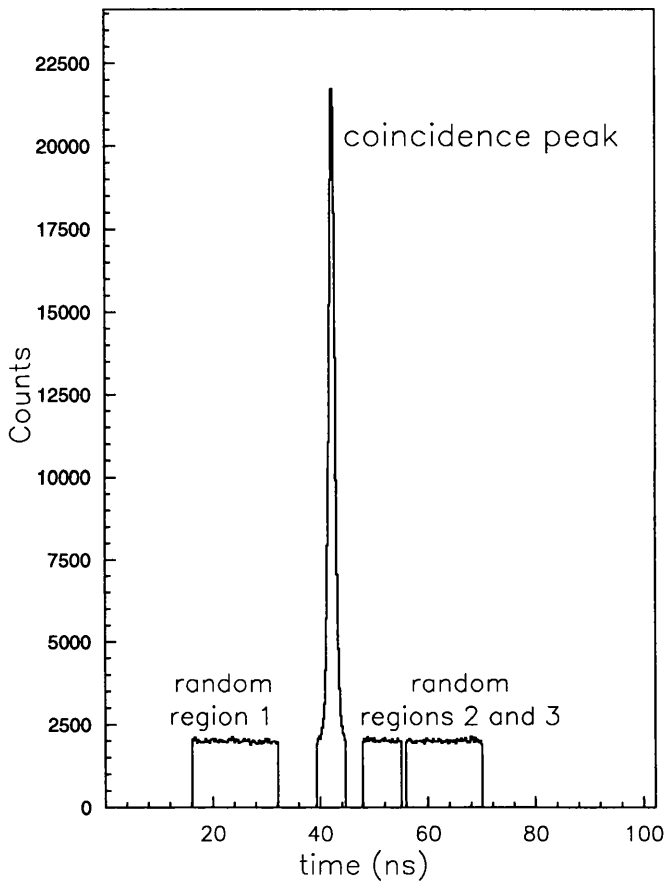


Figure 4.3: *Prompt and random regions in the tagger time spectrum*

in these regions are also analysed, see figure 4.3. A weight is assigned to the event according to the region it originated from and to the relative width of the regions:

$$w_{prompt}^{tagger} = 1.0 \quad (4.3)$$

$$w_{random}^{tagger} = \frac{-1.0 \times \Delta T_{prompt}}{\Delta T_{region1} + \Delta T_{region2} + \Delta T_{region3}} \quad (4.4)$$

In this way, random events are subtracted and the total spectrum corresponds to events correlated with the photoreaction.

#### 4.4.2 Randoms in the TOF Detector

The number of random events in the TOF detector was found to be very small. By cutting on a sail plot to select deuterons, the only random events present are those located under the deuteron ridge. In order to estimate the extent of these events, a similar cut was made in an unphysical region of the sail plot i.e in a region that could not correspond to particles produced in the photoreaction. Random events were found to be  $\sim 2\%$  at the most forward angles, falling to  $\sim 0.5\%$  at the more backward angles. The final cross sections were reduced by 1.25% to take account of this effect.

### 4.5 Tagging Efficiencies

The tagging efficiency  $\epsilon_{tag}$  is expected to be  $<100\%$  as the collimation of the photon beam will remove some of the photon flux. The tagging efficiency is measured as explained in section 2.3.3 and the result, plotted against the photon energy, is shown on figure 4.4. The small increase with photon energy results from a decreasing divergence of the photon beam with increasing photon energy, lessening the effect of the collimator and so allowing more photons to reach the target. A smooth curve was fitted to take account of the photon energy dependence.

### 4.6 Subevents

For each PiP trigger, the number of hits detected in the tagger on average exceeded one. Each of the detected hits can be treated as an individual event, called

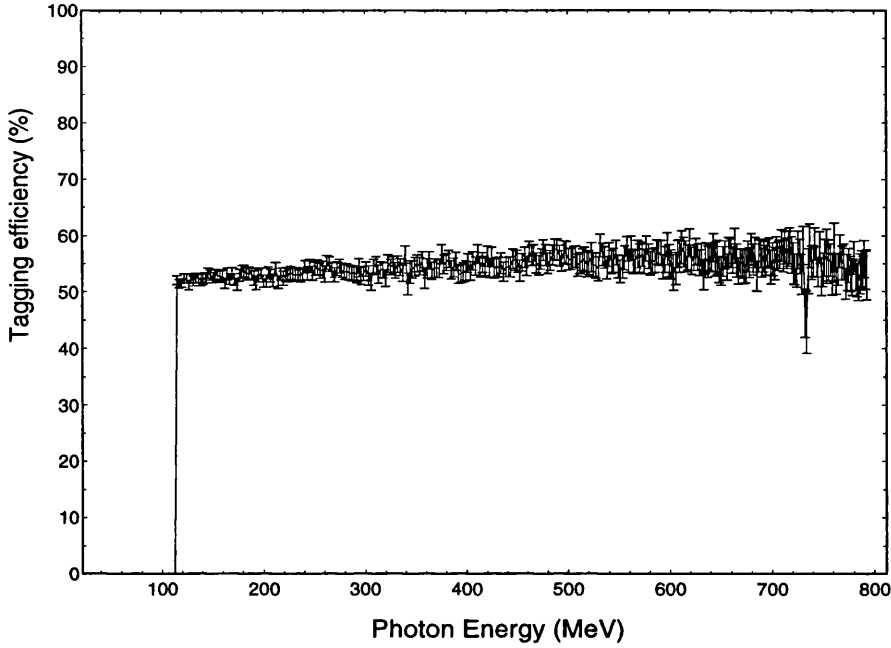


Figure 4.4: *tagging Efficiency as a function of Photon energy*

a subevent. The number of subevents for each trigger is:

$$N_{subevent} = N_{pip} N_{tof} N_{tagger} \quad (4.5)$$

where  $N_{pip}$ ,  $N_{tof}$  and  $N_{tagger}$  are the multiplicities in PiP, TOF the tagger respectively. For each analysed subevent a weight is calculated:

$$\omega^{subevent} = \omega^{tagger} \omega^{proton} \omega^{deuteron} \omega_{eff}^{photon} \quad (4.6)$$

where  $\omega^{tagger}$  is the weight due to the tagger hit and depends on whether the hit lies in the prompt or the random region as discussed above.  $\omega^{proton}$  takes account of the proton detection efficiency as discussed in section 4.1.  $\omega^{deuteron}$  is always one as discussed above but is included for clarity.

The tagging efficiency is also implemented using a weight  $\omega_{eff}^{photon}$ . For each tagger focal plane channel ( $i$ ), the number of photons reaching the target is given by

$$N_{\gamma} = N_e(i) \varepsilon_{tag}(i) \quad (4.7)$$

where  $N_e(i)$  is the total number of post-bremsstrahlung electrons detected in tagger focal plane channel ( $i$ ). This is treated as a photon weight

$$\omega_{eff}^{photon} = \frac{1}{N_e(i) \epsilon_{tag}(i)} \quad (4.8)$$

where  $1/\epsilon_{tag}$  is the photon tagging efficiency weight and  $1/N_e$  is the bremsstrahlung weight  $\omega_b$ . This takes into account the shape of the Bremsstrahlung photon energy distribution and corrects for the larger flux of photons at lower energies. For focal plane channel ( $i$ ) and a photon energy bin width of  $x$  channels:

$$\omega_b = \frac{1}{x N_e(i)} \quad (4.9)$$

giving a photon weight of:

$$\omega_{eff}^{photon} = \frac{1}{x N_e(i)} \cdot \frac{1}{\epsilon_{tag}(i)} \quad (4.10)$$

The histograms of the derived quantities for each subevent are incremented by  $\omega^{subevent}$ . The sum of  $\omega^{subevent}$  for all events gives the tagger random subtracted photoreaction yield with the effects of the Bremsstrahlung shape and the inelastic energy losses in PiP taken into account.

## 4.7 Background Corrections

The air around the target adds to the observed photoreaction yield and this contribution has to be taken into account. In order to measure this background, data was collected in runs where the target had been removed from the beam. These runs are analysed in an exactly similar way to those taken with the target in. The average contribution to the total yield from background was found to be  $\sim 1.5\%$ . Again the final cross sections were reduced by a suitable factor to take account of this effect.

## 4.8 Cross Section Derivations

The probability of a photoreaction, expressed as a cross section  $\sigma$ , is determined by measuring the yield of reaction products,  $Y$ . Once the necessary corrections for efficiencies, randoms and the bremsstrahlung shape have been made, the yield per incident photon is related to the cross section by

$$Y = n_{target} \cdot \sigma \quad (4.11)$$

where  $n_{target}$  is the number of target nuclei per unit area presented to the beam, and is given by:

$$n_{target} = N_A \cdot \rho_s / A \quad (4.12)$$

where  $\rho_s$  is the target thickness in mass per unit area normal to the photon beam,  $N_A$  is Avogadro's number and  $A$  is the atomic mass number of the target nucleus. Because the target is positioned at an angle  $\theta$  to the beam,

$$\rho_s = \frac{\rho}{\sin\theta} \quad (4.13)$$

where  $\rho$  is the target thickness in mass per unit area.

## 4.9 Experimental Uncertainties

This section describes the various factors contributing to the statistical and systematic uncertainty in the experimental results.

### 4.9.1 Statistical Uncertainties

Statistical errors reflect the fact that the experiment measures reaction probabilities. In the simplest case of a spectrum bin containing  $N$  counts, the associated statistical error is  $\sqrt{N}$ . However in this experiment the error is complicated by the

need to perform random subtractions and to correct for the detection efficiencies.

When a spectrum bin has a total weight  $W$ , for a sum of  $N$  counts:

$$W = \sum_{i=1}^N \omega_i^{subevent} \quad (4.14)$$

where  $\omega^{subevent}$  is given in equation 4.6, the associated statistical uncertainty of the sum  $W$  is:

$$\Delta W = \sqrt{\sum_{i=1}^N (\omega_i^{subevent})^2} \quad (4.15)$$

This reduces to the simple  $\sqrt{N}$  case above when all the weights are unity. The statistical error can be reduced by collecting more data or by presenting the data in larger bin widths.

## 4.9.2 Systematic Uncertainties

Systematic errors arise from uncertainties in the calibration procedures and are assessed individually. The most important are:

- The average error in the tagging efficiency,  $\varepsilon_{tag}$ , over the photon energy range, was found to be  $\sim 1.5\%$  [60].
- The target was precisely weighed and measured and therefore the error in the target thickness is negligible. The target angles are set with a computer controlled stepping motor. This contribution is estimated to be  $< 1\%$ .
- The uncertainty in the corrections for proton inelastic energy losses arising from the positioning of the cuts on plots like figure 4.1. This contribution is estimated to be  $\sim 2.5\%$ .

## 4.10 Monte Carlo Simulations of the Experiment

Monte Carlo simulation programs based on two models of the  $(\gamma, pd)$  reaction have been written in order to make comparisons with the experimental distributions. The events generated in both models are sorted into spectra of various kinematic variables on the condition that the nucleons are emitted into the solid angles defined by the detectors and that their energies are within the detector energy acceptances.

### 4.10.1 3N Photon Absorption Model

This model calculates the momenta of the proton and deuteron emitted from the target nucleus following direct photon absorption on a three nucleon cluster (3N), assuming that the residual nucleus takes no part in the interaction. The Monte Carlo event generator first chooses the photon energy, at random, weighted by the energy dependent cross section for the  ${}^3\text{He}(\gamma, pd)$  reaction (see section 4.10.2). The next variable to be chosen is the magnitude of the 3N momentum vector, selected from a distribution of  $P^2F(P)$  where  $P$  is the momentum vector and  $F(P)$  is a form factor describing the probability of finding three nucleons at zero separation with total momentum  $P$  (see Appendix A). The 3N momentum distributions for two possible combinations of initial shells (ppp and pps) were derived by folding together the single nucleon momentum distributions. The direction of  $P$  is chosen isotropically. Assuming that the recoil nucleus is a spectator to the reaction and that there are no final state interactions, the recoil nucleus then has momentum  $-P$  with a corresponding kinetic energy  $T_{recoil}$ .

The next step is to transform the vectors to the centre-of-mass frame of the photon-3N system defined as that frame in which the total momentum of the

photon and the 3N cluster is zero. The total energy of the 3N cluster, assuming a spectator model, is implied through energy conservation to be:

$$E_{3N} = M_{target} - (M_{recoil} + T_{recoil} + E_x) \quad (4.16)$$

where  $M_{target}$  and  $M_{recoil}$  are the rest mass energies of the target and recoil nucleus respectively.  $E_x$  is the residual nucleus excitation energy and is chosen from a distribution which is adjusted until the prediction of the model agrees with the experimental distribution. The outgoing nucleon momenta can now be evaluated by exploiting the conservation of energy and momentum where the nucleon directions are selected randomly from the known angular distribution of the  ${}^3\text{He}(\gamma, \text{pd})$  reaction (see below). The momenta are then transformed back into the laboratory frame.

#### 4.10.2 The ${}^3\text{He}(\gamma, \text{pd})$ cross section

A phenomenological function is used to fit the proton angular differential cross sections from the  ${}^3\text{He}(\gamma, \text{pd})$  reaction in the photon energy range 140-400 MeV. These cross sections are obtained from the work of [5]. The differential cross section in the centre of momentum (CM) frame, for a particular photon energy, is represented by a fourth order Legendre polynomial expansion:

$$\frac{d\sigma}{d\Omega} = \sum_{l=0}^4 A_l(E_\gamma) P_l(\cos \theta) \quad (4.17)$$

where  $\theta$  is the CM angle between the incident photon and outgoing proton. The energy dependence of the  $A_l$  coefficients was fitted using the phenomenological form:

$$A_l(E_\gamma) = C_1 e^{C_2(E_\gamma - C_3)} + C_4 e^{C_5(E_\gamma - C_6)} \quad (4.18)$$

where  $C_{1-6}$  are parameters in the fit. From this parameterisation we can extract the  $(\gamma, \text{pd})$  reaction cross section, used to weight the photon distribution, and the proton angular differential cross section, used in selecting the proton angle.

### 4.10.3 The Pickup Model

This model assumes an initial  $^{12}\text{C}(\gamma, \text{pn})$  reaction followed by an  $n(\text{p}, \text{d})$  pickup reaction in the final state. The basis of the model is a direct two nucleon absorption,  $(\gamma, \text{pn})$  reaction and is described in reference [19]. In this model the residual nucleus excitation energy is chosen from a distribution of missing energies based on the experimental distribution of the  $^{12}\text{C}(\gamma, \text{pn})$  reaction. The magnitude of the picked-up protons' momentum vector is selected at random from a  $1p_{\frac{3}{2}}$  proton momentum distribution and its direction is selected isotropically. The work of Watson *et al.* [62] has established that the highest cross section for pairs of final state nucleons to be strongly correlated arises for low relative momentum between the pair. In order to select events in which the outgoing neutron and the picked-up proton have low relative momentum, the model only accepts those events where the magnitude and direction of the momentum of the proton are closely matched ( $\pm 25$  MeV/c in magnitude and  $\pm 10^\circ$  in both theta and phi directions) to that of the outgoing neutron. The angle and energy components of the outgoing neutron calculated on the basis of the 2N model are added vectorially to those of the picked-up proton, creating a deuteron in the final state.

## **Chapter 5**

### **Results and Discussion**

## 5.1 Introduction

In the present study of the photodisintegration of  $^{12}\text{C}$ , in the photon energy range 110-400 MeV, a significant number of coincident proton-deuteron pairs has been detected and a prominent back-to-back correlation has been observed. This correlation is shown on figure 5.1 which plots the opening angle between the outgoing proton-deuteron pairs in the centre of momentum frame of the photon and a stationary  $^3\text{He}$ , for different photon energy regions. Moving to this frame removes the forward boost given to the particles by the photon in the laboratory frame but leaves the spreading due to the initial motion of the  $^3\text{He}$  cluster in the nucleus. It should be noted that, to a certain extent, the opening angle distributions are constrained by the limited detector coverage. The opening angle correlations are reminiscent of those observed in the dominant  $(\gamma, \text{pn})$  yield (quasideuteron) where back-to-back emission of a proton and neutron implies a direct absorption of the photon on the proton-neutron pair as the A-2 system spectates. A similar correlation amongst proton-deuteron pairs suggests the possibility of a quasi- $^3\text{He}$  process, in which the photon is directly absorbed on a  $^3\text{He}$  cluster inside the  $^{12}\text{C}$  nucleus, as the A-3 system spectates. The direct absorption of a photon on a 3N cluster would indicate three-body interactions in the nucleus. However the photon interaction with a 3N cluster may not be the only or even the major absorption mechanism; the reaction may, for example, be an initial  $(\gamma, \text{pn})$  event followed by  $(\text{n}, \text{d})$  pickup in some final state interaction. The results presented in this chapter are an attempt to learn more about the way in which this reaction proceeds.

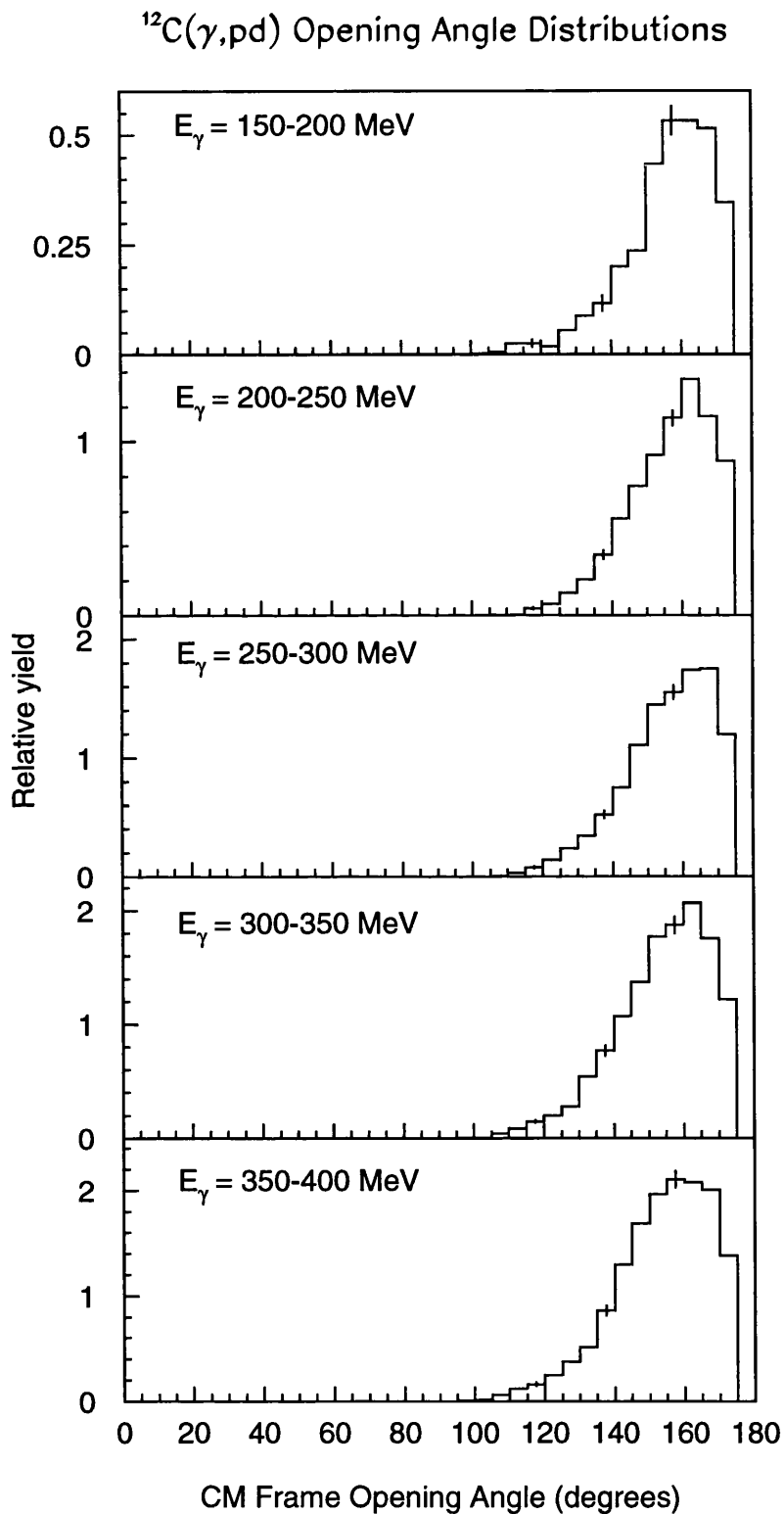


Figure 5.1: *Opening Angle distributions for the  $^{12}\text{C}(\gamma, \text{pd})$  reaction in the centre of momentum frame of the photon and a stationary  $^3\text{He}$ . Sample error bars show the statistical errors.*

## 5.2 Missing Energy

Missing energy plots give information about the excitation energy distribution of the residual system. The missing energy for the  $(\gamma, pd)$  reaction is defined as

$$E_m = E_\gamma - T_p - T_d - T_R = S_{pd} + E_x \quad (5.1)$$

where  $E_\gamma$ ,  $T_p$  and  $T_d$  are respectively the energies of the tagged photon and the detected proton and deuteron.  $T_R$  is the recoil kinetic energy of the residual system and is calculated from  $E_\gamma$ ,  $T_p$  and  $T_d$  utilising the conservation of energy and momentum.  $E_x$  is the excitation energy of this (undetected) recoiling system.

$S_{pd}$  is the separation energy, the threshold energy for the reaction to occur and can be calculated for  $(\gamma, pd)$  using

$$S_{pd} = m_p + m_d + m_{9Be} - m_{12C} \quad (5.2)$$

where  $m$  are the respective rest masses,  $m_{12C}$  being the rest mass of the target nucleus, and for  $^{12}\text{C}(\gamma, pd)$   $S_{pd} = 31.68$  MeV.

If the photon is absorbed directly on a correlated 3N cluster then we would expect to see a value for the missing energy corresponding to the separation energy, smeared by the detector resolution, with the residual nucleus left in or near its ground state. Higher missing energies indicate that the recoiling system has been left in an excited state but can also arise from final state interactions when the initial reaction products interact with the remaining nucleons as they leave the nucleus. Interactions resulting in the emission of more than the two detected particles and processes involving pion production, for example, will also result in higher values of missing energy. Figure 5.2 shows the missing energy distributions for the  $^{12}\text{C}(\gamma, pd)$  reaction for PiP positioned at central angle. The detector setups are discussed in section 2.5 and are shown schematically on figures

2.7-2.9. As can be seen for photon energies in the range 150-200 MeV there is a prominent peak at threshold indicating that the residual nucleus has often been left in or near its ground state suggesting that it has been a spectator to the reaction. At higher photon energies the peak becomes less prominent and we see strength at higher missing energies indicating multi-particle processes. As a comparison, figure 5.3 shows the results from a previous Glasgow study [22] of the  $(\gamma, pn)$  and  $(\gamma, pp)$  reactions in  $^{12}\text{C}$  with a similar experimental setup. Again we see a peak at threshold for the pn case but not for the pp case. In the pp case the photon cannot, to first order, be absorbed directly on two correlated protons because of the absence of any single meson exchange current (two interacting protons can exchange a single neutral pion but can also exchange two oppositely charged pions, providing a current to which the photon could couple, although this is much less probable); it is therefore no surprise that final state interactions are relatively more important. The similarity of the structure observed in the missing energy distributions for the  $^{12}\text{C}(\gamma, pd)$  and  $^{12}\text{C}(\gamma, pn)$  reactions would suggest that the  $(\gamma, pd)$  channel also proceeds via a direct knockout reaction.

Figures 5.4 and 5.5 show the missing energy distributions for the  $^{12}\text{C}(\gamma, pd)$  reaction at the backward and forward proton angle detector geometries respectively. At the backward angle it can be seen that there is less strength concentrated at low missing energy than is the case at central angle. An enhancement in relative strength at higher missing energies in comparison to central angle is also observed. These observations become more marked as the photon energy increases; indeed there is a distinct difference in shape between the distributions for each angle for photon energies greater than 250 MeV.

In contrast, at the forward proton angle detector geometry, there is a significant increase in relative strength at lower missing energies to the extent that there is still an observable peak at threshold up to photon energies in the region

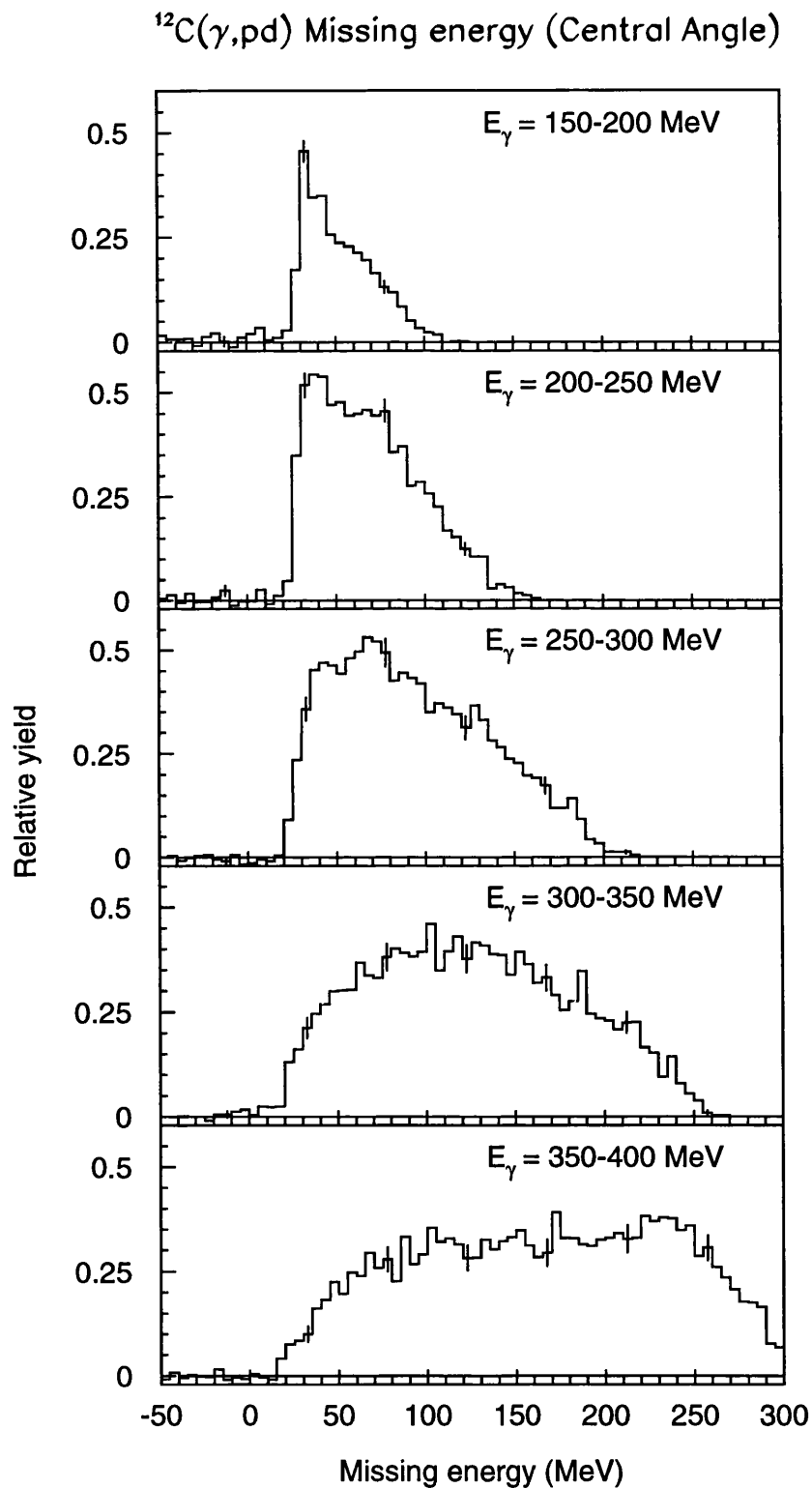


Figure 5.2: Missing energy distributions for the  $^{12}\text{C}(\gamma, \text{pd})$  reaction at central proton angles. Sample error bars show the statistical errors.

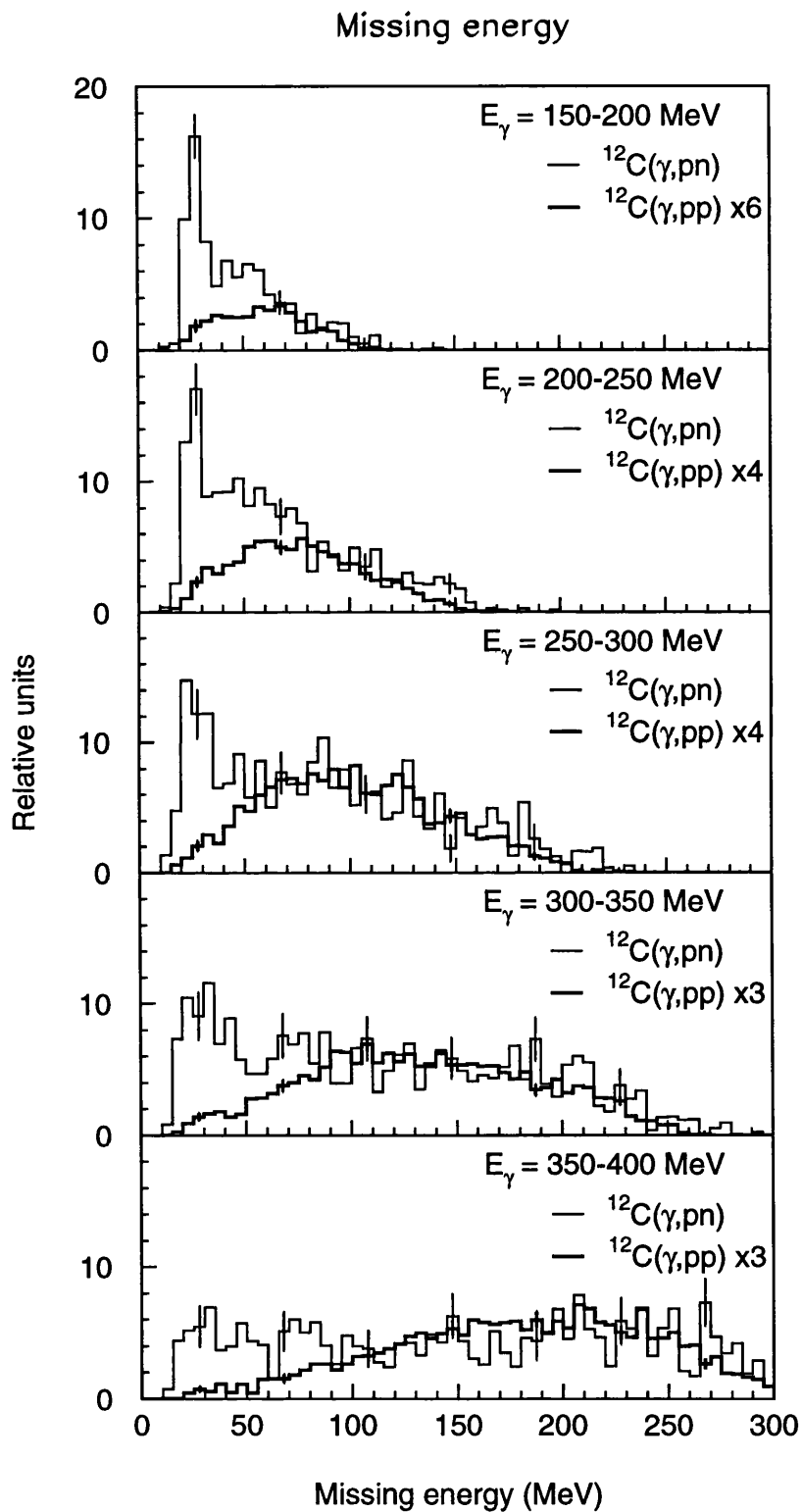


Figure 5.3: Missing energy distributions for the  $^{12}\text{C}(\gamma, pn)$  and  $(\gamma, pp)$  reactions. Sample error bars show the statistical errors.

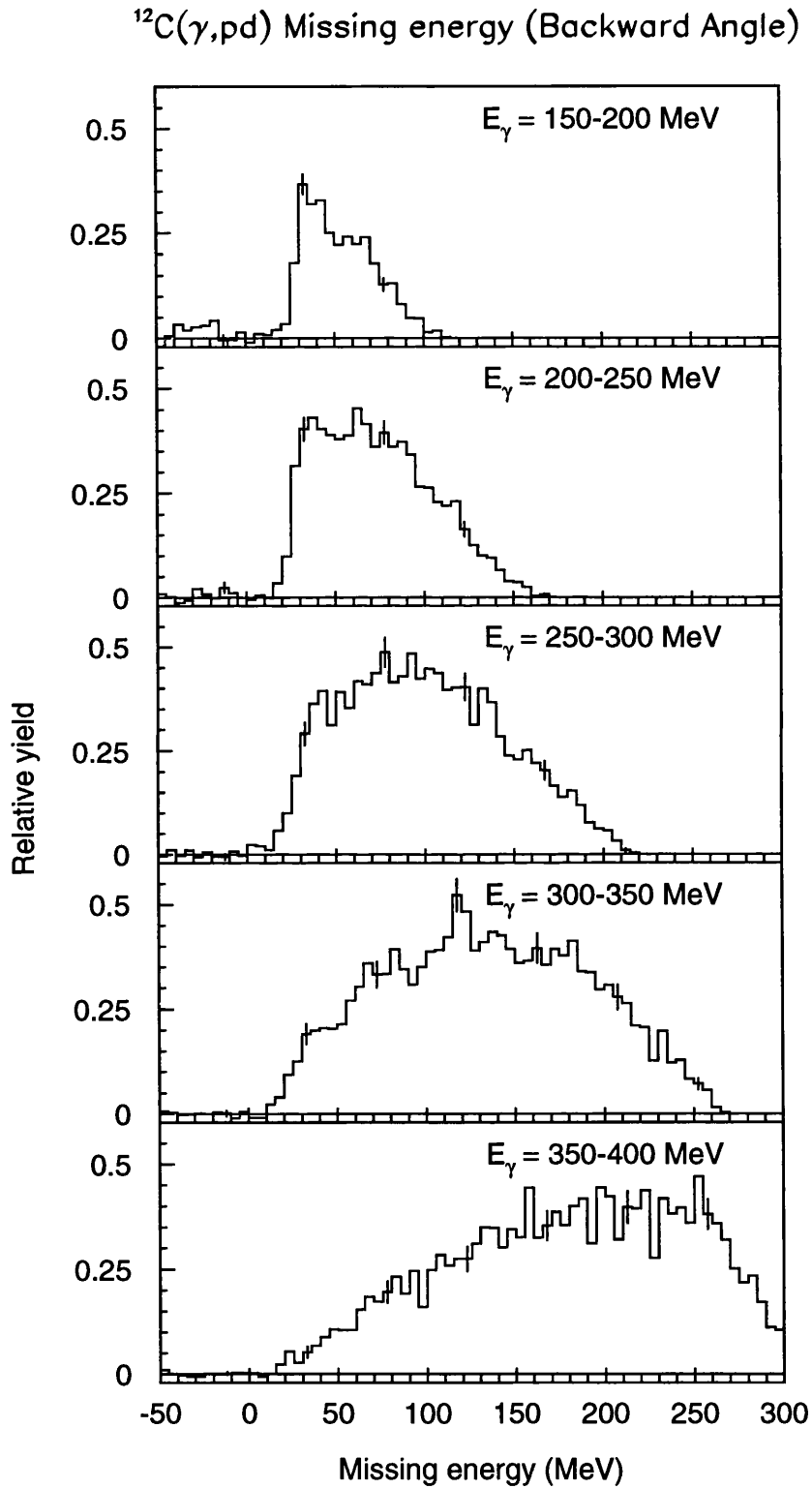


Figure 5.4: Missing energy distributions for the  $^{12}\text{C}(\gamma, \text{pd})$  reaction at backward  $\text{PiP}$  angle detector geometry. Sample error bars show the statistical errors.

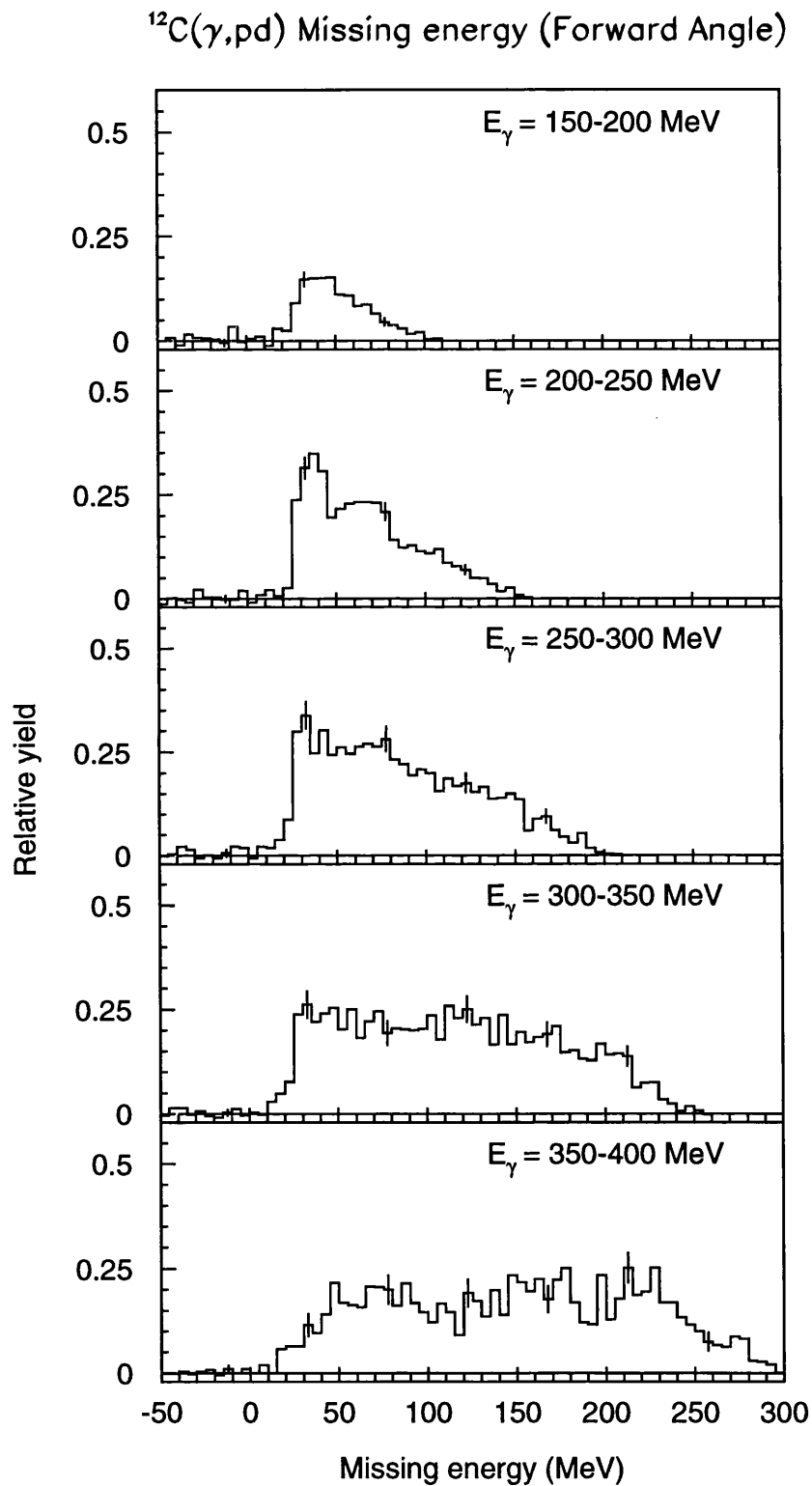


Figure 5.5: Missing energy distributions for the  $^{12}\text{C}(\gamma, pd)$  reaction at forward  $PiP$  angle detector geometry. Sample error bars show the statistical errors.

250-300 MeV. In comparison to the backward and central proton angle geometries there is much less strength at higher missing energies and the shapes of the distributions from 250 MeV onwards are quite different.

This shifting in relative strength from high to low missing energies as we move through from backward to forward angle geometries can be seen more clearly on figure 5.6 which is a superposition of the missing energy distributions from all three detector geometries. It is an indication that more than one reaction mechanism contributes and that their relative importance changes with proton angle.

There is a noticeable bump in the all the distributions up to photon energies of 300 MeV for missing energies of  $\sim 50$ -80 MeV. It is especially prominent in the forward proton angle data for photon energies between 200 and 250 MeV. This consistent feature of the data is not well understood but may be due to the involvement of one or two s-shell nucleons.

### 5.3 Missing Momentum

A qualitative indication of the reaction mechanism can be obtained from plots of missing momentum which reconstruct the momentum of the recoiling system on an event-by-event basis and allow a check on whether the recoil system is a spectator to the reaction. Events in which the photon has been directly absorbed by the detected particles, leaving the residual system unaffected, will usually result in lower values of missing momentum than those events in which further undetected particles have been emitted. As the photon energy increases so does the probability that more particles will be involved in the interaction, above the  $\sim 140$  MeV pion production threshold, for example, pion processes become more important and these can lead to a pion being absorbed by a nucleon pair with

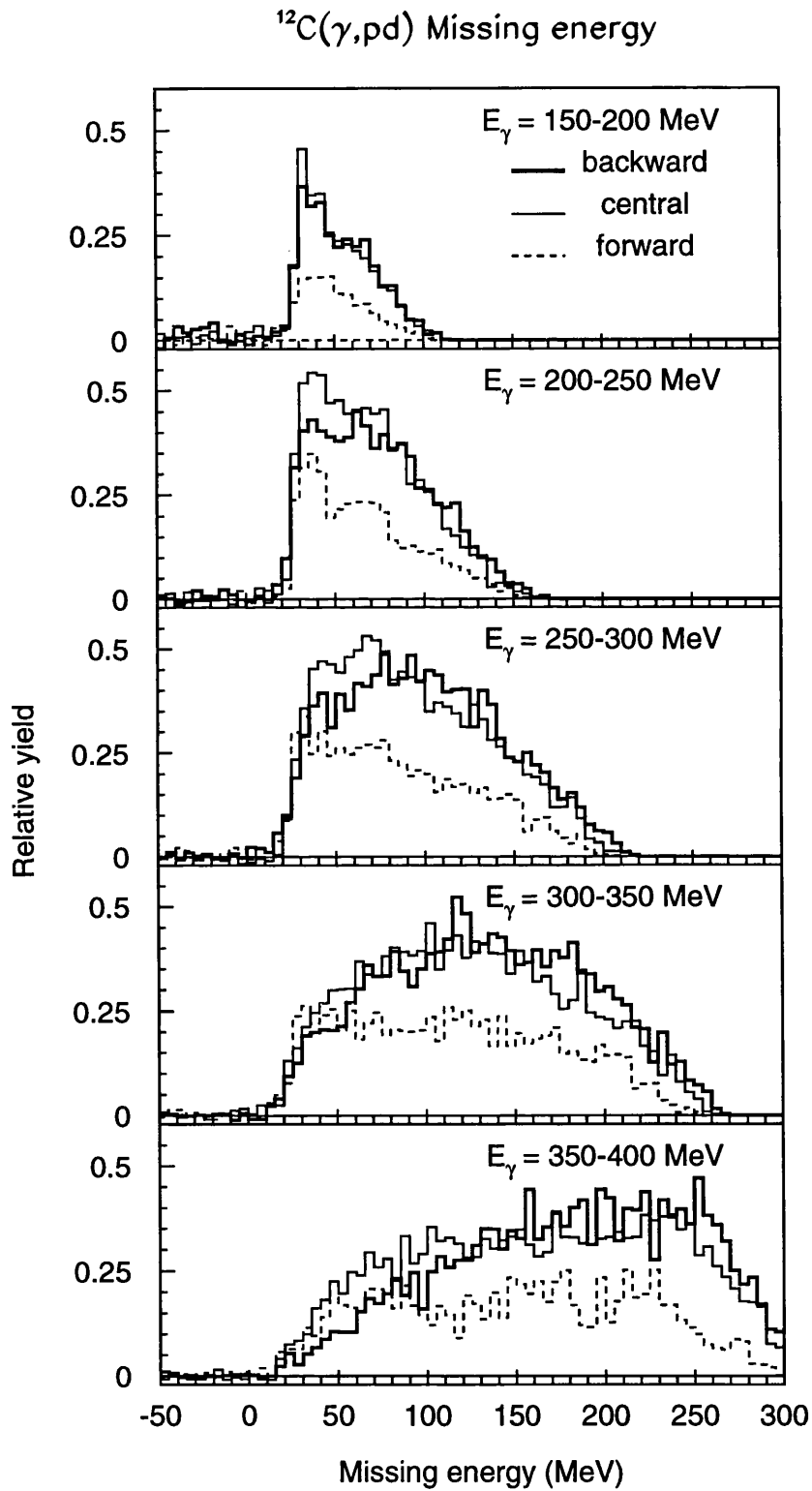


Figure 5.6: Superposition of the missing energy distributions for each detector setting for the  $^{12}\text{C}(\gamma, \text{pd})$  reaction.

one of the emitted pair undetected, which will result in a higher value of missing momentum. It is expected then that as the photon energy increases the average value of the missing momentum will increase also. However, it should be noted that in a spectator model the momentum distribution is independent of photon energy. For the  $(\gamma, pd)$  reaction the missing momentum is defined as

$$\mathbf{P}_{missing} = \mathbf{P}_{\gamma} - \mathbf{P}_p - \mathbf{P}_d \quad (5.3)$$

where  $\mathbf{P}_{\gamma, p, d}$  are respectively the measured photon, proton and deuteron momenta. In a spectator model, assuming there are no final state interactions, the initial momentum of the proton-deuteron pair (or 3N cluster)  $\mathbf{P}$  is equal to  $-\mathbf{P}_R$ , the momentum of the recoiling system, which is equal to  $\mathbf{P}_{missing}$ . Therefore the  $\mathbf{P}_{missing}$  distribution can be usefully compared with model predictions derived from wave functions of the three nucleons making up the 3N cluster, see section 4.10 and Appendix A. By examining the  $F(P)$  distribution for three interacting particles shown in Appendix A on figure A.3 it can be seen that there is a small probability of large  $P$ . Significant strength at these large values of  $P$  must correspond to final state interactions or processes involving more than the detected particles. Figure 5.7 shows the missing momentum distributions for the  $^{12}\text{C}(\gamma, pd)$  reaction at central proton angles. The distributions are shown for low missing energy,  $E_m < 44$  MeV, corresponding to excitation energies of up to 13 MeV where the particles involved are assumed to come exclusively from the p shell [19]. Figures 5.8 and 5.9 show the missing momentum distributions, also for low missing energy, for the backward and forward angle PiP geometries respectively.

The forward angle distributions again exhibit a significant change in both shape and average momentum when compared to those for the more backward angle geometries. The average recoil momentum is around 250 MeV/c, a distinct increase on the more backward geometries which exhibit an average recoil mo-

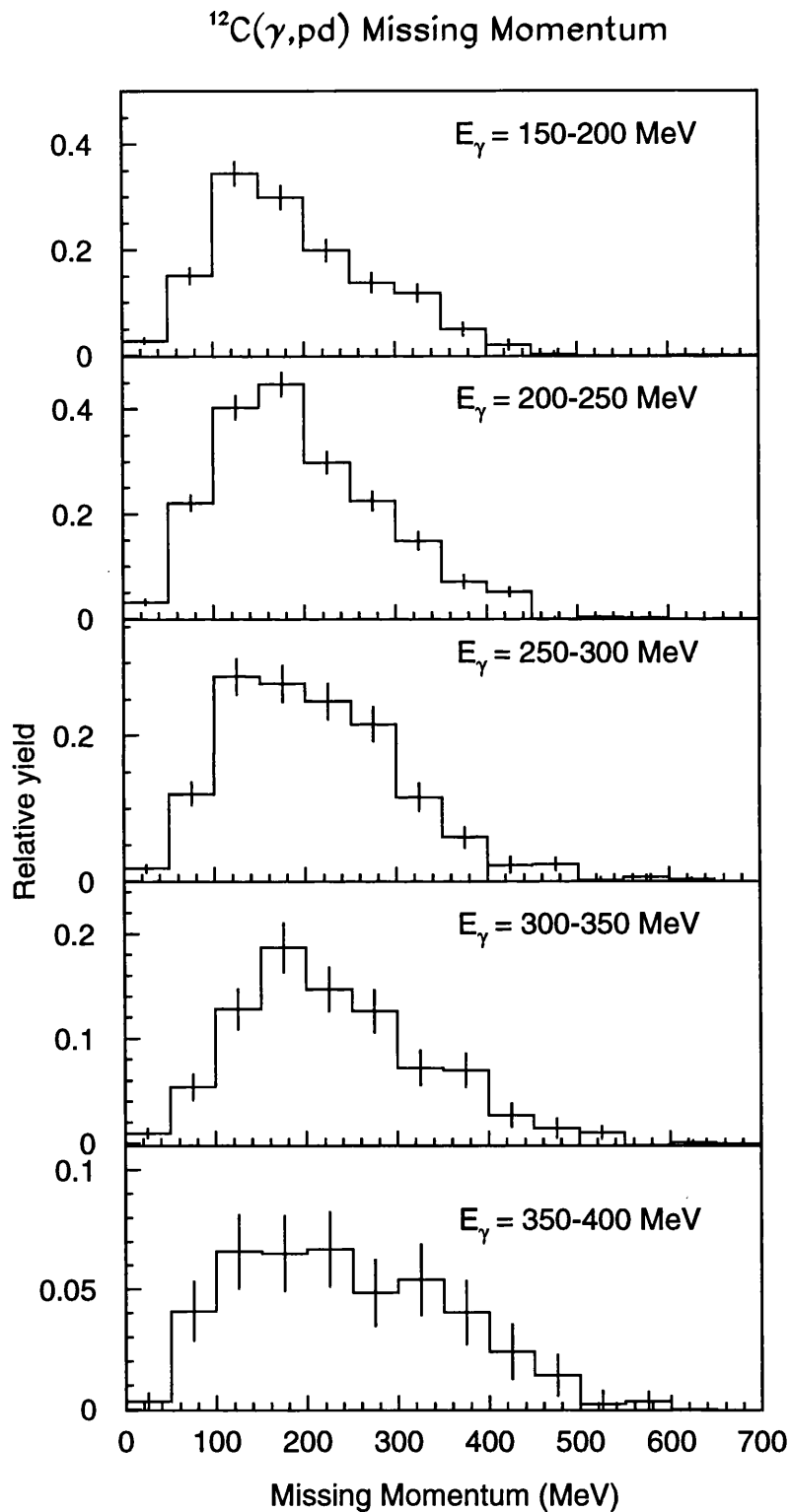


Figure 5.7: Recoil momentum distributions for the  $^{12}\text{C}(\gamma, \text{pd})$  reaction at the central  $\text{PiP}$  angle detector geometry for low missing energy,  $E_m < 44$  MeV. Sample error bars show the statistical errors.

mentum of  $\sim 150$  MeV/c. Unlike the backward and central angles, the forward angle missing momentum distributions exhibit a decrease in the average recoil momentum with increasing photon energy. Also at the more backward angles there is little change in the shape of the distributions as the photon energy increases whereas at the forward angle geometry there is a more marked change in shape between each photon energy bin. This reinforces the suggestion that the relative importance of the reaction mechanisms are changing with proton angle.

As expected the extent of the missing momentum distributions increases with increasing photon energy, indicating that final state interactions and multi-particle processes are playing an increasingly important role.

For the higher missing energy region,  $44 \leq E_m \leq 70$  MeV, where one or more of the particles can come from the s shell, figures 5.10, 5.11 and 5.12 again show the recoil momentum distributions for each detector geometry. For low photon energies the average recoil momentum increases as we move from backward through to central angle and then more distinctly again as we go to forward angle, mirroring the pattern for the lower missing energy region. In the higher photon energy regions the average recoil momentum is similar at all angles. As before, at the backward angle geometry the average recoil momentum increases with increasing photon energy as it does at the central angle, although to a lesser degree while at the forward angle the average value decreases with increasing photon energy. It should also be noted that in all photon energy regions the recoil momenta distributions at forward angle have a wider extent than those of the more backward angles.

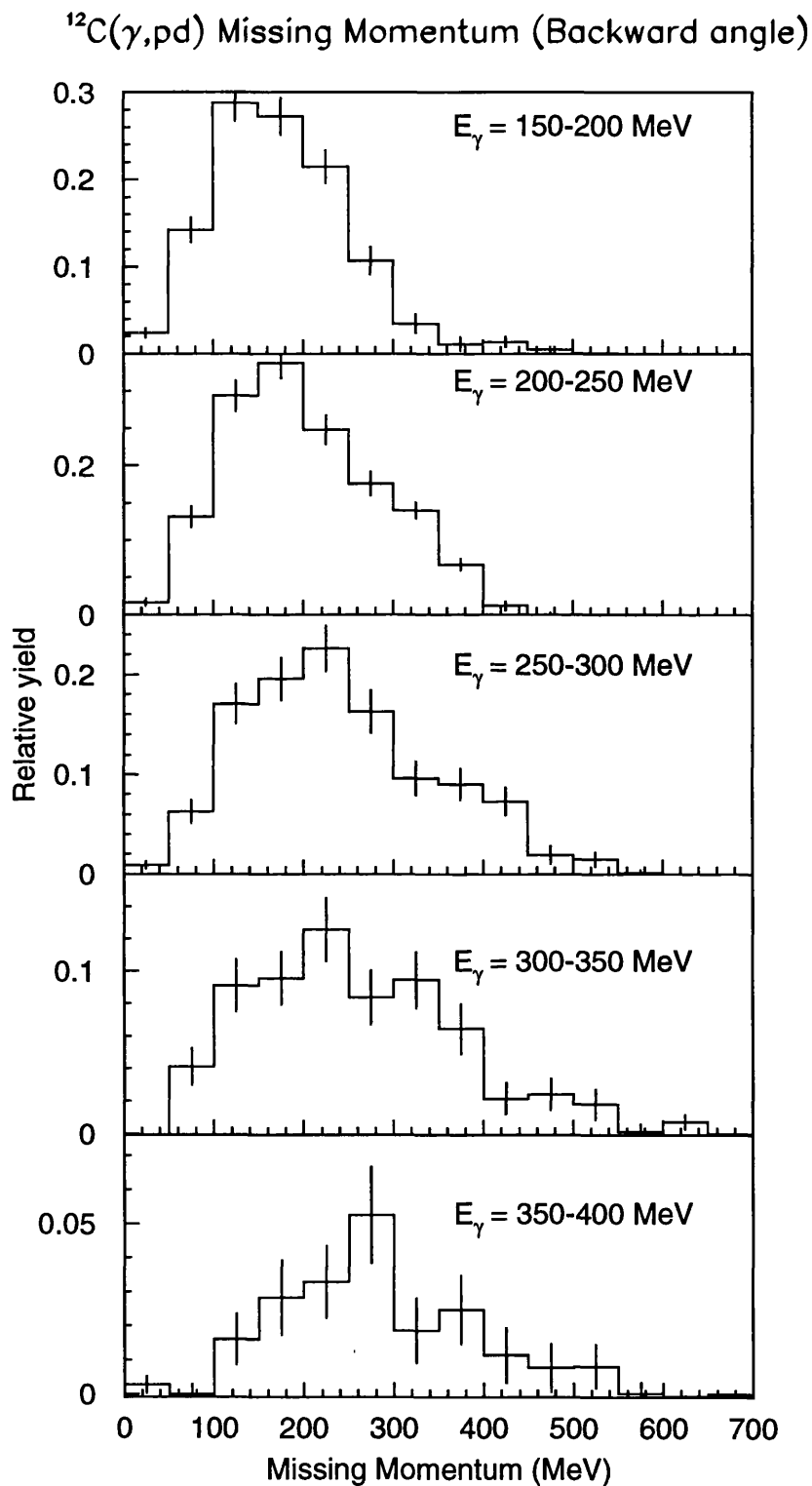


Figure 5.8: Recoil momentum distributions for the  $^{12}\text{C}(\gamma, \text{pd})$  reaction at the backward  $\text{PiP}$  angle detector geometry for low missing energy,  $E_m < 44$  MeV. Sample error bars show the statistical errors.

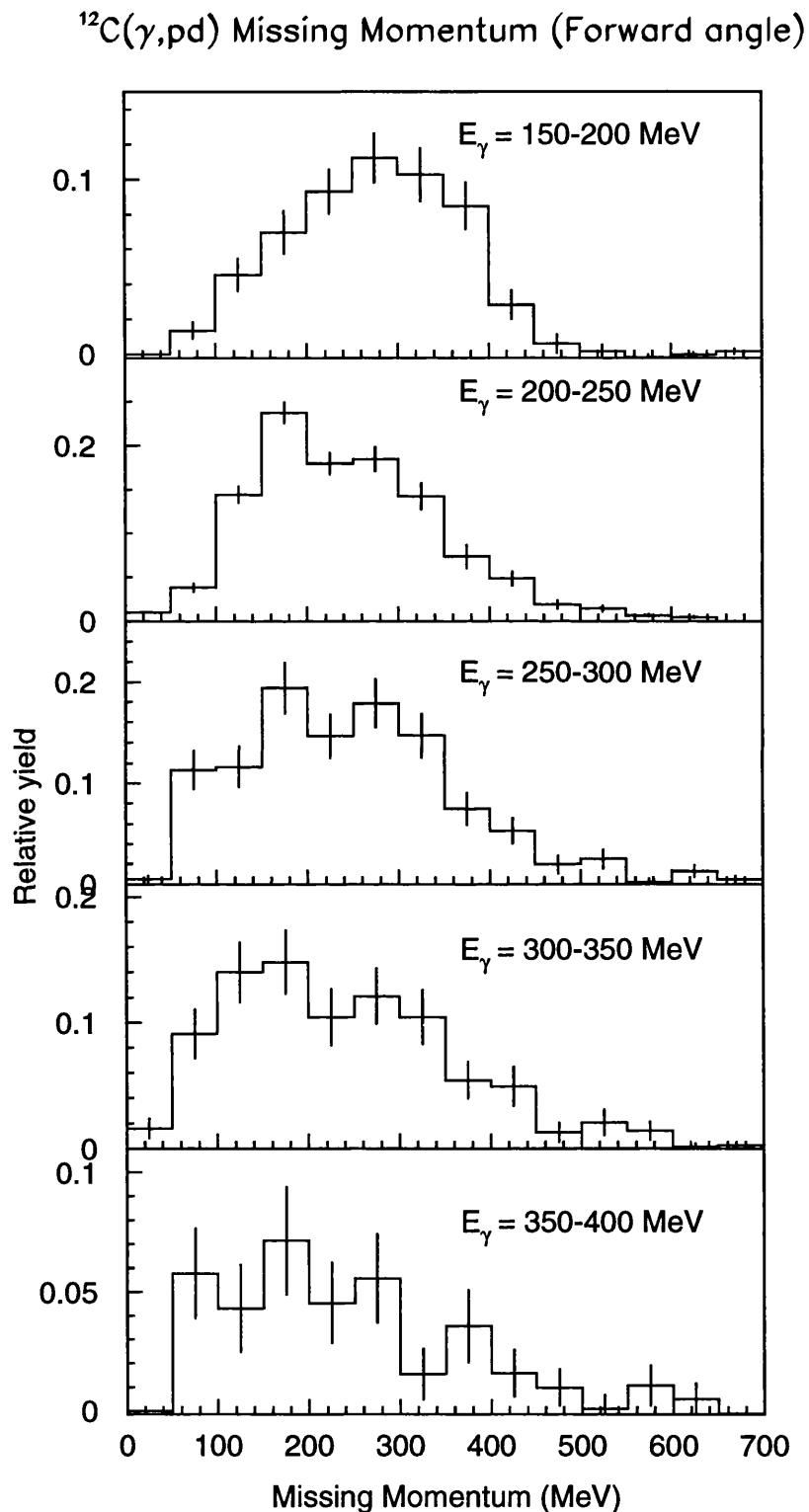


Figure 5.9: Recoil momentum distributions for the  $^{12}\text{C}(\gamma, \text{pd})$  reaction at the forward  $\text{PiP}$  angle detector geometry for low missing energy,  $E_m < 44$  MeV. Sample error bars show the statistical errors.

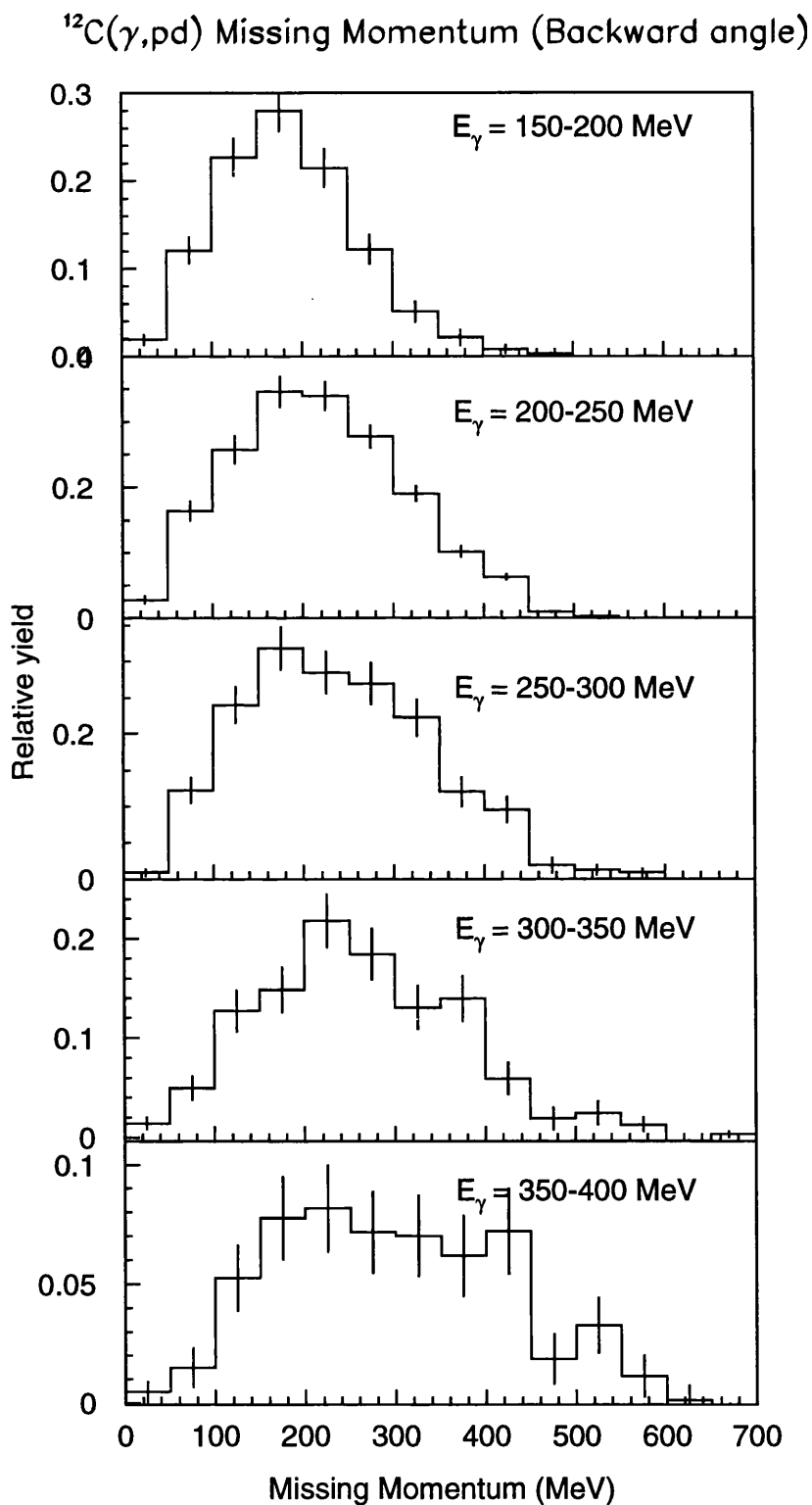


Figure 5.10: Recoil momentum distributions for the  $^{12}\text{C}(\gamma, pd)$  reaction at the backward  $PiP$  angle detector geometry for higher missing energy,  $44 \leq E_m \leq 70$  MeV. Sample error bars show the statistical errors.

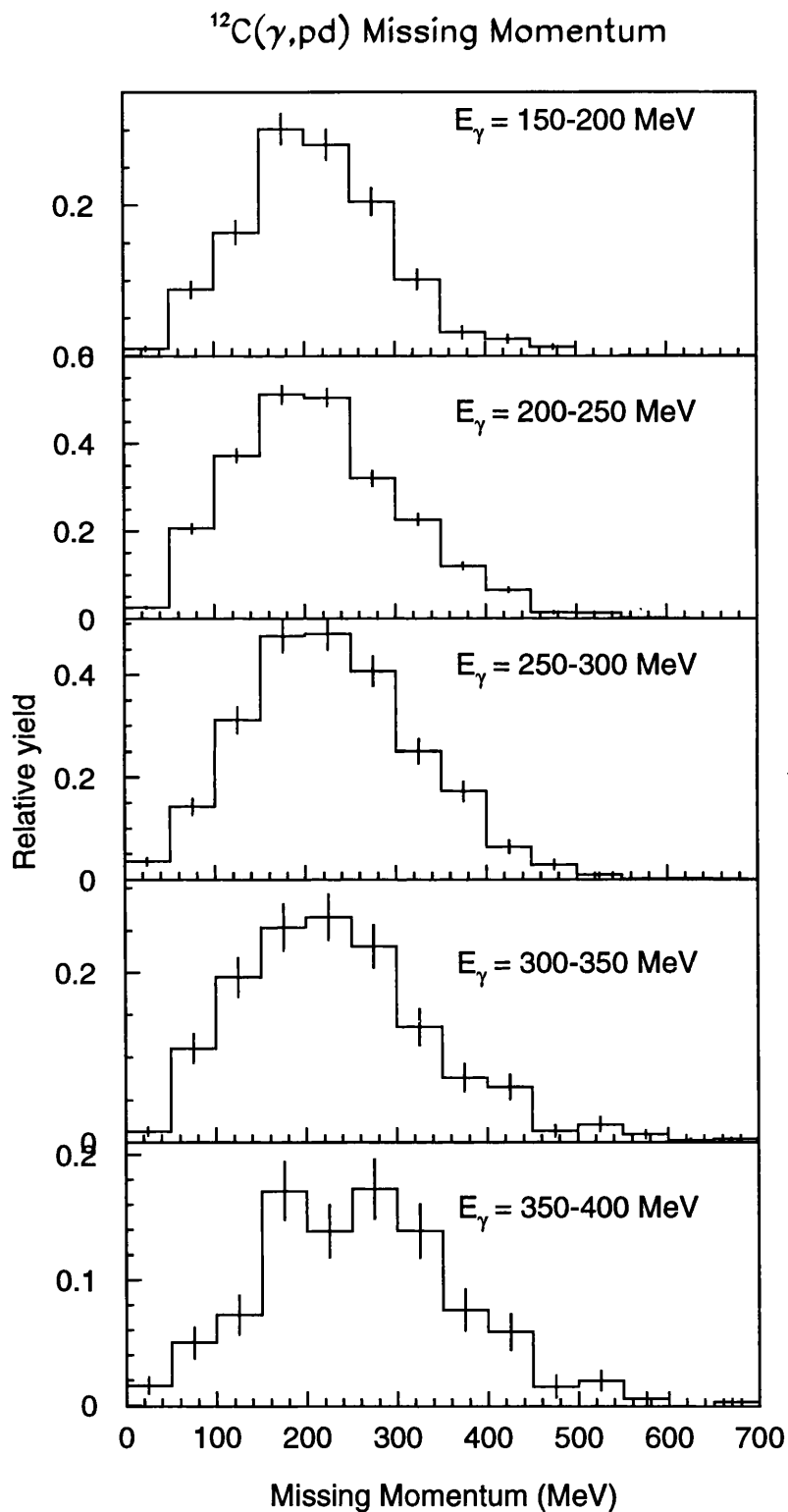


Figure 5.11: Recoil momentum distributions for the  $^{12}\text{C}(\gamma, pd)$  reaction at the central  $PiP$  angle detector geometry for higher missing energy,  $44 \leq E_m \leq 70$  MeV. Sample error bars show the statistical errors.

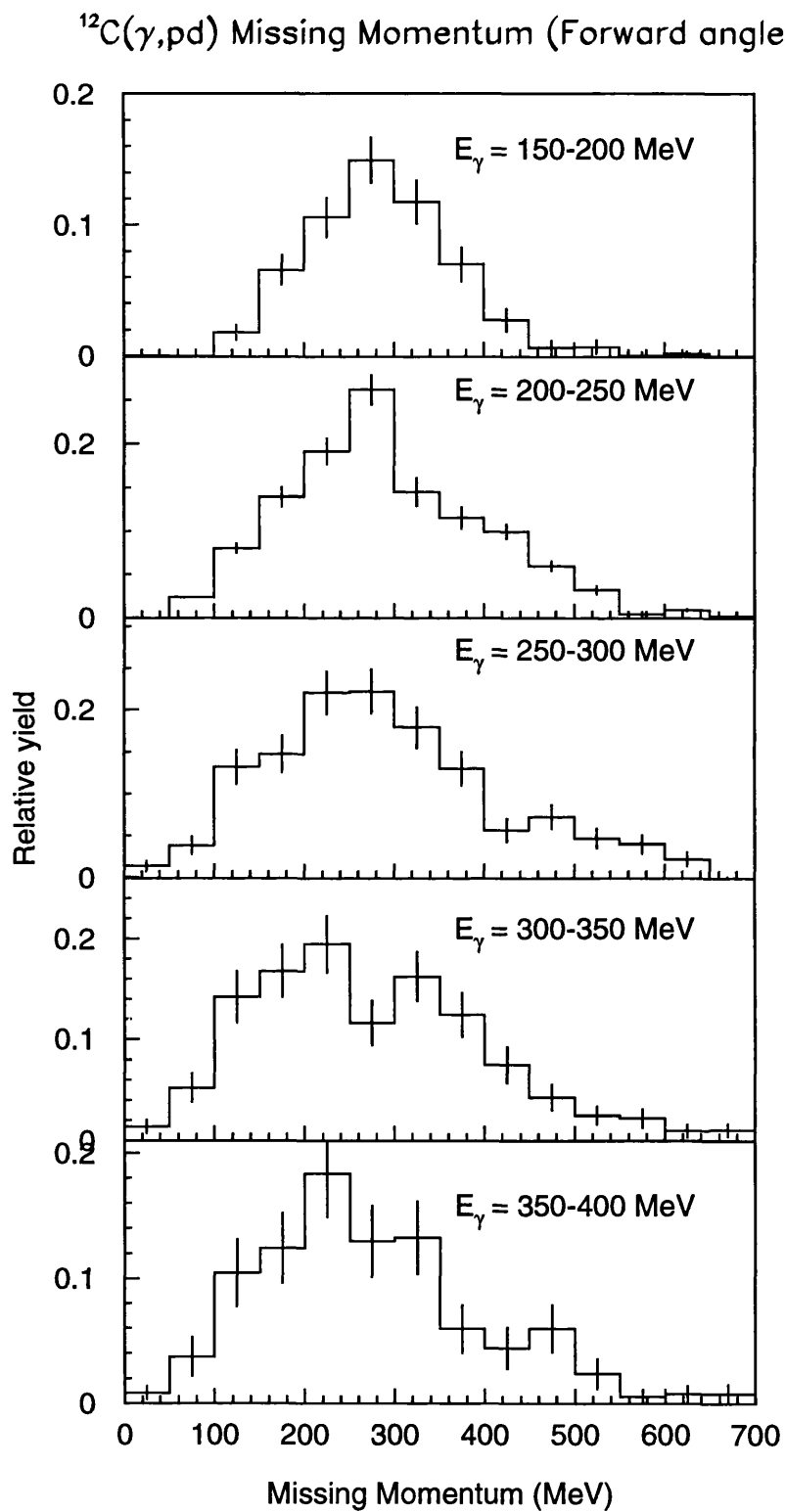


Figure 5.12: Recoil momentum distributions for the  $^{12}\text{C}(\gamma, \text{pd})$  reaction at the forward  $\text{PiP}$  angle detector geometry for higher missing energy,  $44 \leq E_m \leq 70$  MeV.

## 5.4 Photon Energy Dependence

Another indication of what the reaction mechanism may be is provided by an examination of the photon energy dependence of the reaction cross section cut on low missing energy. Selecting the low missing energy region, defined as missing energies below 44 MeV, will select those events which are most likely to be  $^3\text{He}$  like' and so a direct comparison can be made between the energy dependence of the cross section for these events and the energy dependence of the two-body breakup reaction  $^3\text{He}(\gamma, \text{pd})$  [5]. Figure 5.13 compares the photon energy dependence of each reaction cross section for various centre of momentum proton angles. The detector solid angles have been taken into account as explained in section 5.5.

While the energy dependencies are similar they are not identical. The effect of the detector thresholds has to be considered up to photon energies of about 225 MeV in the present work where they have the greatest influence at the most forward proton angles and lower photon energies. At photon energies greater than  $\sim 225$  MeV it can be seen that the energy dependence of the present work is very similar to that of the  $^3\text{He}$  two-body breakup reaction. Bearing in mind the possibility of significant medium modification effects, the dependencies are similar enough, in these higher photon energy regions, to suggest that the  $^{12}\text{C}(\gamma, \text{pd})$  reaction may indeed be a straightforward breakup of  $^3\text{He}$  clusters in the nucleus. It is observed that these excitation functions exhibit no structure in the Delta region around  $\sim 300$  MeV. This contrasts with deuteron photodisintegration where a prominent peak is clearly seen in this region. This point is discussed more fully in Chapter 1.

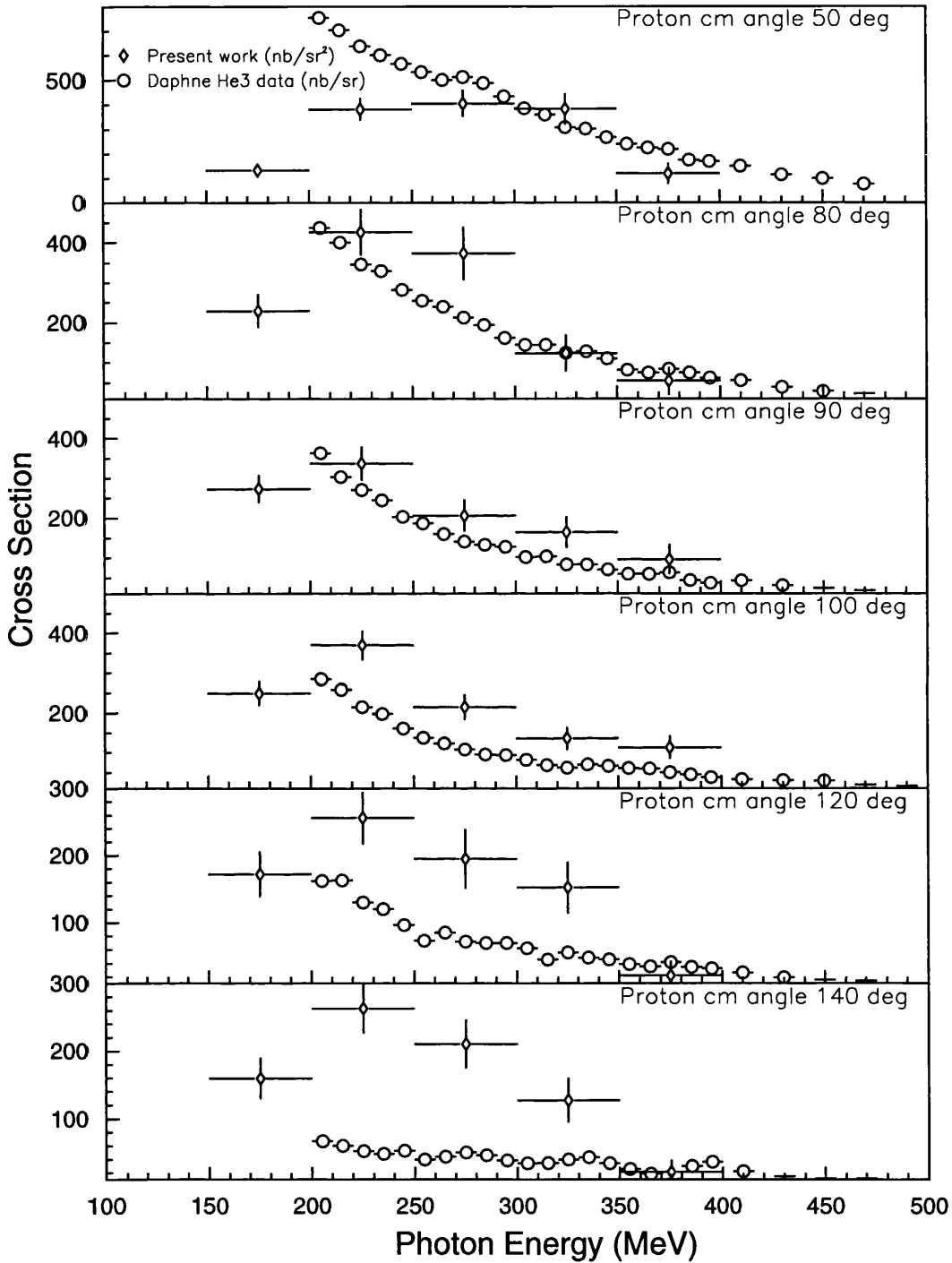
$^{12}\text{C}(\gamma, \text{pd})$  Photon Energy Dependence:  $E_m < 44\text{MeV}$ 

Figure 5.13: Photon energy dependence of the  $^{12}\text{C}(\gamma, \text{pd})$  reaction for low missing energy compared to that for the  $^3\text{He}(\gamma, \text{pd})$  reaction [5]. It should be noted that in the  $^3\text{He}$  measurement only the proton solid angle is taken into account and so the cross section is expressed in units of nb/sr.

## 5.5 Angular Distributions

It has already been shown from an examination of the missing energy distributions that the reaction cross section is changing in magnitude with proton angle. The lowest missing energy region retains most strength with increasing photon energy for the more forward angles, with the observed yield for this region falling as the proton angle moves more backward. Indeed, if the reaction mechanism is ‘ $^3\text{He}$  like’ then the expectation [5] is that the magnitude of the cross section will fall smoothly with increasingly backward proton angles as indicated on figures 1.4-1.6. It is therefore instructive to examine the angular distribution of the cross section for the  $^{12}\text{C}(\gamma, \text{pd})$  reaction and to compare it not only with the two-body  $^3\text{He}$  breakup channel but with the angular distributions observed for the  $^{12}\text{C}(\gamma, \text{pn})$  and  $(\gamma, \text{pp})$  reactions, which have been shown to exhibit marked differences in their angular distributions [51].

For the purpose of measuring the angular distribution each front TOF stand is split into two angular bins, giving a total of 6 angular TOF bins for each detector geometry, 18 bins in all. The deuteron angle of each TOF bin is defined by the centre of each group of 4 TOF bars at beam height. For each deuteron angle  $\theta_d$  an associated proton angle  $\theta_p$  is calculated from two-body breakup kinematics, defining each PiP angular bin as  $\theta_p \pm 10^\circ$ . In order to determine the cross section the deuteron solid angle  $\Delta\Omega_d$  and corresponding proton solid angle  $\Delta\Omega_p$  are taken into account. The angular distributions are measured over photon energies from  $175 \pm 25$  MeV to  $375 \pm 25$  MeV and for two missing energy regions from  $E_m < 44$  MeV for particle emission from the  $1p1p1p$  shell and from 44-70 MeV for particle emission from the  $1p1p1s$  shell. A list of the deuteron and proton angles with the appropriate solid angle correction and resulting cross section are given for each photon energy and missing energy region in Appendix B. Figures 5.14 and

5.15 show the angular cross section distribution for the reaction for low and then higher missing energy regions as a function of the TOF-side laboratory angles.

An interesting comparison to make is to examine the angular distributions for the  $^{12}\text{C}(\gamma, \text{pn})$  and  $(\gamma, \text{pp})$  reactions. Figures 5.16 to 5.19 are the angular distributions for these reactions analysed in a similar way [51]. The angular distributions for the pn and pp reactions are different in both missing energy regions and distinctly so in the lower missing energy region. In the pn case for the  $E_m < 44$  MeV region, all the angular distributions exhibit a broad peak at  $\sim 80^\circ$  whereas a sharper peak is observed for the 40-70 MeV missing energy region. For the  $(\gamma, \text{pp})$  reaction in the  $E_m < 44$  MeV region, there is a 'dip' at central angles in nearly all the photon energy bins. This 'dip' is most obvious at  $E_\gamma = 275 \pm 25$  MeV and is in complete contrast to the  $(\gamma, \text{pn})$  case. At higher missing energies the  $(\gamma, \text{pp})$  spectra are more similar in shape to the  $(\gamma, \text{pn})$  spectra, showing a broad bump with a maximum around  $\theta_p^{TOF} = 60^\circ - 80^\circ$ , although there is still an indication of a minimum at  $\theta_p^{TOF} = 110^\circ - 130^\circ$  for  $E_\gamma$  above 225 MeV. It is noted that the  $(\gamma, \text{pp})$  cross section is about a factor 10 smaller than the cross section for  $(\gamma, \text{pn})$ .

In comparison the pd channel has more in common with the pn channel, for the lowest missing energy region with broad peaked structures especially at the lower photon energies. It should be stressed that detector thresholds will have an effect on these distributions up to about 225 MeV in this missing energy region (in the direct model a photon needs roughly 35 MeV (average separation energy) + 50 MeV (deuteron threshold) in which case the proton has  $\sim 100$  MeV = 185 MeV). As the photon energy increases the cross section rises as the deuteron angle moves more backward, corresponding to more forward proton angles, in broad agreement with the  $^3\text{He}$  two-body break-up channel. The distributions show no evidence of the prominent 'dips' observed for the pp channel.

For the higher missing energy region, where detector threshold effects are more

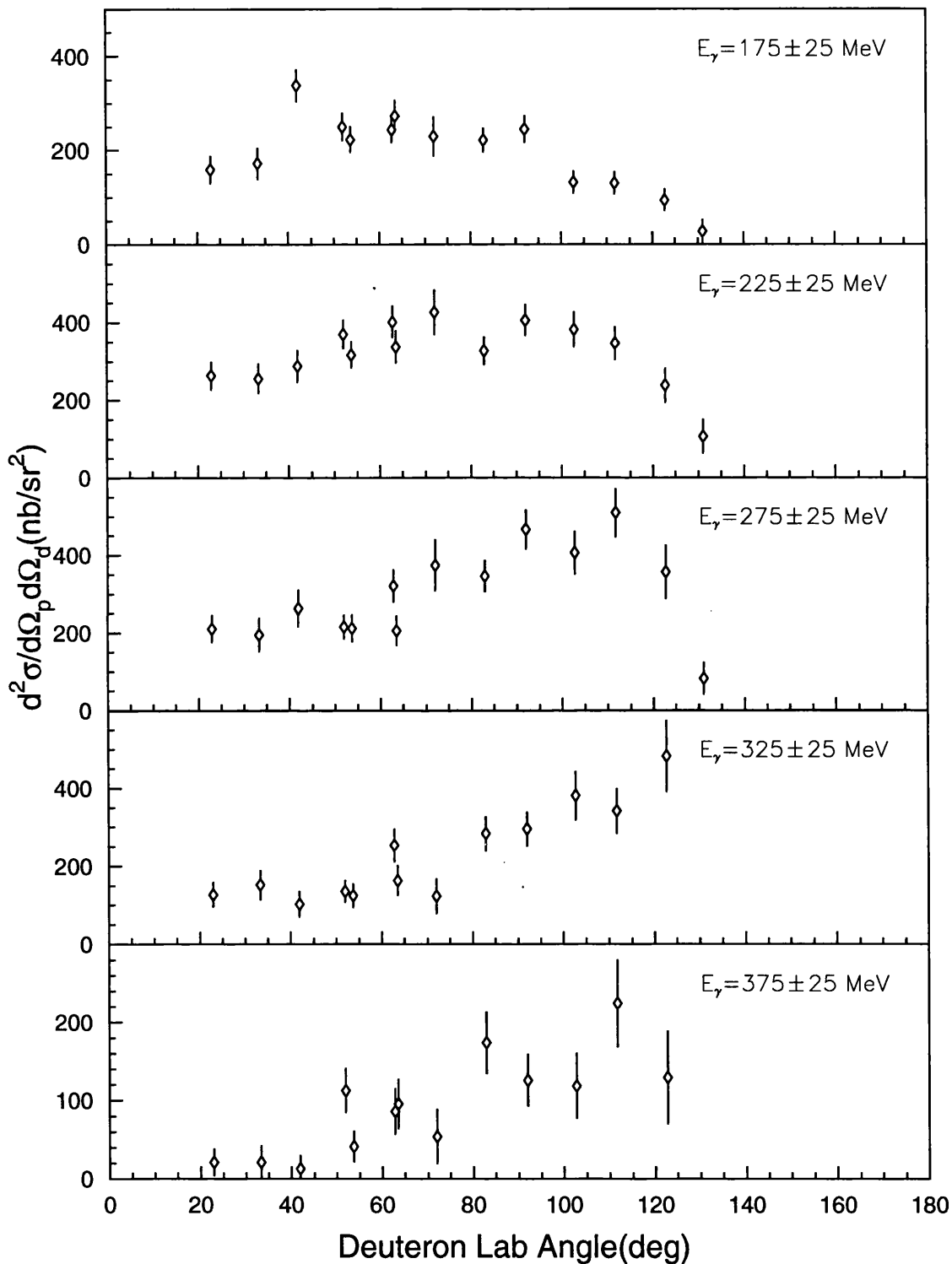
$^{12}\text{C}(\gamma, \text{pd})$  Angular Distribution:  $E_m < 44\text{MeV}$ 

Figure 5.14: Angular distribution of  $^{12}\text{C}(\gamma, \text{pd})$  cross section for missing energy  $E_m < 44$  MeV, for various photon energies.

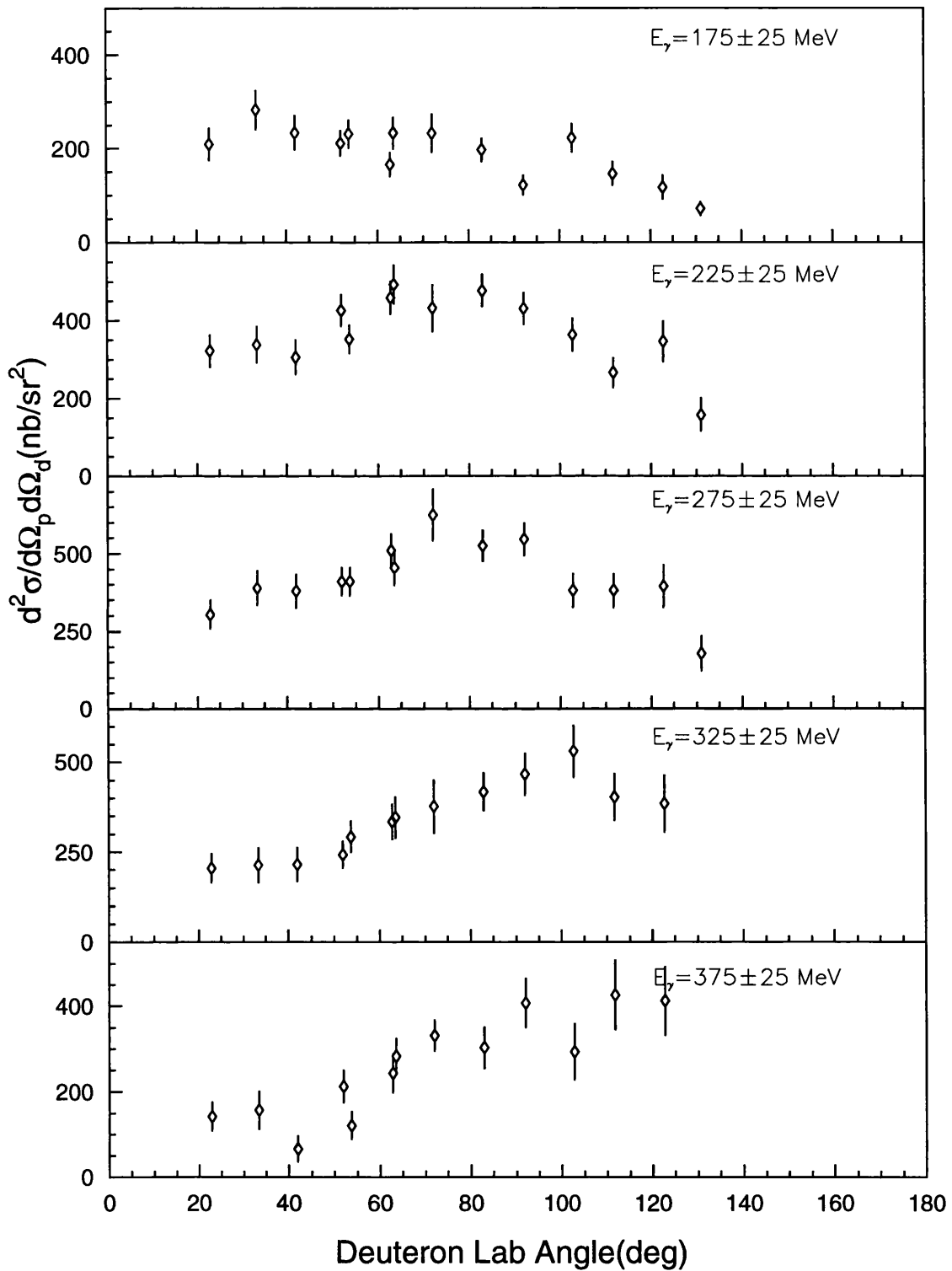
$^{12}\text{C}(\gamma, pd)$  Angular Distribution:  $E_m=44-70\text{MeV}$ 

Figure 5.15: Angular distribution of  $^{12}\text{C}(\gamma, pd)$  cross section for missing energy 44-70 MeV, for various photon energies.

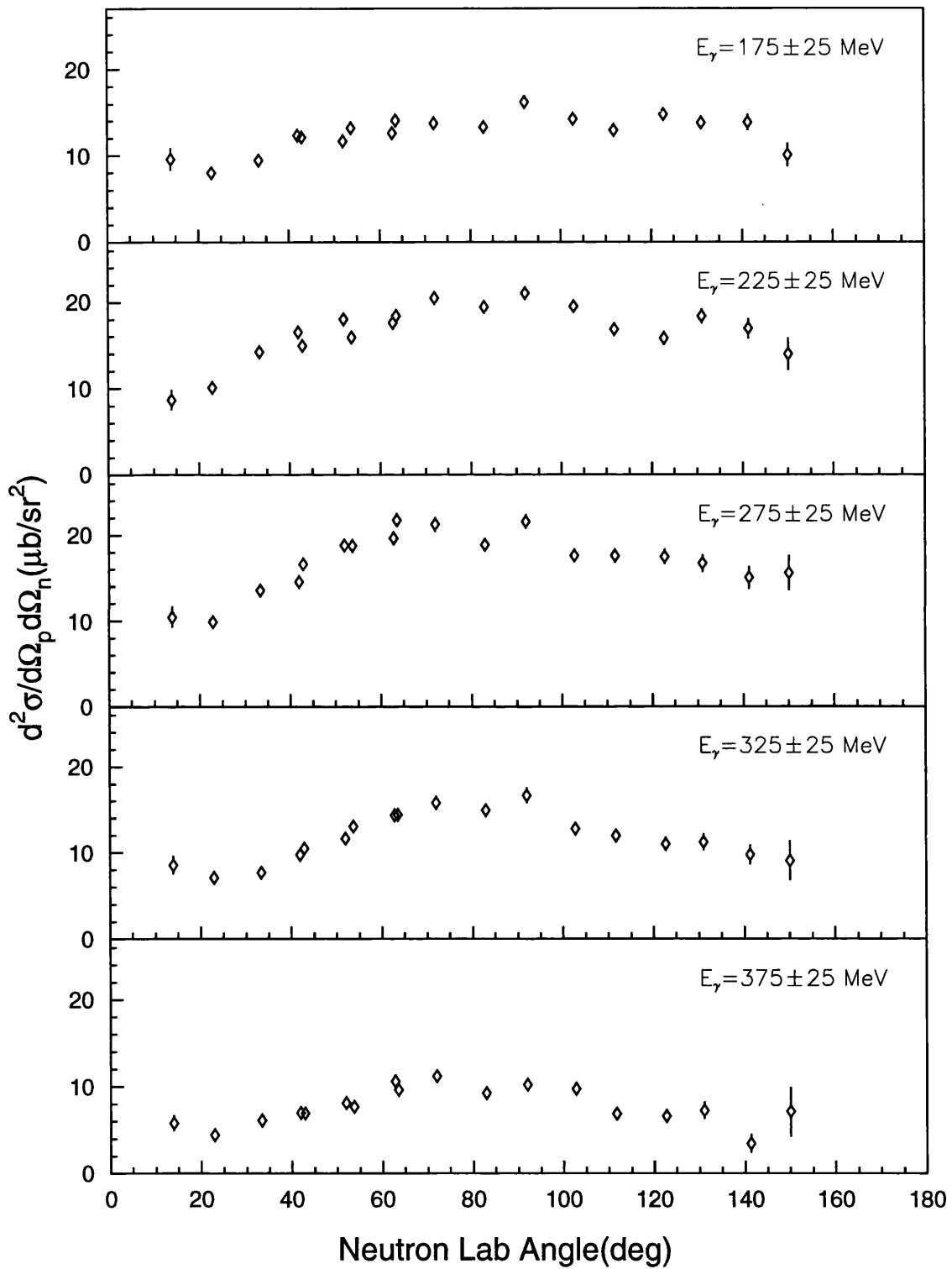
$^{12}\text{C}(\gamma, pn)$  Angular Distribution:  $E_m < 40\text{MeV}$ 

Figure 5.16: Angular distribution of  $^{12}\text{C}(\gamma, pn)$  cross section for missing energy  $E_m < 40\text{ MeV}$ , for various photon energies.

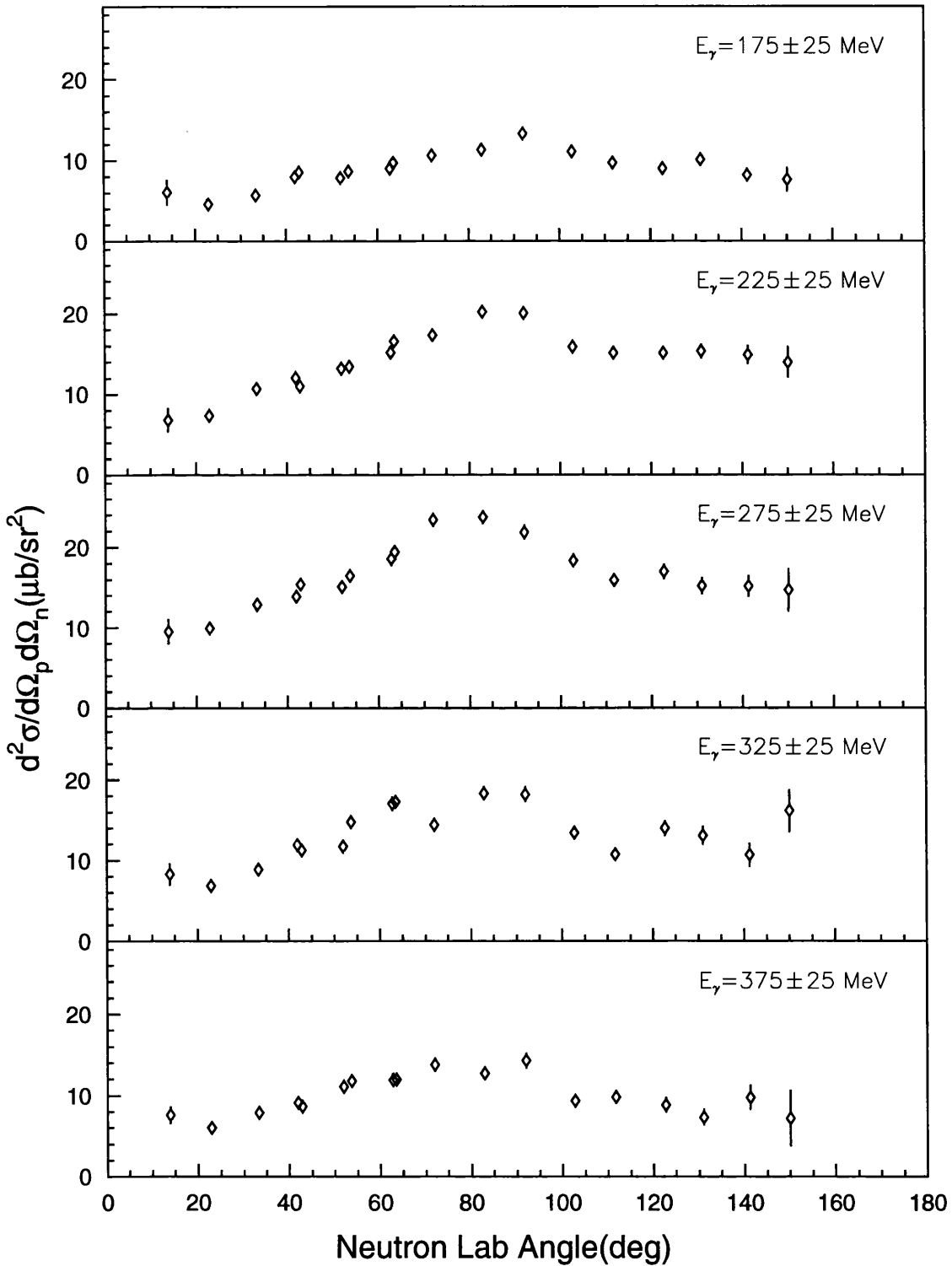
$^{12}\text{C}(\gamma, pn)$  Angular Distribution:  $E_m=40-70\text{MeV}$ 

Figure 5.17: Angular distribution of  $^{12}\text{C}(\gamma, pn)$  cross section for missing energy 40-70MeV, for various photon energies.

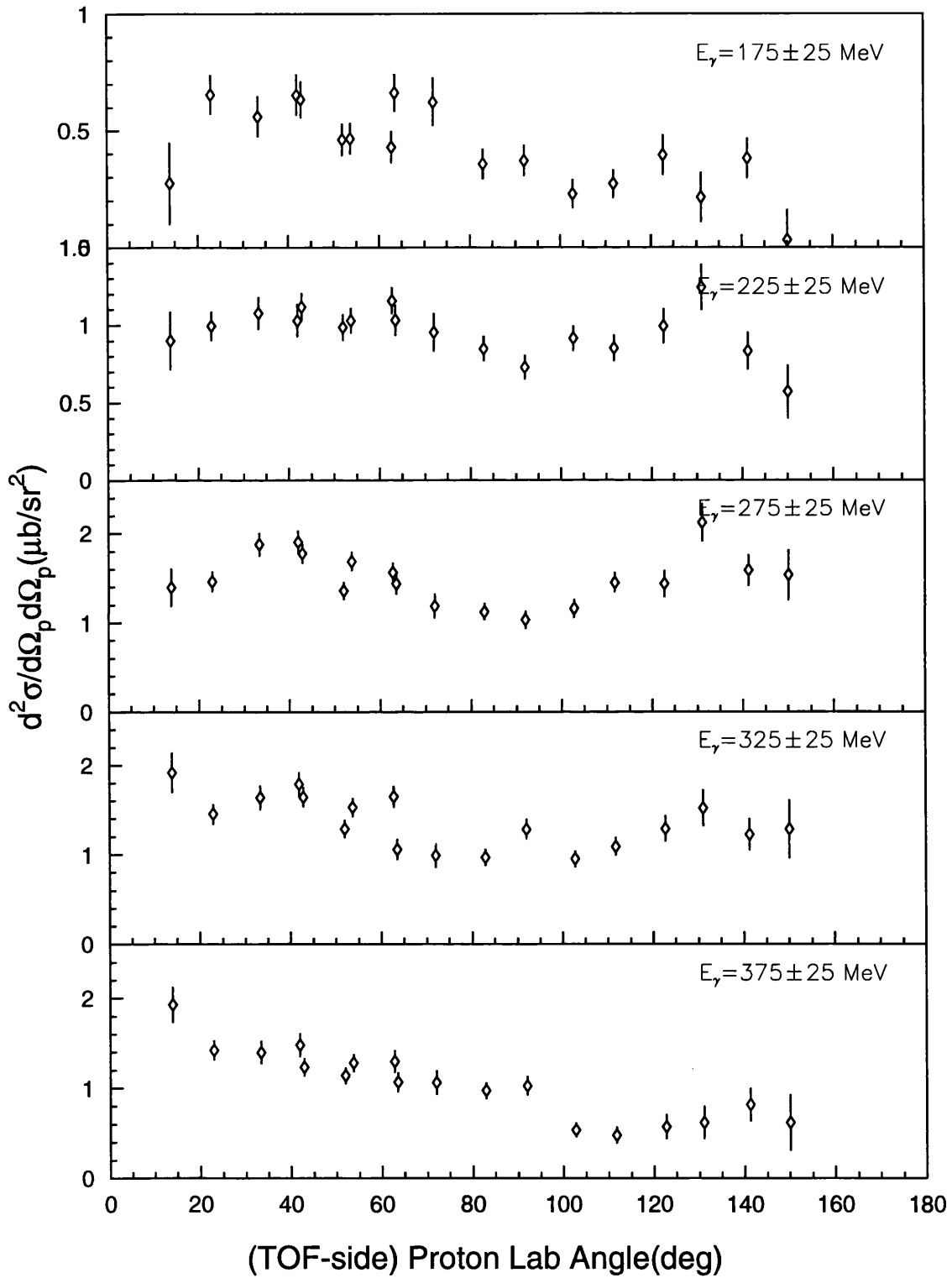
$^{12}\text{C}(\gamma, pp)$  Angular Distribution:  $E_m < 40\text{MeV}$ 

Figure 5.18: Angular distribution of  $^{12}\text{C}(\gamma, pp)$  cross section for missing energy  $E_m < 40$  MeV, for various photon energies.

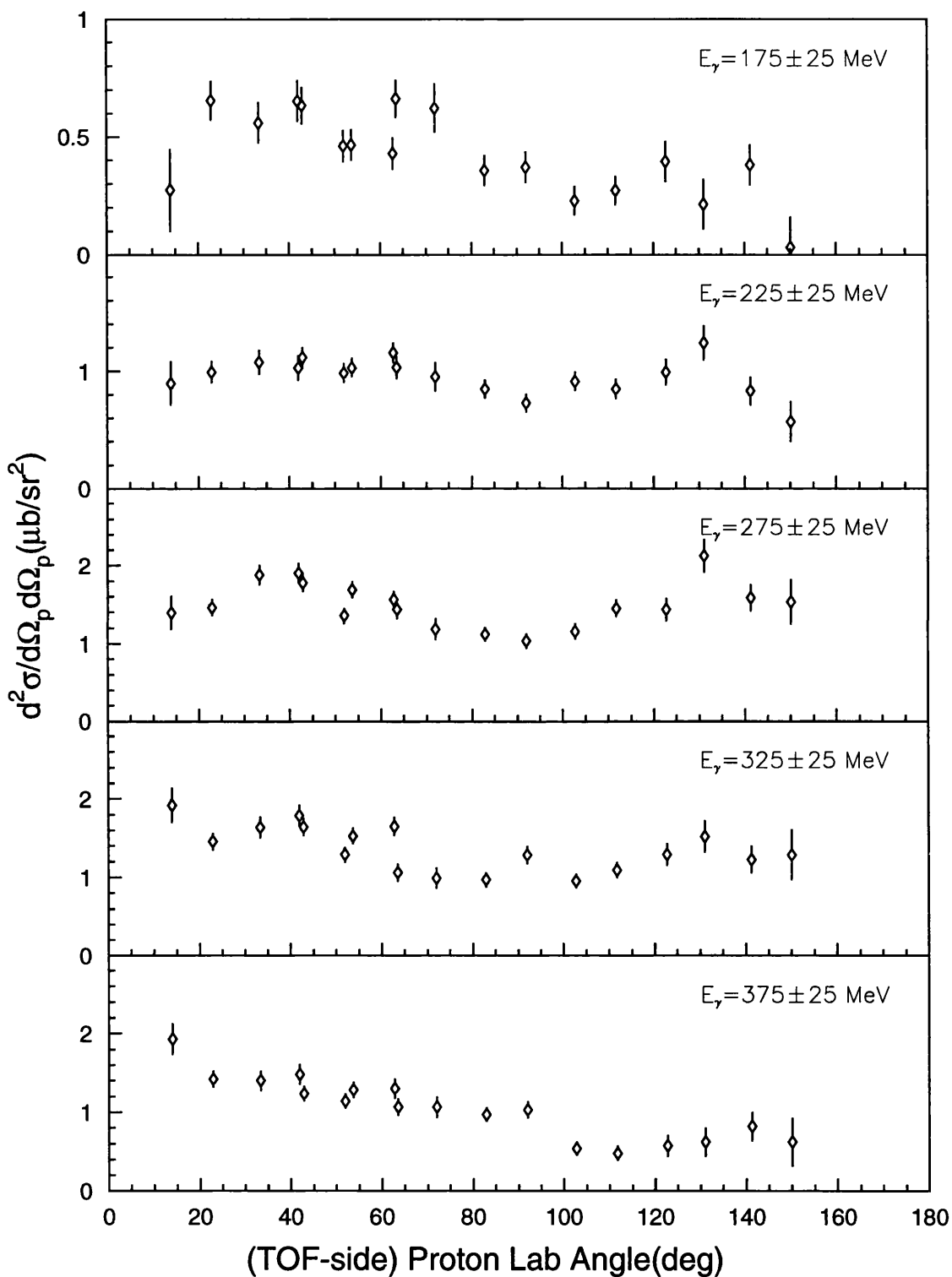
$^{12}\text{C}(\gamma,pp)$  Angular Distribution:  $E_m=40-70\text{MeV}$ 

Figure 5.19: Angular distribution of  $^{12}\text{C}(\gamma,pp)$  cross section for missing energy 40-70 MeV, for various photon energies.

important again due to the influence of a higher effective separation energy, there are broad, relatively flat structures up to the 275 MeV photon energy bin. For higher photon energies the magnitude of the cross section again starts to increase as the deuteron angle moves more backward. The quite prominent peaks observed for the higher missing energy region in the pn channel are not reflected in the pd channel.

It should be noted that the  $(\gamma, pd)$  cross section is a factor of  $\sim 3$  lower than that for  $(\gamma, pp)$  and is therefore about a factor of  $\sim 30$  lower than the cross section for  $(\gamma, pn)$ . If the reaction mechanism proceeds as a pickup then one in every 30 neutrons would be required to pick up the necessary proton to form the deuteron final state. This would appear to imply a rather large cross section for the pickup reaction and therefore makes it unlikely that the reaction mechanism is predominantly a pickup one.

As a further comparison, figure 5.20, the  $^{12}\text{C}(\gamma, pd)$  angular distributions are compared to those for the  $^3\text{He}$  two body breakup channel. This time the angular distributions are plotted as a function of the proton angle. It can be seen that the shapes are very similar for the higher photon energy regions where detector threshold effects are not important, consistent with a reaction mechanism which involves direct photon absorption by a  $3\text{N}$  cluster.

## Angular Distributions

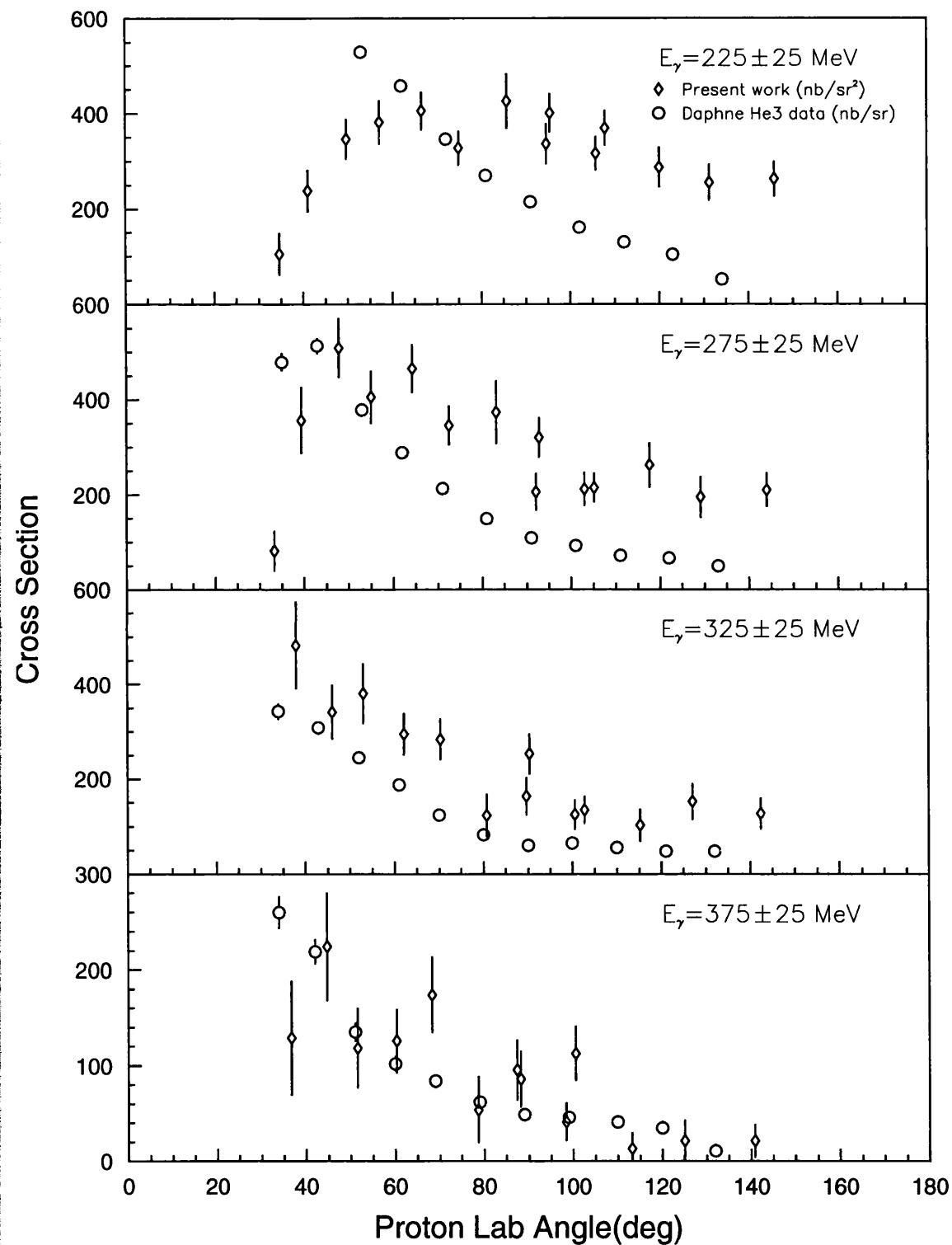


Figure 5.20: Angular distribution of the  $^{12}\text{C}(\gamma, pd)$  cross section for missing energy  $E_m < 44$  MeV, for various photon energies, compared to that for the  $^3\text{He}$  two body breakup channel [5].

## 5.6 Monte Carlo Simulations

### 5.6.1 Missing Energy Distributions

Monte Carlo simulations of the experiment based on two very different models of the  $^{12}\text{C}(\gamma, \text{pd})$  reaction will be compared with the experimental distributions. The direct model calculates the momenta of the proton and deuteron emitted from the target nucleus following direct photon absorption on a three nucleon cluster and assumes that the residual nucleus takes no part in the interaction. The pickup model assumes an initial  $^{12}\text{C}(\gamma, \text{pn})$  reaction followed by an  $n(\text{p}, \text{d})$  pickup reaction, with the magnitude and direction of the picked-up proton momentum constrained to be very similar to that of the outgoing neutron, creating an on-shell deuteron in the final state. The basis of the model is a direct two nucleon,  $(\gamma, \text{pn})$  reaction. The models are described more fully in section 4.10.

Comparisons between the experimentally observed missing energy distributions and those predicted by the models should provide an initial understanding of what the reaction mechanism may be. However, for the direct model, the input excitation distribution is chosen in such a way that the predicted missing energy distribution matches the experimentally observed missing energy distribution. In this case the model simulation of the excitation distribution has no predictive power. Information can however be gained from the missing energy distribution produced by the pickup model as the initial input to the simulation is the excitation distribution which produces the experimentally observed  $^{12}\text{C}(\gamma, \text{pn})$  missing energy distribution [51]. Figure 5.21 compares the experimentally observed  $^{12}\text{C}(\gamma, \text{pd})$  missing energy distribution with that predicted by the pickup model, for different photon energy regions. It can be seen that the predicted distributions show no evidence of the peaked structure observed in the experiment for low photon energies. However, for low photon energy, the shapes

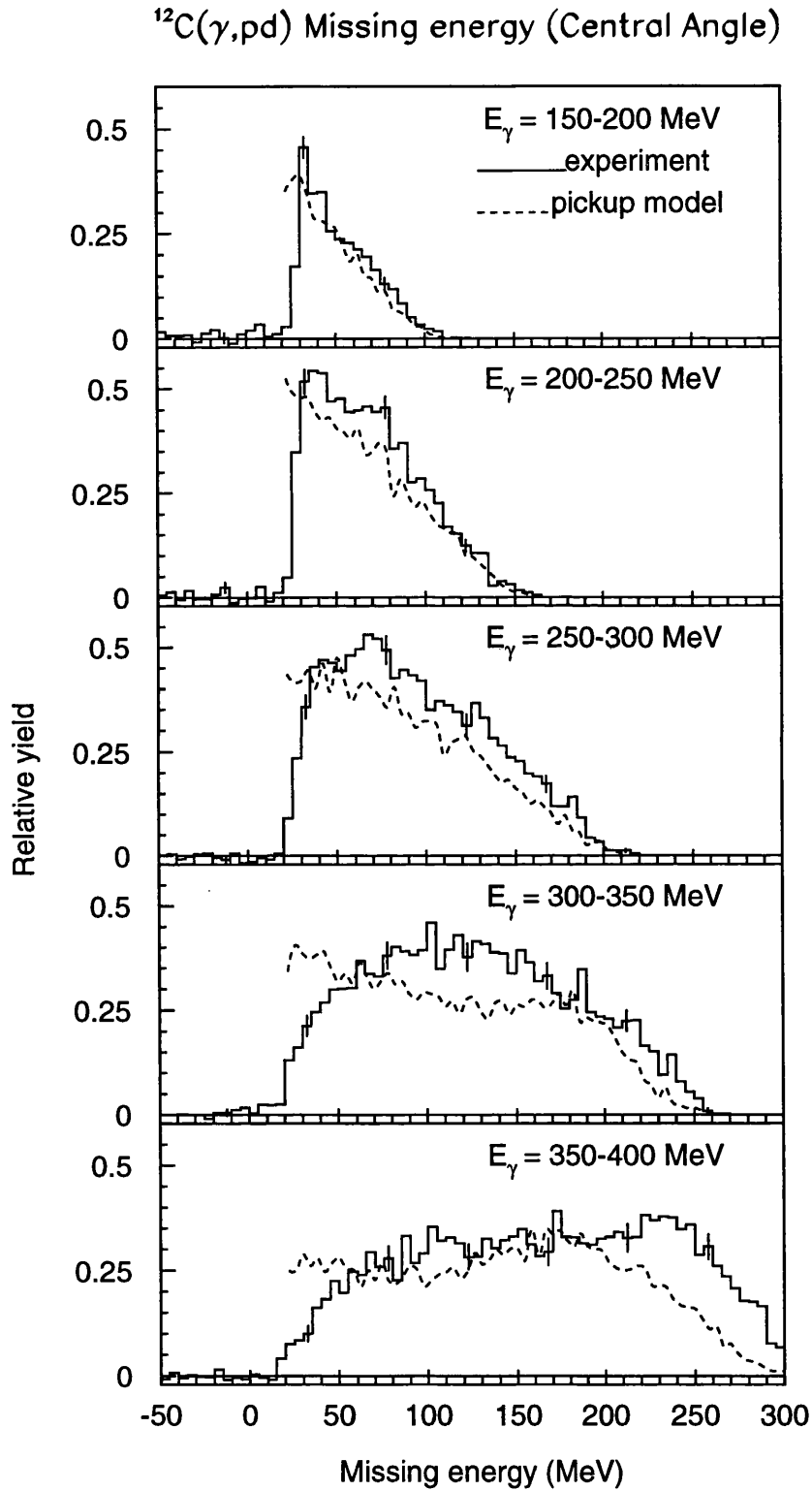


Figure 5.21: Missing energy distributions for the  $^{12}\text{C}(\gamma, \text{pd})$  reaction at central proton angles compared to the pickup model calculation.

of the distributions are similar enough at higher missing energies to suggest that there may indeed be a pickup component to the reaction mechanism, although clear differences are increasingly seen at high missing energies as the photon energy increases. To obtain further information on the possible mechanisms it is necessary to study further kinematic variables.

### 5.6.2 Recoil Momentum Distributions

Studying the momentum distribution of the recoiling system provides information on whether the recoil system was a spectator. In a direct absorption process, and in the absence of final state interactions, the recoil momentum reflects the initial momentum of the nucleons. An examination of figures A.1 and A.3 which show the  $F(p)$  distributions for a single p-shell particle and three correlated p-shell particles respectively, immediately shows that the average  $F(P)$  value, and so the momentum, for the 3N cluster is just  $\sqrt{3}$  times the average  $F(p)$  for the single p-shell particle. The  $P^2F(P)$  distribution for three correlated particles indicates that, in a direct reaction in which the residual system spectates, the expected average missing momentum will be  $\sim 250$  MeV/c. Much higher values for the missing momentum would indicate that other processes are playing a role. Figures 5.22 to 5.26 compare the model predictions with the experimental missing momentum distributions for each detector geometry and for photon energies in the range 150-400 MeV. The direct model is represented on the figures that follow by a solid curve and the pickup model is represented by a dashed curve. In order to ease comparison between the shapes of the distributions all model calculations are individually normalised to the data.

It is immediately evident that the pickup model does not describe the data in this low missing energy region for any photon energy except in the lowest photon energy region where the dominance of the detector threshold effects greatly

$E_\gamma = 150-200 \text{ MeV}$

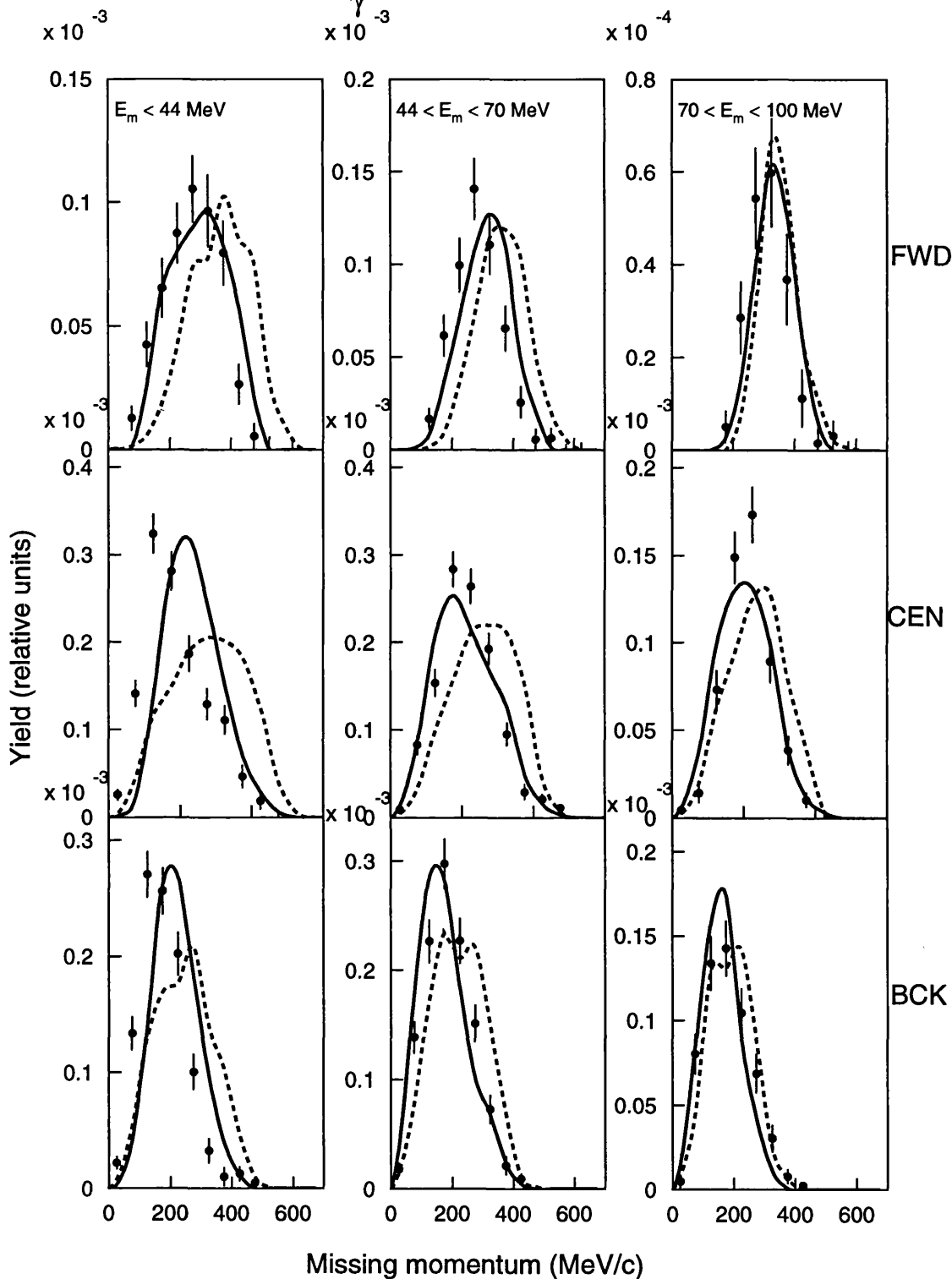


Figure 5.22:  $^{12}\text{C}(\gamma, pd)$  recoil momentum distributions, for different missing energy regions and all three detector geometries, for  $E_\gamma=150-200 \text{ MeV}$ . The solid curve represents the direct model; the dashed curve is the pickup model.

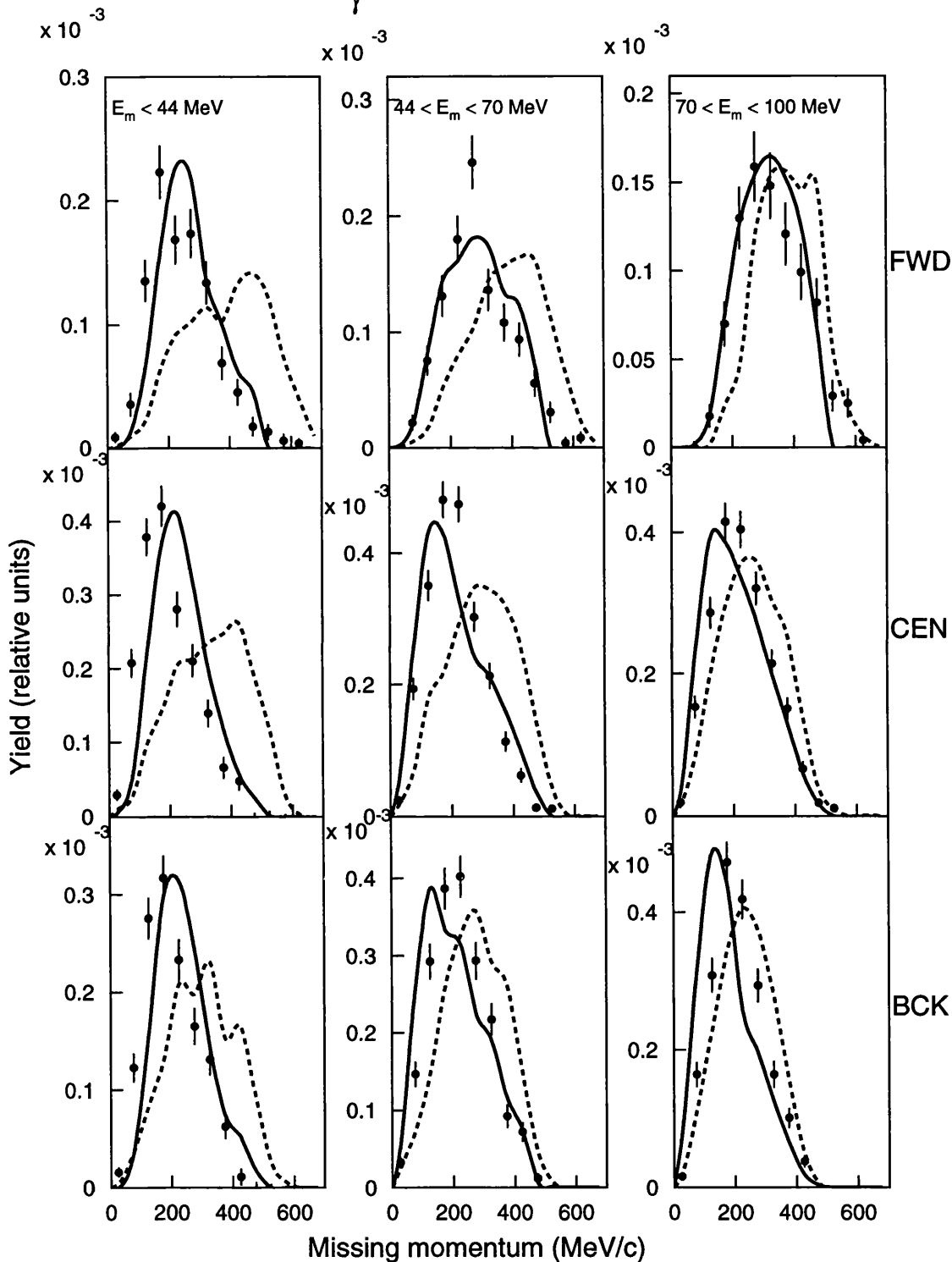
$E_\gamma = 200-250 \text{ MeV}$ 


Figure 5.23:  $^{12}\text{C}(\gamma, pd)$  recoil momentum distributions, for different missing energy regions and all three detector geometries, for  $E_\gamma=200-250 \text{ MeV}$ . The solid curve represents the direct model; the dashed curve is the pickup model.

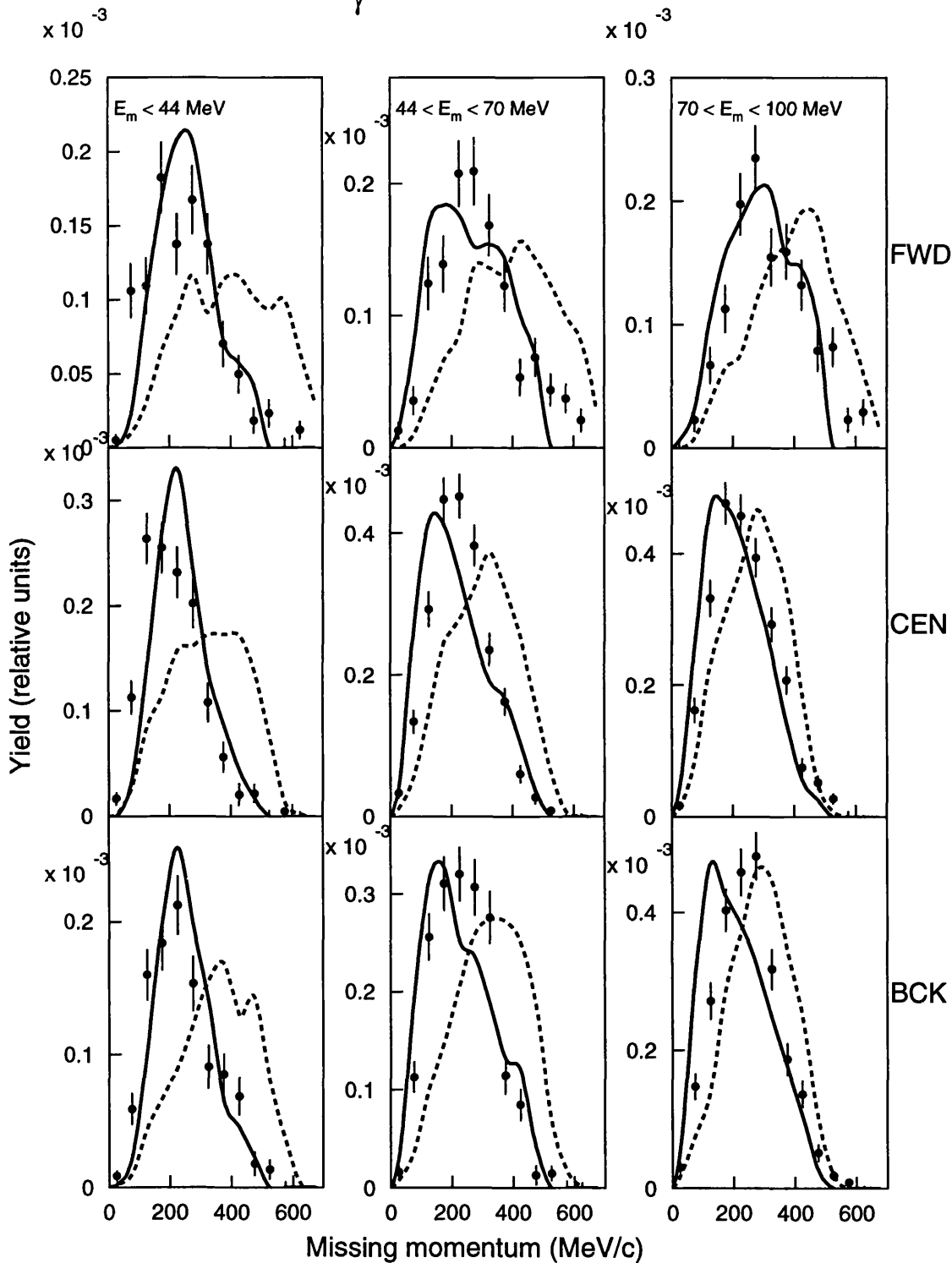
$E_\gamma = 250-300 \text{ MeV}$ 


Figure 5.24:  $^{12}\text{C}(\gamma, pd)$  recoil momentum distributions, for different missing energy regions and all three detector geometries, for  $E_\gamma=250-300 \text{ MeV}$ . The solid curve represents the direct model; the dashed curve is the pickup model.

$E_\gamma = 300-350 \text{ MeV}$

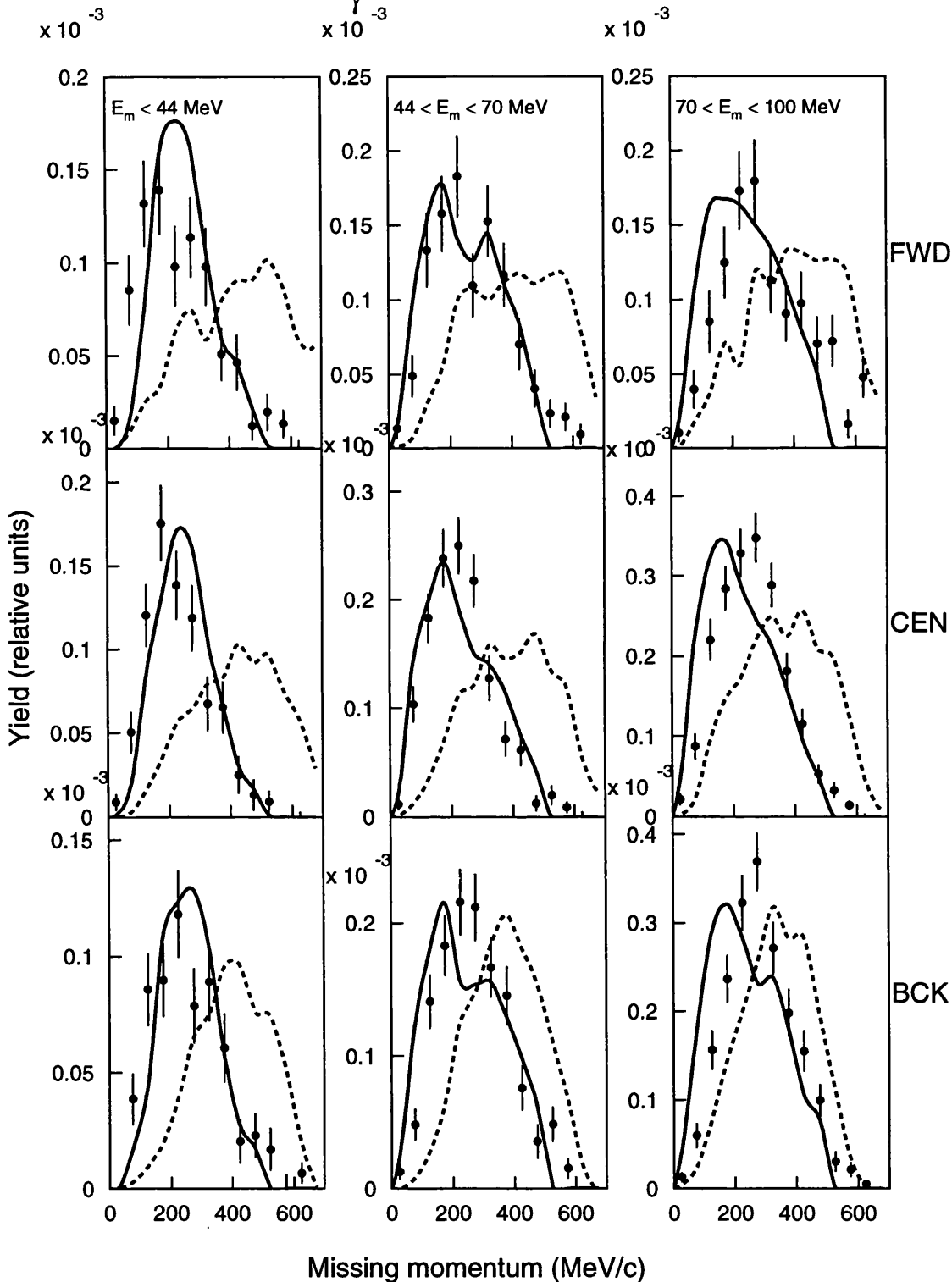


Figure 5.25:  $^{12}\text{C}(\gamma, pd)$  recoil momentum distributions, for different missing energy regions and all three detector geometries, for  $E_\gamma=300-350 \text{ MeV}$ . The solid curve represents the direct model; the dashed curve is the pickup model.

$$E_\gamma = 350-400 \text{ MeV}$$

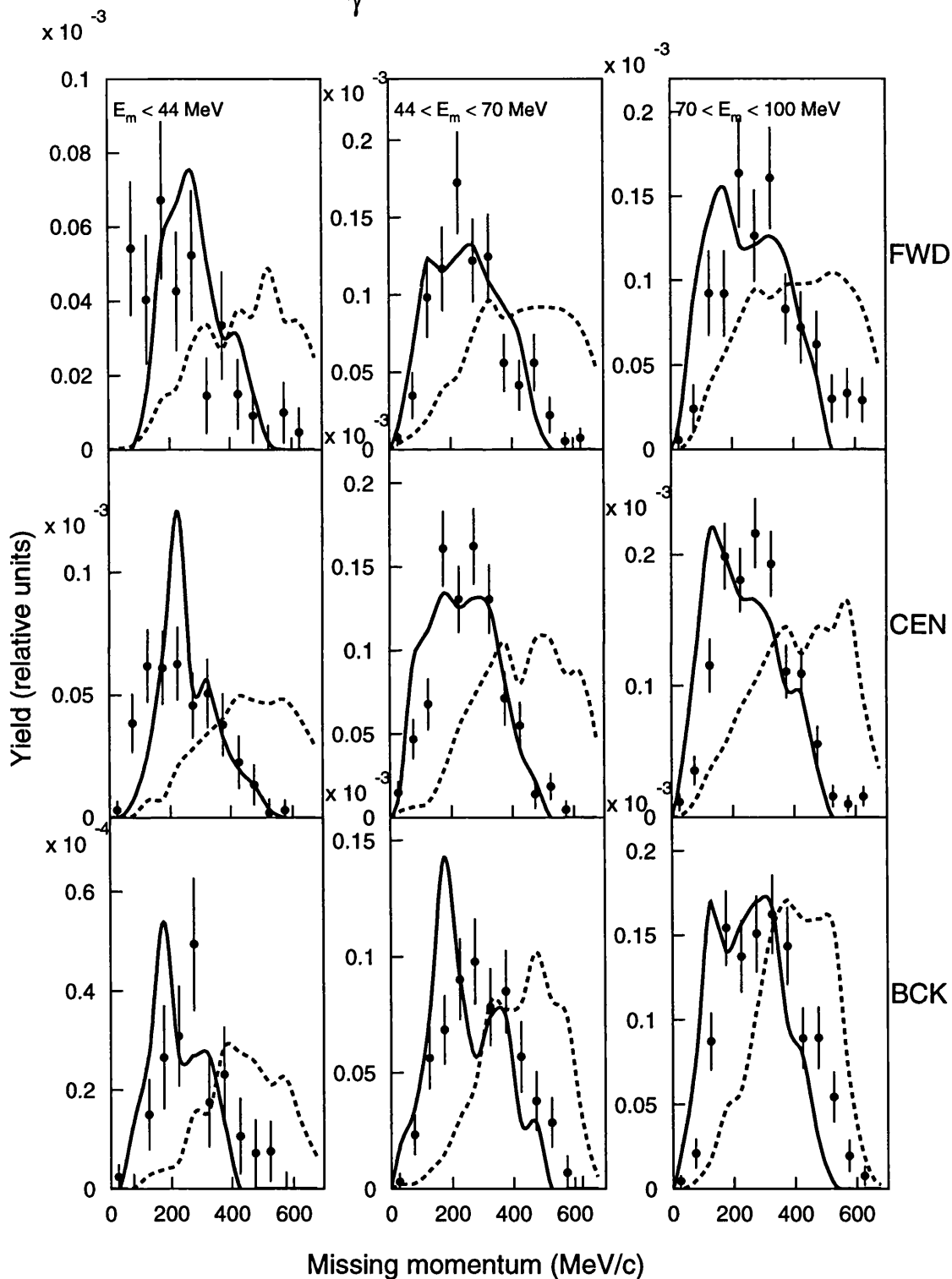


Figure 5.26:  $^{12}\text{C}(\gamma, pd)$  recoil momentum distributions, for different missing energy regions and all three detector geometries, for  $E_\gamma=350-400$  MeV. The solid curve represents the direct model; the dashed curve is the pickup model.

reduces the sensitivity to the reaction mechanism. This effect can be seen most clearly on figure 5.22 for the forward PiP angle data in the highest missing energy region where both models are very close to the data.

It is also clear from these plots that, for the lowest missing energy region,  $E_m < 44$  MeV, the observed momenta are smaller than predicted by both models. Since the direct model is the most straightforward way of obtaining low recoil momentum it is surprising that the experimental data exhibits even lower values. A similar effect was observed for the  $^{12}\text{C}(\gamma,pp)$  reaction by Harty *et al.* [22].

Overall however, for  $E_m < 44$  MeV, and for all photon energies, the direct model describes the experimental missing momentum distributions very well. Interestingly, the backward angle seems to be getting closer to the data as we go up in photon energy and at 250-300 MeV and 300-350 MeV it can be seen that the direct model is very close to the data. It has been noted from the discussion in Chapter 1 that as the photon energy increases towards  $\sim 500$  MeV and at more backward angles, 3N mechanisms play an increasingly important role in  $^3\text{He}$  photodisintegration.

Moving to the middle missing energy region,  $44 \leq E_m \leq 70$  MeV, it can be seen that, with the exception of the forward PiP angle at the lowest photon energy, the experimental distributions lie between those predicted by the simulations. It is also noted that as the photon energy increases up to 400 MeV the direct model calculation remains close to the data while the pickup model gets steadily worse. In this missing energy region where it is expected that particles may be removed from the s-shell, effectively increasing the separation energy, the detector threshold effects will play a role to higher photon energies than is the case in the lowest missing energy region. For this reason, for the two lowest photon energy bins, there is a reduced sensitivity to the reaction mechanism and the detector thresholds and acceptances constrain the data close to the model calculations.

The apparently good fits to the data for missing energies  $70 \leq E_m \leq 100$  MeV result from the significant effect of detector thresholds for this missing energy region. The models do not begin to exhibit much sensitivity to the reaction mechanism until photon energies greater than 300 MeV where again it can be seen that, especially in the 350-400 MeV region, the direct model calculation provides a significantly better description of the experimental data.

### 5.6.3 Momentum Difference

Another variable which may be particularly sensitive to the reaction mechanism is the momentum difference defined as

$$P_{diff} = |P_{proton}| - |P_{deuteron}| \quad (5.4)$$

If the reaction mechanism proceeds as the recoil system spectates leading to the back-to-back emission of a proton and deuteron, then in the centre of momentum frame of the photon and the stationary  ${}^3\text{He}$  cluster, the value of  $P_{diff}$  is zero as the photon momentum is shared equally between the absorbing particles. In the laboratory frame there is a spreading about zero due to the influence of the photon energy and from the initial cluster momentum. Figures 5.27-5.31 display the momentum difference distributions observed and predicted by the models for each detector setup for photon energies between 150 and 400 MeV in the laboratory frame. The effect of the detector geometry and thresholds is pronounced especially at the lowest photon energies as the distributions predicted by the direct model are clearly not averaging at zero. Viewing the same distributions without imposing the detector acceptances shows the anticipated average zero value for the momentum difference. See figure 5.32. The mostly negative values for  $P_{diff}$  in figures 5.26-5.30 reflect the fact that for equivalent kinetic energies a deuteron will carry  $\sim \sqrt{2}$  times the momentum of a proton. The TOF detectors  $\sim 50$  MeV deuteron energy threshold would require a proton energy of at least 100 MeV in order to balance the momenta and result in a  $P_{diff}$  of zero. Taking into account that the photon must also supply the  $\sim 32$  MeV separation energy, zero momentum difference requires a photon energy of at least  $\sim 180$  MeV. This explains why the momentum difference spectra are most asymmetric for the lowest photon energy bin. The distributions become less asymmetric as the photon energy increases and the detector threshold effects become less important.

The momentum difference plots follow a similar pattern to that of the missing momentum distributions with the direct model simulation describing the data significantly better than the pickup calculation. Figures 5.28 and 5.29 also provide evidence that, for the lowest missing energy region, as the photon energy increases, the backward PiP angle data is getting closer to the direct model than the data from the more forward PiP geometries.

## 5.7 Summary

This chapter has presented the results of the analysis of the  $^{12}\text{C}(\gamma, \text{pd})$  reaction measured over photon energies from 150-400 MeV. The experimental data points to a reaction mechanism which is very similar to that of  $^3\text{He}(\gamma, \text{pd})$  at low missing energy. The model calculations show that the mechanism is not a simple  $(\gamma, \text{pn})$  reaction followed by a pickup process.

The following chapter will discuss these conclusions in more detail and outline some possible future developments.

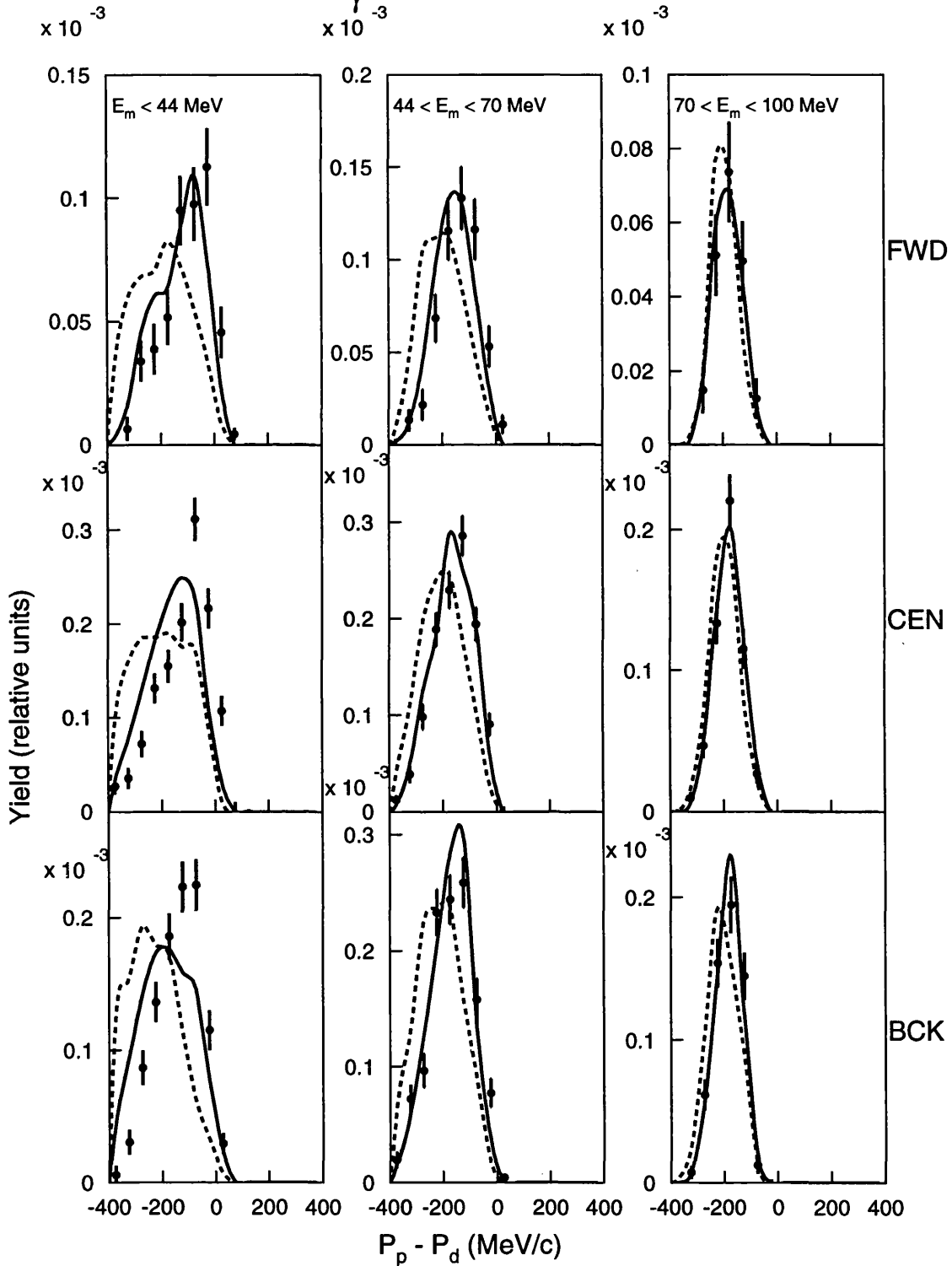
$E_\gamma = 150-200 \text{ MeV}$ 

Figure 5.27:  $^{12}\text{C}(\gamma, pd)$  momentum difference distributions, for different missing energy regions and all three detector geometries, for  $E_\gamma = 150-200 \text{ MeV}$ . The solid curve represents the direct model; the dashed curve is the pickup model.

$$E_\gamma = 200-250 \text{ MeV}$$

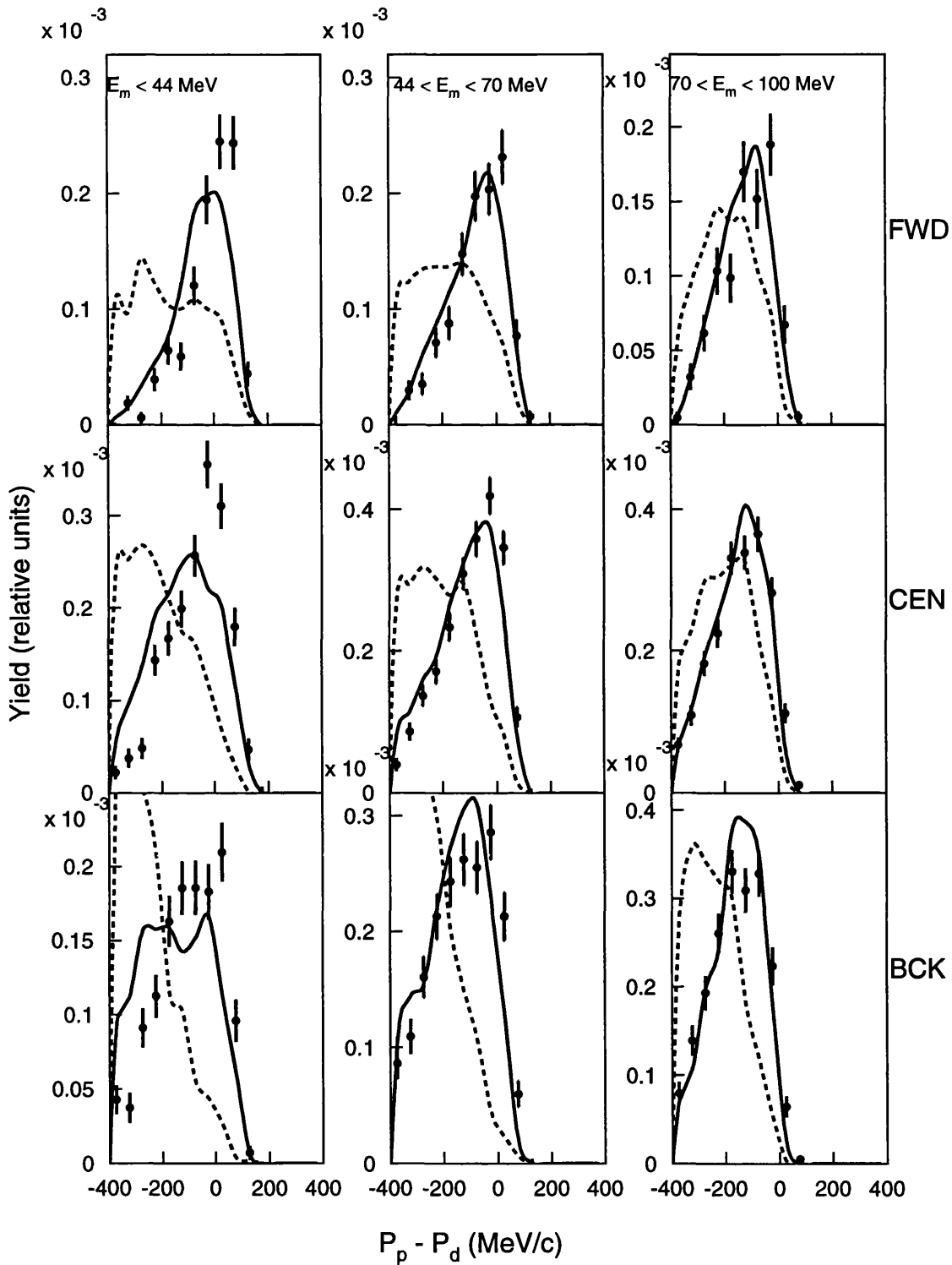


Figure 5.28:  $^{12}\text{C}(\gamma, pd)$  momentum difference distributions, for different missing energy regions and all three detector geometries, for  $E_\gamma=200-250 \text{ MeV}$ . The solid curve represents the direct model; the dashed curve is the pickup model.

$E_\gamma = 250-300 \text{ MeV}$

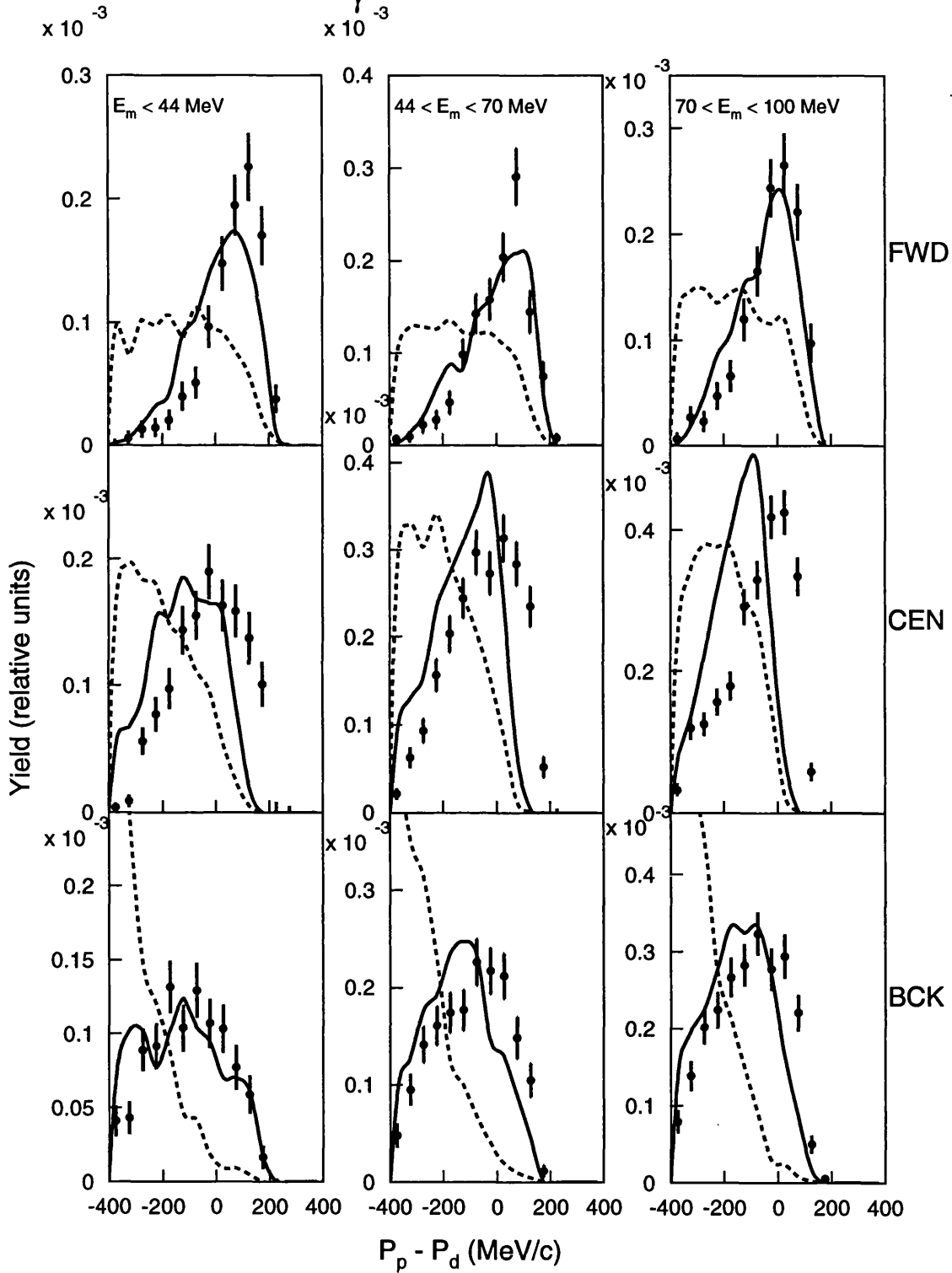


Figure 5.29:  $^{12}\text{C}(\gamma, pd)$  momentum difference distributions, for different missing energy regions and all three detector geometries, for  $E_\gamma=250-300 \text{ MeV}$ . The solid curve represents the direct model; the dashed curve is the pickup model.

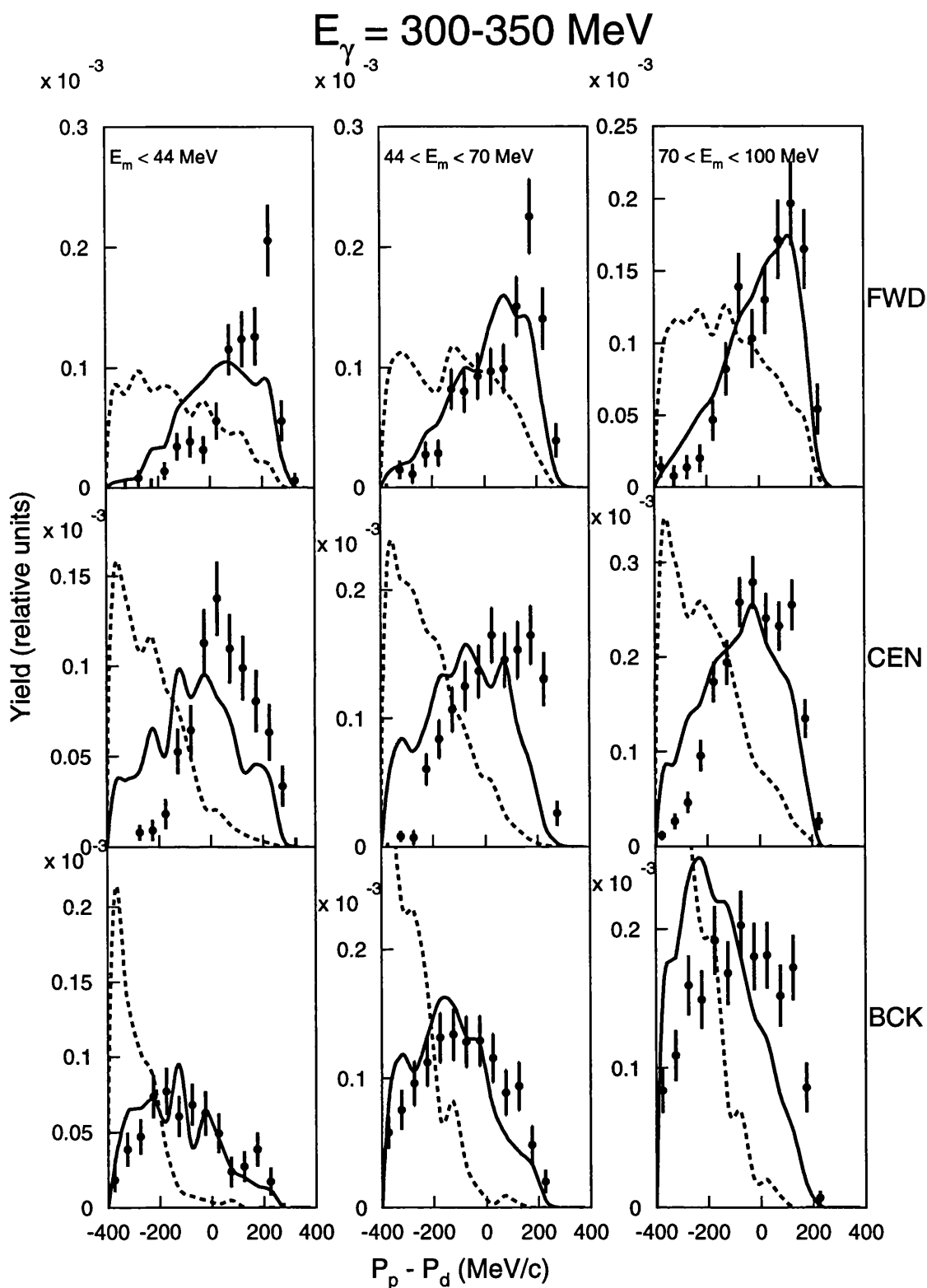


Figure 5.30:  $^{12}\text{C}(\gamma, pd)$  momentum difference distributions, for different missing energy regions and all three detector geometries, for  $E_\gamma = 300-350 \text{ MeV}$ . The solid curve represents the direct model; the dashed curve is the pickup model.

$E_\gamma = 350-400 \text{ MeV}$

$\times 10^{-3}$   $\times 10^{-3}$

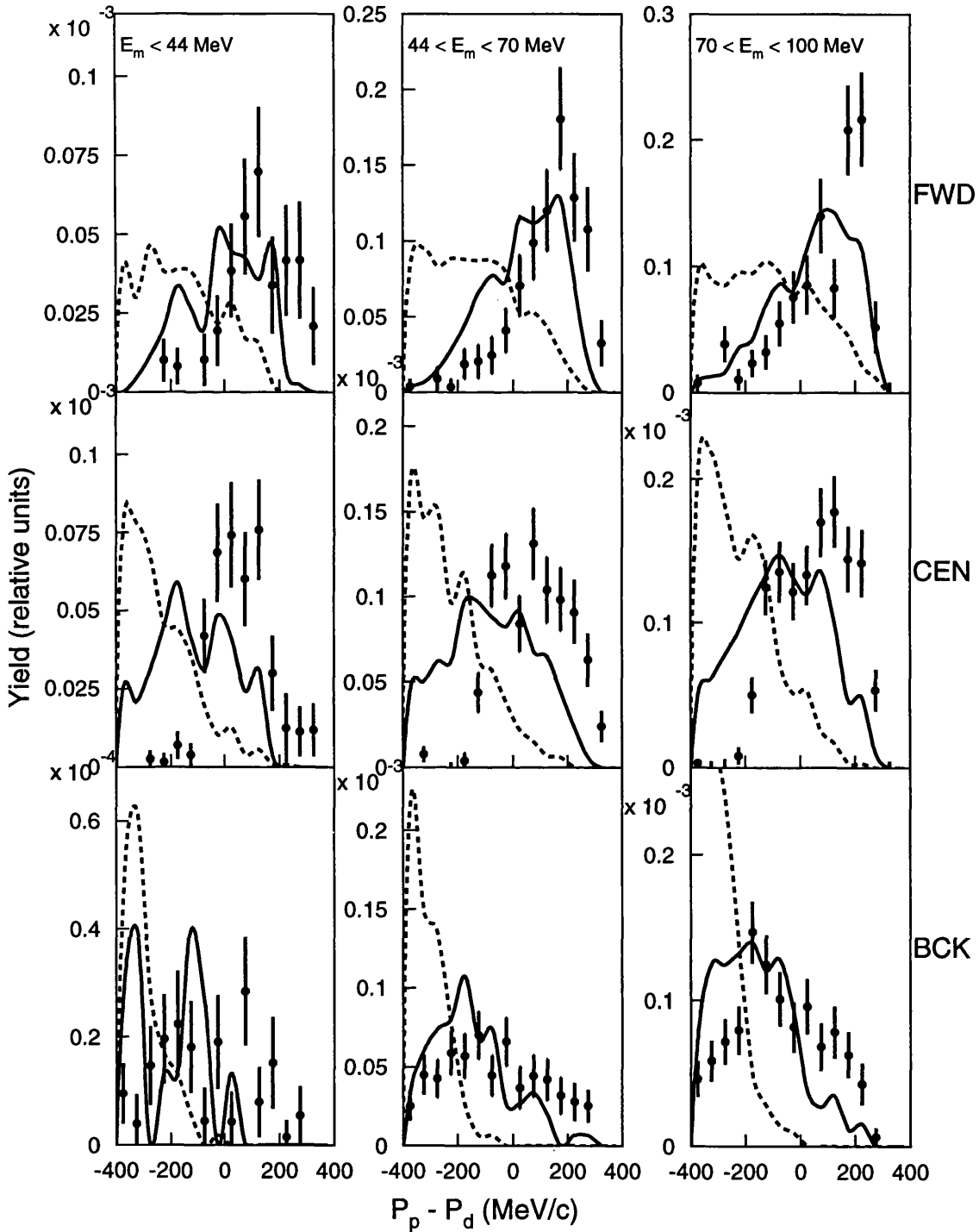


Figure 5.31:  $^{12}\text{C}(\gamma, pd)$  momentum difference distributions, for different missing energy regions and all three detector geometries, for  $E_\gamma = 350-400 \text{ MeV}$ . The solid curve represents the direct model; the dashed curve is the pickup model.

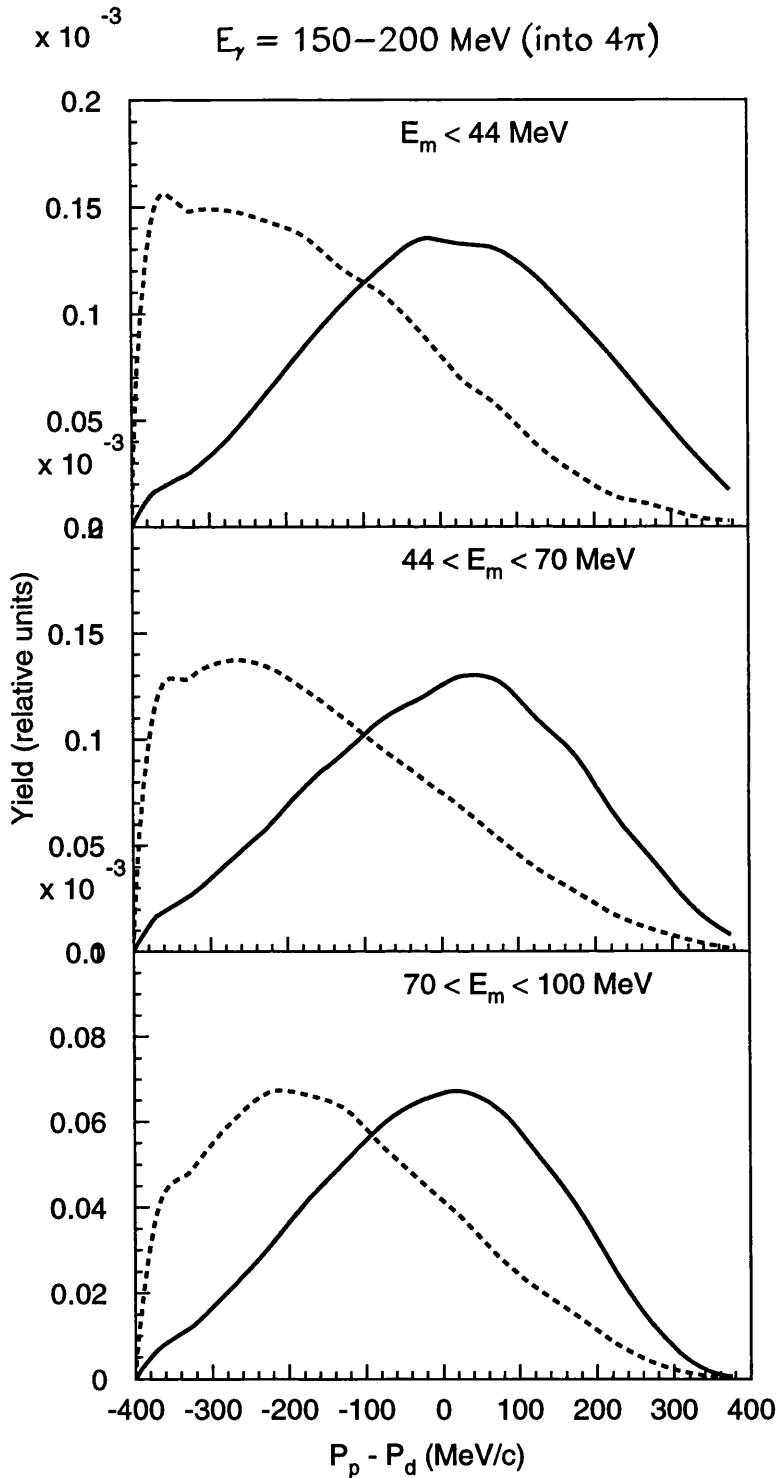


Figure 5.32: Model predictions of the momentum difference distributions into  $4\pi$ , for the central angle detector geometry for  $E_\gamma=150-200 \text{ MeV}$ . The solid curve represents the direct model; the dashed curve is the pickup model.

## **Chapter 6**

# **Conclusions and Outlook**

## 6.1 Conclusions

The work presented in this thesis is the first measurement of the  $^{12}\text{C}(\gamma, \text{pd})$  reaction over the photon energy range 150-400 MeV, using tagged photons with an energy resolution of 2 MeV. The experiment was performed at MAMI-B with the particle detectors PiP and TOF, both detectors having  $\sim 4$  MeV energy resolution. This experimental system then has a missing energy resolution of  $\sim 6$  MeV when measuring the  $(\gamma, \text{pd})$  reaction and can fully determine the kinematics of the reaction in order to explore the processes contributing to the reaction. The overall energy resolution allows the shells from which the particles were emitted to be determined.

In order to shed light on the possible mechanisms leading to this photonuclear reaction, missing energy and momentum spectra have been presented for various photon energy bins and the missing momentum has been examined for different missing energy regions corresponding to particle emission from different shells. The variation of the cross section, presented in the form of double differential cross sections, has been studied both as a function of photon energy and particle angle and has been compared to previous measurements of the  $^3\text{He}(\gamma, \text{pd})$  reaction.

The analysis of this data suggests that the reaction mechanism is similar to that of the two-body breakup of  $^3\text{He}$ . The cross section falls smoothly for all proton angles with increasing photon energy and the angular distribution of the cross section also falls off rapidly as the proton moves to more backward angles. A comparison of the angular distribution measured in this work and those of the  $^{12}\text{C}(\gamma, \text{pn})$  and  $(\gamma, \text{pp})$  reactions at low missing energy has shown that the pd channel has much more in common with the pn case which is dominated by direct 2N mechanisms. The angular distribution has little similarity to that of the pp channel and shows no evidence of the dip structures which are a prominent

feature of this channel.

Further analysis has involved Monte Carlo simulations of the experiment based on two very different possible reaction mechanisms. These simulations include the effect of the detector threshold and acceptances and provide an immediate insight as to the way in which the reaction proceeds. The first simulation was a  $3N$  absorption model which calculates the momenta of the proton and deuteron emitted from the target nucleus following photon absorption on a three nucleon cluster, assuming that the residual nucleus takes no part in the interaction. This model describes the data reasonably well.

The second simulation assumes an initial  $^{12}\text{C}(\gamma, pn)$  reaction followed by an  $n(p, d)$  pickup forming the deuteron in the final state. This model clearly did not describe the data and this process does not play a dominant role in the  $^{12}\text{C}(\gamma, pd)$  reaction, at least at low missing energy. This conclusion is strengthened in view of the fact that the magnitude of the cross section has been shown to be around 3% that of  $^{12}\text{C}(\gamma, pn)$ , which would require the pickup reaction to have an unreasonably large cross section.

Overall the analysis of the experimental data, together with comparisons to similar previous measurements and predictions from Monte Carlo calculations have shown that the reaction mechanism is consistent with some direct process, similar to that observed in  $^3\text{He}$  two-body breakup. These findings will provide constraints on any future microscopic theories and lead to a better understanding of the underlying photonuclear mechanisms.

## 6.2 Outlook

In order to strengthen the conclusions yet further there are developments that can be applied to any future experiment. A significant constraint on the current

measurement, aside from low statistics at high photon energies, is the deuteron energy threshold. A reduction in the flight path of say 50% would go some way to reducing the energy threshold, as would a thinner target and TOF-side  $\Delta E$  layer. A 50 MeV deuteron loses  $\sim 5$  MeV in the target and then a further  $\sim 7$  MeV in the 2mm  $\Delta E$  detector. Reducing the flight path to the TOF detectors brings the added benefit of an increased angular acceptance as would layering the TOF stands 2 deep and spreading out to cover a much wider range of the available phase space. In the present measurement, the back two stands in each bank of four are made redundant when used to detect deuterons because they are mostly stopped in the first layer. The second layer would play a more important role if the stands were brought forward as more of the deuterons would have higher energies at the TOF detectors and would punch through. As has been shown in this thesis the  $^{12}\text{C}(\gamma, \text{pd})$  reaction has an interesting opening angle distribution and the measurement of it would benefit from a wider spread of the deuteron detectors. Although the  $^{12}\text{C}(\gamma, \text{pd})$  reaction appears to be quasi- $^3\text{He}$  like at low missing energy for the present geometry it is possible that other mechanisms are significant especially at higher missing energies. It would therefore be valuable to take data over a wider range of the available phase space. Moving into regions of the phase space away from 'quasi- $^3\text{He}$  kinematics' might allow small contributions from non-quasi- $^3\text{He}$  mechanisms to be identified. It will also aid in resolving the ratio of direct to pickup processes as moving away from regions where direct processes will dominate will also reduce any direct  $(\gamma, \text{pn})$  component which may be the basis of a pickup process. A soon to be published study by the Glasgow group [54] has shown that, in non-quasideuteron regions, 2N mechanisms do indeed die away enabling the examination of reactions which involve 3 or more particles.

The reduction in energy thresholds may also enable the detection on the TOF

side of a significant number of tritons presently barely observable on sail plots like figure 4.2. An increased yield of tritons would enable the study of the  $(\gamma,pt)$  reaction which would be interesting because it is more difficult to see how this reaction would proceed from an initial  $(\gamma,pn)$  reaction in that it would require two pickups or the pickup of a quasideuteron in order to form a  $pnn$  particle in the final state. This reaction may however be a 'quasi- $^4\text{He}$ ' process in which the photon is absorbed on an alpha particle in the nucleus.

In principle, the PiP detector is also able to detect deuterons and so enables the study of this reaction with the corresponding proton detected in TOF. In the present experimental setup the TOF-side proton energy threshold would be  $\sim 28\text{MeV}$  and since the PiP-side energy threshold does not have as great an effect due to the much reduced flight path to PiP, a greater yield of  $pd$  events is to be expected.

Any future measurement of  $^{12}\text{C}(\gamma,pd)$  would of course benefit from some microscopic calculations like those Laget has carried out for  $^3\text{He}$ , although Laget's approach of summing over all possible 'diagrams' may not be feasible for  $^{12}\text{C}$  as the number of possible diagrams will increase significantly. The complications in calculating cross sections even for the simplest case of  $^3\text{He}$  may mean that, for the foreseeable future, realistic calculations will be based on a shell-model approach.

# Appendix A

## F(P) Distributions

## A.1 Introduction

In this appendix the methods employed in producing the 3N  $\mathbf{F}(\mathbf{P})$  distribution are discussed. This distribution is the basis of the direct model simulation as it builds the  $\mathbf{P}^2\mathbf{F}(\mathbf{P})$  distribution where  $\mathbf{P}$  is the 3N momentum vector. It describes the probability of finding three nucleons with total momentum  $\mathbf{P}$ .

## A.2 The Radial Wavefunction

Figure A.1(a) shows the radial wavefunction  $R_{p_{\frac{3}{2}}}$  times  $r$ , where  $r$  is the radial distance from the centre, for a proton in the  $p_{\frac{3}{2}}$  shell of  $^{12}\text{C}$ . The radial wavefunction  $R_{p_{\frac{3}{2}}}$  is produced using an Elton-Swift potential [61]. Figure A.1(a) reflects the fact that the most probable radius of orbit from the centre of the nucleus for a proton in this shell is  $\sim 2.5$  fm. Figure A.2(a) shows the radial wavefunction for a proton in the s-shell. As expected, this has a smaller average radius of orbit. Integrating the function  $(rR)^2$  gives unity.

## A.3 The Wavefunction in Momentum Space

Taking the Fourier transform of the radial wave function gives the wavefunction in momentum space (see section A.5). This momentum probability distribution is the form factor  $\mathbf{F}(\mathbf{p})$  where  $\mathbf{p}$  is the nucleon momentum and is shown on figure A.1(b). For a  $p_{\frac{3}{2}}$  shell proton

$$\mathbf{F}(\mathbf{p}) = \left( \int_0^\infty r^2 j_1(pr) R_{p_{\frac{3}{2}}} dr \right)^2 \quad (\text{A.1})$$

where  $j_1(pr)$  is a spherical Bessel function of order one. The order of this function reflects the angular momentum of the state. Figure A.1(c) replots this form factor on a logarithmic scale and reveals the 'zeroes' which correspond to 'forbidden' mo-

menta, where there is zero probability of finding a nucleon with that momentum. This momentum distribution is also used in the second Monte Carlo simulation of the experiment which is based on a pickup model; from it the momentum of the picked-up proton is chosen, with the condition that it has a momentum value very close to that of the outgoing neutron.

Plotting the same distributions for particles in the s-shell reveals different shapes. Figure A.2(b) shows the  $F(\mathbf{p})$  distribution for an s-shell proton on a linear scale. It can be seen that the most probable momenta are close to zero and the probability rapidly falls off with increasing momentum reflecting the fact that the potential is infinite at the origin. Figure A.2(c) shows the distribution on a logarithmic scale.

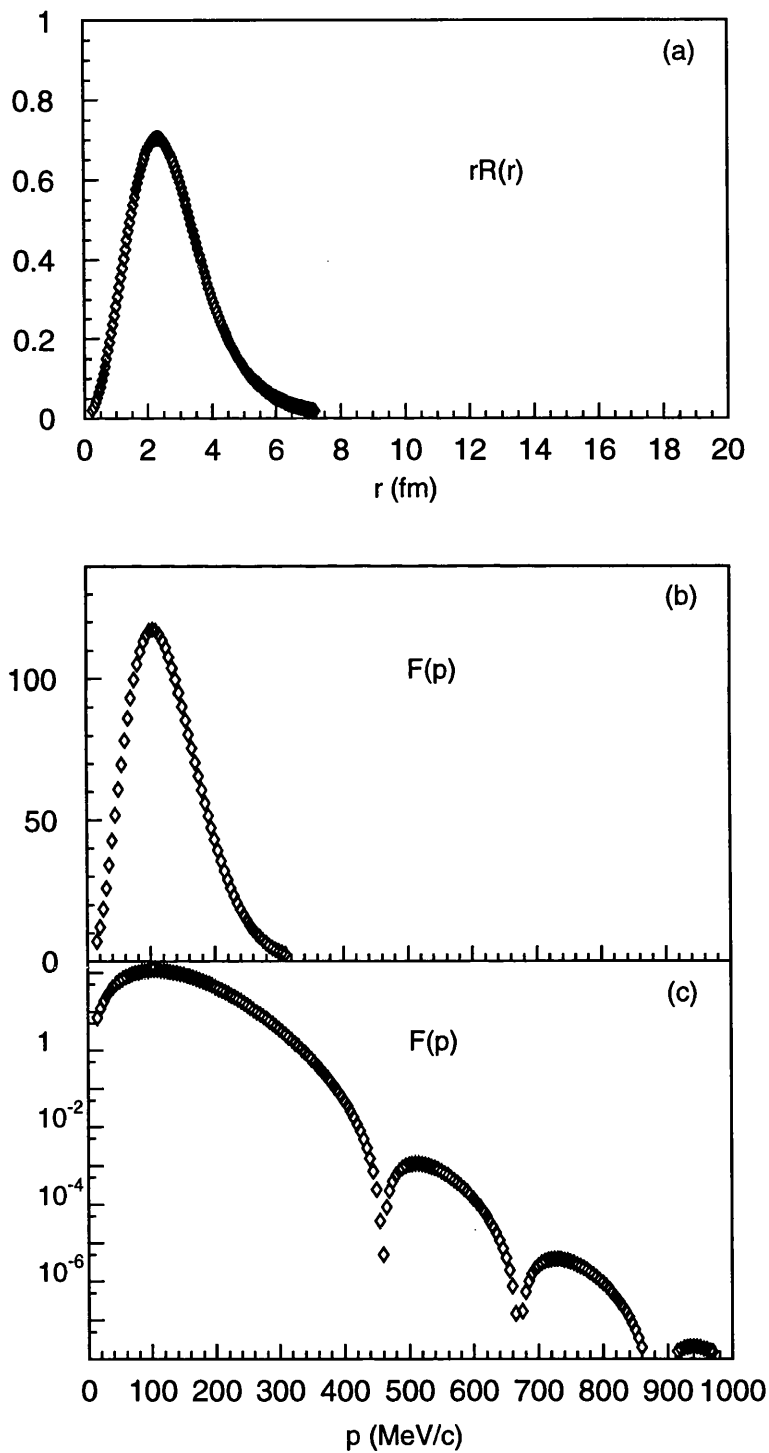
Distributions for a  $p_{3/2}$  particle

Figure A.1: Distributions for a single  $p_{3/2}$ -shell particle; (a) is the radial wavefunction times  $r$ ; (b) is the  $F(p)$  distribution for a single  $p$ -shell nucleon and (c) is the same  $F(p)$  distribution plotted on a logarithmic scale.

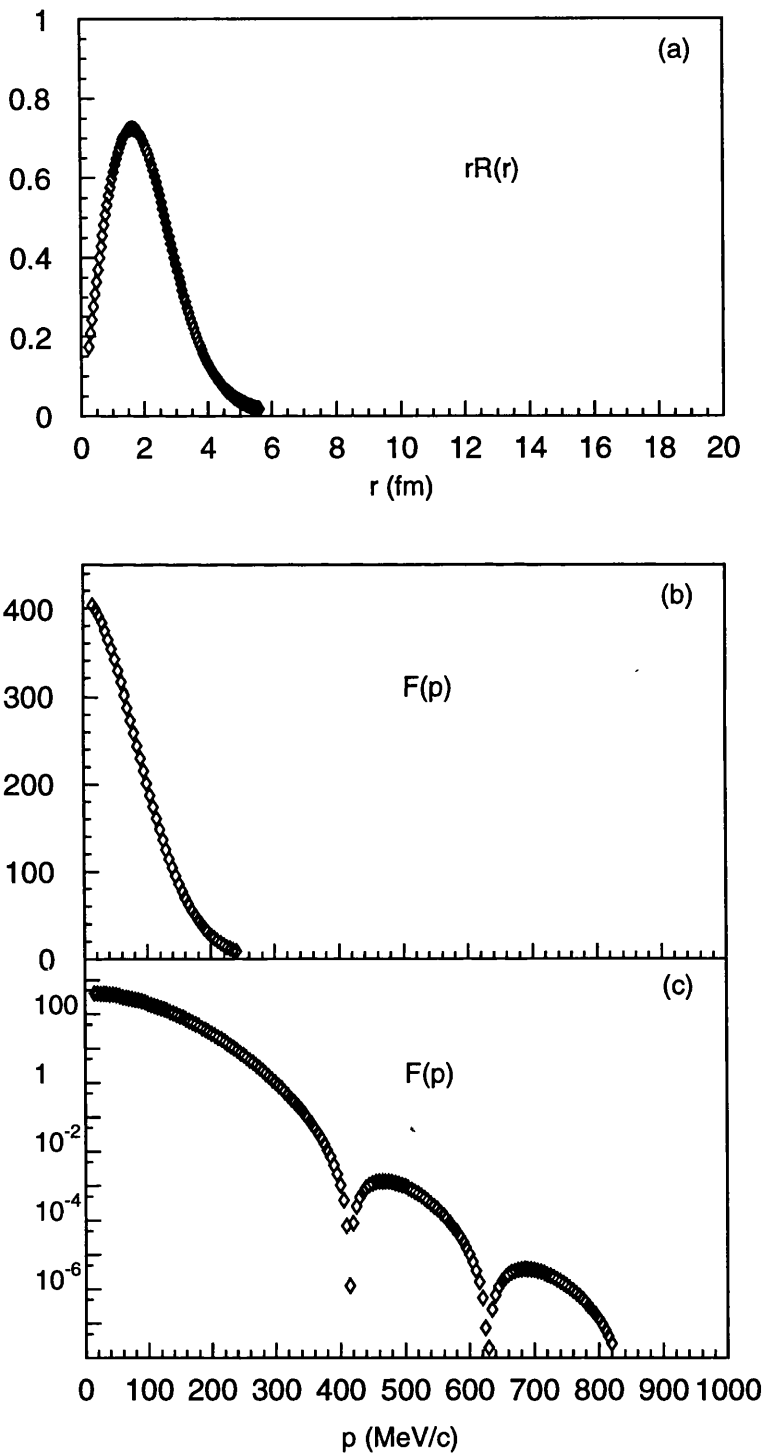
Distributions for a  $s_{1/2}$  particle

Figure A.2: Distributions for a single  $s_{1/2}$ -shell particle; (a) is the radial wavefunction times  $r$ ; (b) is the  $F(p)$  distribution for a single  $s$ -shell nucleon and (c) is the same  $F(p)$  distribution plotted on a logarithmic scale.

## A.4 Mixing Three Wavefunctions

### A.4.1 Three $p_{\frac{3}{2}}$ Shell Particles

Before folding together three single particle wavefunctions to obtain an  $F(P)$  distribution for the  ${}^3\text{He}$  cluster in the nucleus, the mixing of the angular momenta of the particles has to be considered. The following is a description of the coupling of three  $p_{\frac{3}{2}}$  shell wavefunctions.

A p-shell particle has angular momentum  $l=1$  and so the possible angular momenta of the combination of *two* such particles are  $l=0, 1$  or  $2$ . Using the Clebsch-Gordon coefficient notation

$$\langle l_1 l_2 m_1 m_2 \mid l m \rangle \quad (\text{A.2})$$

where  $l$  is the angular momentum quantum number of the combined state and  $m$  is the quantum number which takes one of the  $2l+1$  quantum numbers from  $-l, -l+1, \dots, l$ , the coefficients for each possible outcome can be determined as follows

$$\langle 1100 \mid 00 \rangle = -\sqrt{\frac{1}{3}} \quad (\text{A.3})$$

$$\langle 1100 \mid 10 \rangle = 0 \quad (\text{A.4})$$

$$\langle 1100 \mid 20 \rangle = -\sqrt{\frac{2}{3}} \quad (\text{A.5})$$

[it should be noted that when summing over all possible magnetic substates we are only left with the  $m_1=m_2=0$  states, [16]] This means that  $\frac{1}{3}$  of the time the combined system produces an  $l=0$  state and is in an  $l=2$  state in the remaining  $\frac{2}{3}$  of the time.

If the third  $l=1$  particle is now coupled to the  $l=0$  and  $l=2$  states above, the possible outcomes for the angular momenta of the tri-particle system are  $l=1$  when coupling to the zero state and  $l=1, 2$  or  $3$  when coupling to the angular

momentum 2 state. The Clebsch-Gordon coefficients are

$$\langle 2100 | 10 \rangle = -\sqrt{\frac{2}{5}} \quad (\text{A.6})$$

$$\langle 2100 | 20 \rangle = 0 \quad (\text{A.7})$$

$$\langle 2100 | 30 \rangle = -\sqrt{\frac{3}{5}} \quad (\text{A.8})$$

This means that  $\frac{2}{5}$  of the time an  $l=1$  state is produced and the remaining  $\frac{3}{5}$  of the time, the combined system is in an  $l=3$  state.

So overall,

$$l = 1 \text{ occurs } \frac{1}{3} + \frac{2}{3} \times \frac{2}{5} = \frac{9}{15} \text{ of the time} \quad (\text{A.9})$$

and

$$l = 3 \text{ occurs } \frac{2}{3} \times \frac{3}{5} = \frac{6}{15} \text{ of the time} \quad (\text{A.10})$$

This means that three p-shell particles will produce an  $F(\mathbf{P})$  distribution as follows

$$F(\mathbf{P}) = \frac{9}{15} \left( \int_0^\infty r^2 j_1(pr) R_{p\frac{3}{2}}^3 dr \right)^2 + \frac{6}{15} \left( \int_0^\infty r^2 j_3(pr) R_{p\frac{3}{2}}^3 dr \right)^2 \quad (\text{A.11})$$

The resulting  $F(\mathbf{P})$  distribution is shown on figure A.3(a). Figure A.3(b) shows the distribution on a logarithmic scale.

The  $P^2F(\mathbf{P})$  distribution is shown on figure A.3(c).

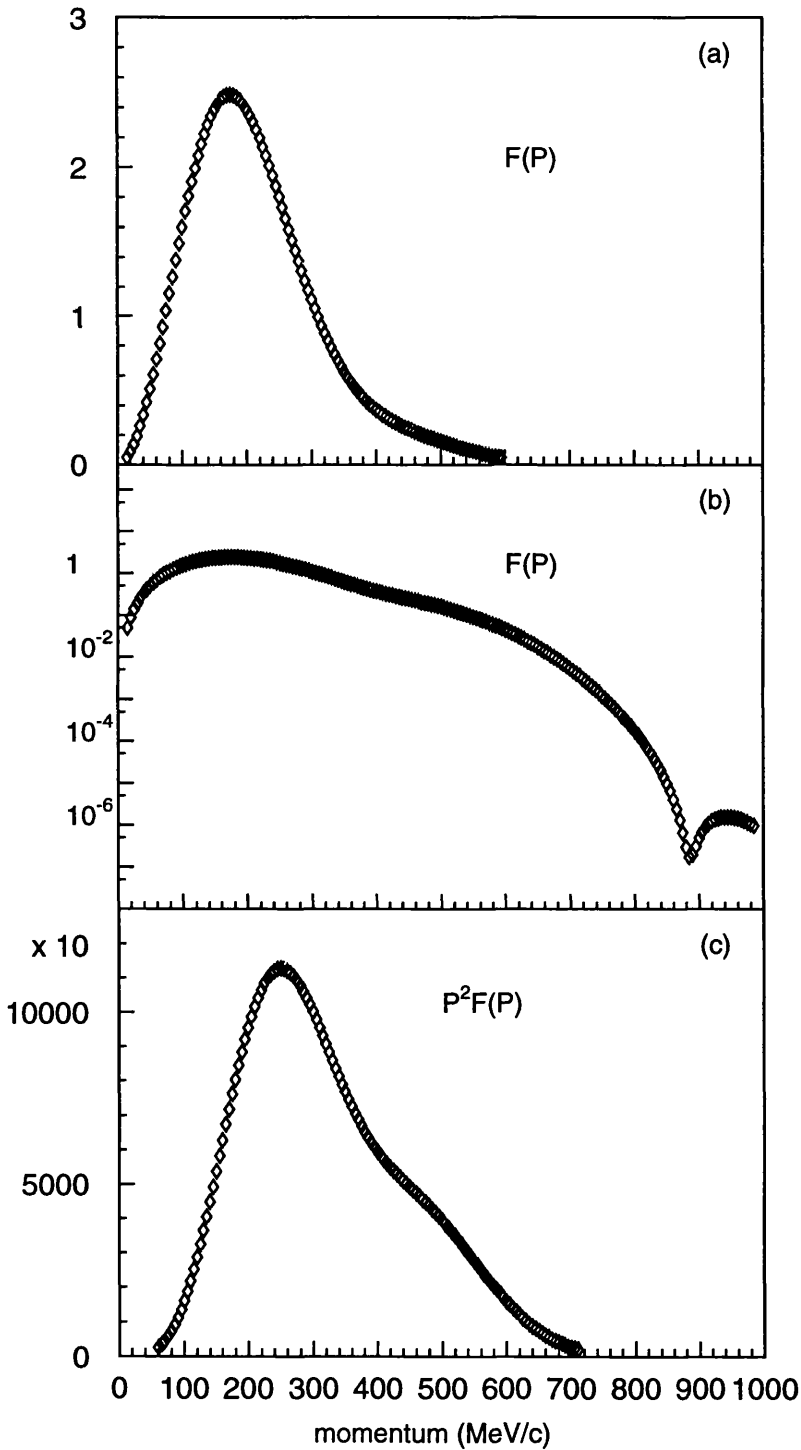
Distributions for three  $p_{3/2}$  particles

Figure A.3: Distributions for three  $p_{3/2}$ -shell particles; (a) is the  $F(P)$  distribution for three  $p$ -shell nucleons; (b) is the same  $F(P)$  distribution plotted on a logarithmic scale and (c) is the resulting  $P^2 F(P)$  distribution.

### A.4.2 Mixing Two $p_{\frac{3}{2}}$ Particles with an $s_{\frac{1}{2}}$ Shell Particle

Following similar arguments to those above,  $pps$  mixing produces a final state which is an admixture of  $l=0$  and  $l=2$  states. The resulting  $F(\mathbf{P})$  distribution is built up from

$$F(\mathbf{P}) = \frac{1}{3} \left( \int_0^\infty r^2 j_0(pr) R_{p\frac{3}{2}}^2 R_{s\frac{1}{2}} dr \right)^2 + \frac{2}{3} \left( \int_0^\infty r^2 j_2(pr) R_{p\frac{3}{2}}^2 R_{s\frac{1}{2}} dr \right)^2 \quad (\text{A.12})$$

and is shown on figure A.4(a).

Figure A.4(b) shows the distribution on a logarithmic scale.

The  $\mathbf{P}^2 F(\mathbf{P})$  distribution is shown on figure A.4(c).

## Distributions for pps particles

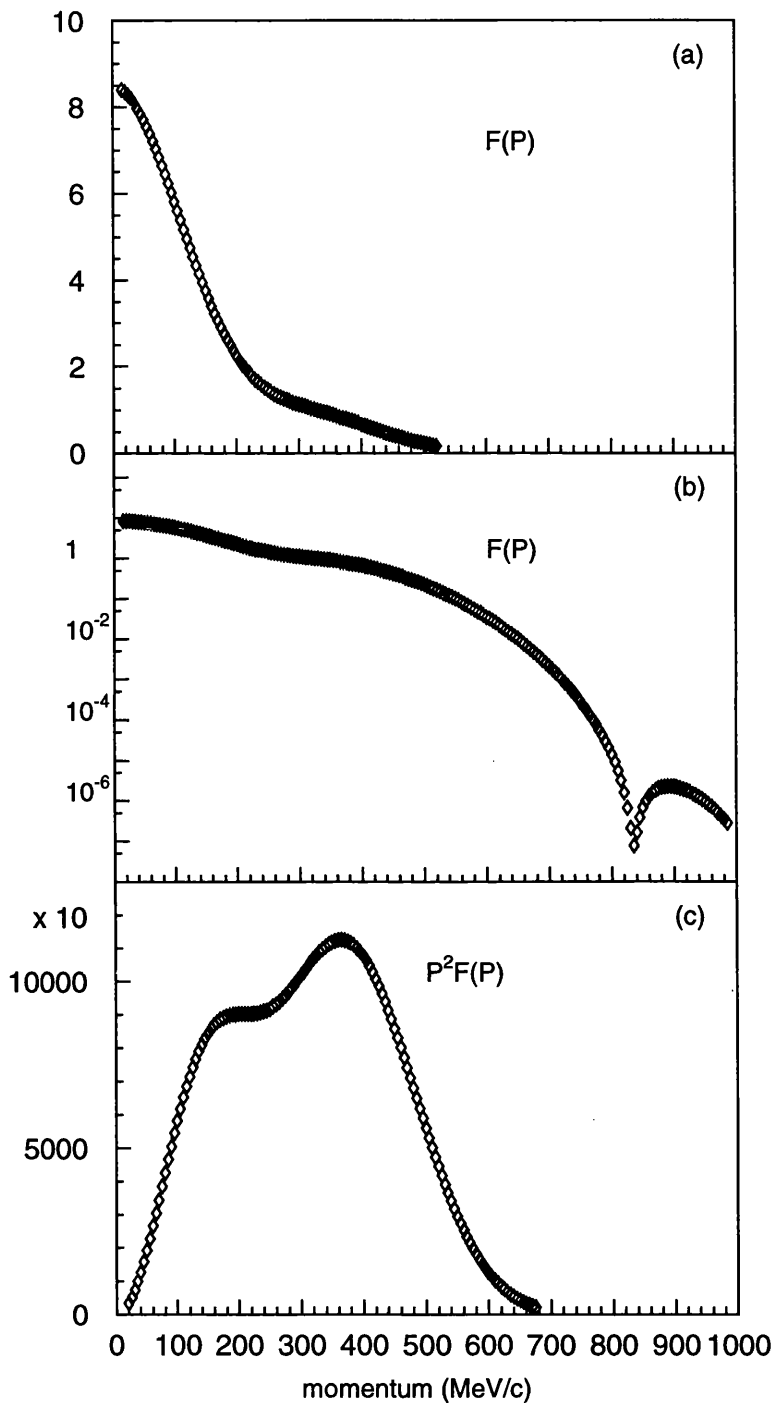


Figure A.4: Distributions for two  $p_{3/2}$ -shell particles folded with a third  $s_{1/2}$ -shell particle; (a) is the  $F(P)$  distribution for the three nucleons; (b) is the same  $F(P)$  distribution plotted on a logarithmic scale and (c) is the resulting  $P^2 F(P)$  distribution.

## A.5 Wavefunctions

In configuration space the wavefunction for a single nucleon is

$$\Psi(\underline{r}) = \sum_{lm} C_{lm} R_l(r) Y_{lm}(\underline{r}) \quad (\text{A.13})$$

where  $C_{lm}$  is a normalisation constant which can be obtained using Clebsch-Gordon tables,  $R_l$  is the radial wavefunction and  $Y_{lm}$  is a spherical harmonic.

The normalisation condition

$$\int \Psi * \Psi d\underline{r} = 1 \quad (\text{A.14})$$

is ensured if

$$\int |R_l(r)|^2 r^2 dr = 1 \quad (\text{A.15})$$

and

$$\sum_{lm} |C_{lm}|^2 = 1 \quad (\text{A.16})$$

In momentum space the wavefunction is

$$\Phi(\underline{p}) = (2\pi)^{-\frac{3}{2}} \int e^{-i\underline{p}\cdot\underline{r}} \Psi(\underline{r}) d\underline{r} \quad (\text{A.17})$$

Using

$$\int e^{-i\underline{p}\cdot\underline{r}} = \sum_{lm} 4\pi (-i)^l j_l(pr) Y_{lm}(r) Y_{lm}^*(r) \quad (\text{A.18})$$

and integrating, we obtain

$$\Phi(\underline{p}) = \sum_{lm} (-i)^l C_{lm} \Theta_l(p) Y_{lm}(p) \quad (\text{A.19})$$

where

$$\Theta_l(p) = \sqrt{\frac{2}{\pi}} \int r^2 j_l(pr) R_l(r) dr \quad (\text{A.20})$$

The momentum distribution integrating over all possible angles is then

$$\int \Phi^*(\underline{p}) \Phi(\underline{p}) d\Omega_p p^2 dp = \sum_{lm} |C_{lm} \Theta_l(p)|^2 p^2 dp = F(p) p^2 dp \quad (\text{A.21})$$

# Appendix B

## Table of Results

$$E_\gamma = 175 \pm 10 \text{ MeV}$$

TOF side deuteron		PIP side proton		cross section
$\theta_{lab}(\text{deg})$	solid angle(sr)	$\theta_{lab}(\text{deg})$	solid angle(sr)	$d^2\sigma/d\Omega_n d\Omega_p(\text{nb}/\text{sr}^2)$
102.8	0.0722	59.5	0.275	$131.9 \pm 23.9$
111.7	0.0722	51.9	0.268	$130.4 \pm 24.6$
122.7	0.0638	42.9	0.253	$94.4 \pm 23.6$
131.1	0.0644	36.2	0.237	$28.0 \pm 24.9$
51.9	0.0733	110.8	0.258	$249.2 \pm 30.2$
63.5	0.0653	97.7	0.273	$272.4 \pm 34.7$
72.0	0.0654	88.7	0.276	$229.5 \pm 42.2$
82.9	0.0749	77.8	0.270	$221.3 \pm 25.9$
92.0	0.0747	69.2	0.258	$244.6 \pm 29.6$
22.9	0.0739	147.6	0.214	$159.5 \pm 30.1$
33.3	0.0657	133.7	0.257	$172.0 \pm 33.8$
41.9	0.0658	122.8	0.270	$337.7 \pm 34.8$
53.7	0.0747	108.7	0.272	$222.6 \pm 28.1$
62.8	0.0758	98.5	0.263	$243.6 \pm 28.6$

Table B.1:  $(\gamma, pd)$  cross sections for  $E_\gamma=175 \text{ MeV}$  and  $E_m < 44 \text{ MeV}$

$$E_\gamma = 225 \pm 10 \text{ MeV}$$

TOF side deuteron		PIP side proton		cross section
theta(deg)	solid angle(sr)	theta(deg)	solid angle(sr)	$d^2\sigma/d\Omega_n d\Omega_p (nb/sr^2)$
102.8	0.0722	57.1	0.273	$381.7 \pm 45.9$
111.7	0.0722	49.7	0.265	$345.9 \pm 42.3$
122.7	0.0638	41.0	0.248	$237.7 \pm 45.1$
131.1	0.0644	34.6	0.232	$105.1 \pm 44.6$
51.9	0.0733	107.8	0.262	$369.4 \pm 37.1$
63.5	0.0653	94.6	0.275	$336.7 \pm 42.4$
72.0	0.0654	85.7	0.275	$426.2 \pm 58.2$
82.9	0.0749	74.9	0.266	$327.4 \pm 35.8$
92.0	0.0747	66.5	0.253	$405.6 \pm 40.3$
22.9	0.0739	145.8	0.228	$262.8 \pm 36.7$
33.3	0.0657	131.3	0.261	$255.4 \pm 38.8$
41.9	0.0658	120.0	0.272	$287.3 \pm 42.5$
53.7	0.0747	105.7	0.270	$316.3 \pm 35.4$
62.8	0.0758	95.4	0.257	$400.8 \pm 41.5$

Table B.2:  $(\gamma, pd)$  cross sections for  $E_\gamma = 225 \text{ MeV}$  and  $E_m < 44 \text{ MeV}$

$$E_\gamma = 275 \pm 10 \text{ MeV}$$

TOF side deuteron		PIP side proton		result
theta(deg)	solid angle(sr)	theta(deg)	solid angle(sr)	$d^2\sigma/d\Omega_n d\Omega_p (nb/sr^2)$
102.8	0.0722	55.0	0.272	$404.9 \pm 55.7$
111.7	0.0722	47.8	0.262	$508.5 \pm 62.9$
122.7	0.0638	39.3	0.245	$356.4 \pm 70.0$
131.1	0.0644	33.2	0.227	$81.4 \pm 42.3$
51.9	0.0733	105.1	0.266	$214.9 \pm 31.7$
63.5	0.0653	92.0	0.276	$206.0 \pm 39.6$
72.0	0.0654	83.1	0.273	$373.3 \pm 66.6$
82.9	0.0749	72.5	0.263	$345.6 \pm 41.0$
92.0	0.0747	64.2	0.248	$465.2 \pm 51.4$
22.9	0.0739	144.0	0.233	$210.1 \pm 35.9$
33.3	0.0657	129.1	0.264	$194.9 \pm 43.9$
41.9	0.0658	117.6	0.273	$262.4 \pm 47.7$
53.7	0.0747	103.0	0.268	$211.6 \pm 35.6$
62.8	0.0758	92.7	0.253	$320.3 \pm 42.2$

Table B.3:  $(\gamma, pd)$  cross sections for  $E_\gamma=275 \text{ MeV}$  and  $E_m < 44 \text{ MeV}$

$$E_\gamma = 325 \pm 10 \text{ MeV}$$

TOF side deuteron		PIP side proton		result
theta(deg)	solid angle(sr)	theta(deg)	solid angle(sr)	$d^2\sigma/d\Omega_n d\Omega_p (nb/sr^2)$
102.8	0.0722	53.1	0.270	$381.0 \pm 63.5$
111.7	0.0722	46.1	0.261	$341.1 \pm 58.1$
122.7	0.0638	38.0	0.243	$482.2 \pm 92.1$
51.9	0.0733	102.8	0.269	$135.2 \pm 28.9$
63.5	0.0653	89.6	0.276	$163.8 \pm 39.6$
72.0	0.0654	80.8	0.272	$123.1 \pm 45.5$
82.9	0.0749	70.3	0.260	$283.6 \pm 44.0$
92.0	0.0747	62.2	0.244	$295.2 \pm 44.4$
22.9	0.0739	142.4	0.238	$127.2 \pm 32.4$
33.3	0.0657	127.0	0.267	$152.0 \pm 38.0$
41.9	0.0658	115.3	0.274	$103.0 \pm 34.3$
53.7	0.0747	100.6	0.265	$125.0 \pm 31.2$
62.8	0.0758	90.4	0.248	$253.3 \pm 43.0$

Table B.4:  $(\gamma, pd)$  cross sections for  $E_\gamma = 325 \text{ MeV}$  and  $E_m < 44 \text{ MeV}$

$$E_\gamma = 375 \pm 10 \text{ MeV}$$

TOF side deuteron		PIP side proton		result
theta(deg)	solid angle(sr)	theta(deg)	solid angle(sr)	$d^2\sigma/d\Omega_n d\Omega_p (nb/sr^2)$
102.8	0.0722	51.5	0.267	$118.5 \pm 41.9$
111.7	0.0722	44.7	0.256	$224.1 \pm 56.6$
122.7	0.0638	36.7	0.237	$129.1 \pm 59.8$
51.9	0.0733	100.6	0.271	$112.6 \pm 28.7$
63.5	0.0653	87.4	0.275	$95.4 \pm 31.8$
72.0	0.0654	78.7	0.270	$53.9 \pm 35.0$
82.9	0.0749	68.3	0.256	$173.8 \pm 39.7$
92.0	0.0747	60.3	0.228	$125.8 \pm 33.5$
22.9	0.0739	140.9	0.242	$21.3 \pm 17.5$
33.3	0.0657	125.1	0.269	$21.5 \pm 21.8$
41.9	0.0658	113.2	0.274	$13.2 \pm 16.9$
53.7	0.0747	98.4	0.262	$41.3 \pm 20.1$
62.8	0.0758	88.2	0.234	$85.9 \pm 29.5$

Table B.5:  $(\gamma, pd)$  cross sections for  $E_\gamma = 375 \text{ MeV}$  and  $E_m < 44 \text{ MeV}$

$$E_\gamma = 175 \pm 10 \text{ MeV}$$

TOF side deuteron		PIP side proton		cross section
$\theta_{lab}(\text{deg})$	solid angle(sr)	$\theta_{lab}(\text{deg})$	solid angle(sr)	$d^2\sigma/d\Omega_n d\Omega_p (\text{nb}/\text{sr}^2)$
102.8	0.0722	60.7	0.276	$222.2 \pm 31.0$
111.7	0.0722	53.0	0.270	$146.5 \pm 26.8$
122.7	0.0638	43.8	0.254	$117.5 \pm 26.4$
131.1	0.0644	37.0	0.238	$71.4 \pm 15.5$
51.9	0.0733	112.2	0.255	$211.4 \pm 28.0$
63.5	0.0653	99.1	0.272	$233.2 \pm 34.8$
72.0	0.0654	90.1	0.276	$232.1 \pm 42.2$
82.9	0.0749	79.2	0.271	$197.0 \pm 25.8$
92.0	0.0747	70.5	0.260	$122.5 \pm 22.0$
22.9	0.0739	148.5	0.203	$209.5 \pm 34.9$
33.3	0.0657	134.9	0.254	$282.4 \pm 42.8$
41.9	0.0658	124.1	0.269	$234.0 \pm 37.6$
53.7	0.0747	110.1	0.273	$231.1 \pm 30.3$
62.8	0.0758	99.9	0.265	$165.9 \pm 26.0$

Table B.6:  $(\gamma, pd)$  cross sections for  $E_\gamma=175 \text{ MeV}$  and  $E_m=44-70 \text{ MeV}$

$$E_\gamma = 225 \pm 10 \text{ MeV}$$

TOF side deuteron		PIP side proton		cross section
theta(deg)	solid angle(sr)	theta(deg)	solid angle(sr)	$d^2\sigma/d\Omega_n d\Omega_p (nb/sr^2)$
102.8	0.0722	58.0	0.274	$363.4 \pm 43.3$
111.7	0.0722	50.6	0.266	$265.3 \pm 39.6$
122.7	0.0638	41.7	0.250	$346.3 \pm 53.7$
131.1	0.0644	35.2	0.234	$157.9 \pm 44.2$
51.9	0.0733	109.0	0.261	$425.6 \pm 42.3$
63.5	0.0653	95.9	0.274	$492.3 \pm 50.5$
72.0	0.0654	86.9	0.275	$431.5 \pm 60.8$
82.9	0.0749	76.1	0.268	$476.8 \pm 42.7$
92.0	0.0747	67.6	0.256	$430.7 \pm 42.3$
22.9	0.0739	146.5	0.226	$322.1 \pm 42.7$
33.3	0.0657	132.3	0.259	$338.6 \pm 47.5$
41.9	0.0658	121.2	0.272	$305.9 \pm 45.2$
53.7	0.0747	106.9	0.273	$352.5 \pm 37.3$
62.8	0.0758	96.6	0.259	$458.4 \pm 43.6$

Table B.7:  $(\gamma, pd)$  cross sections for  $E_\gamma = 225 \text{ MeV}$  and  $E_m = 44-70 \text{ MeV}$

$$E_\gamma = 275 \pm 10 \text{ MeV}$$

TOF side deuteron		PIP side proton		result
theta(deg)	solid angle(sr)	theta(deg)	solid angle(sr)	$d^2\sigma/d\Omega_n d\Omega_p (nb/sr^2)$
102.8	0.0722	55.8	0.272	$380.6 \pm 55.7$
111.7	0.0722	48.5	0.264	$379.7 \pm 54.9$
122.7	0.0638	40.0	0.246	$394.4 \pm 69.7$
131.1	0.0644	33.7	0.229	$177.5 \pm 58.1$
51.9	0.0733	106.2	0.265	$409.3 \pm 46.5$
63.5	0.0653	93.1	0.275	$453.4 \pm 58.3$
72.0	0.0654	84.1	0.274	$624.4 \pm 85.0$
82.9	0.0749	73.5	0.264	$524.9 \pm 50.5$
92.0	0.0747	65.1	0.250	$545.6 \pm 53.5$
22.9	0.0739	144.7	0.231	$304.0 \pm 47.4$
33.3	0.0657	130.0	0.263	$388.5 \pm 57.8$
41.9	0.0658	118.6	0.273	$379.0 \pm 55.6$
53.7	0.0747	104.1	0.269	$409.9 \pm 47.3$
62.8	0.0758	93.8	0.255	$509.9 \pm 54.1$

Table B.8:  $(\gamma, pd)$  cross sections for  $E_\gamma=275 \text{ MeV}$  and  $E_m=44-70 \text{ MeV}$

$$E_\gamma = 325 \pm 10 \text{ MeV}$$

TOF side deuteron		PIP side proton		result
theta(deg)	solid angle(sr)	theta(deg)	solid angle(sr)	$d^2\sigma/d\Omega_n d\Omega_p (nb/sr^2)$
102.8	0.0722	53.9	0.270	$530.0 \pm 73.2$
111.7	0.0722	46.8	0.260	$403.3 \pm 65.9$
122.7	0.0638	38.5	0.243	$383.9 \pm 79.8$
51.9	0.0733	103.7	0.268	$242.4 \pm 38.7$
63.5	0.0653	90.6	0.276	$346.1 \pm 58.1$
72.0	0.0654	81.7	0.273	$376.0 \pm 74.6$
82.9	0.0749	71.2	0.261	$416.5 \pm 53.5$
92.0	0.0747	63.0	0.246	$466.4 \pm 59.6$
22.9	0.0739	143.1	0.236	$204.7 \pm 40.9$
33.3	0.0657	127.9	0.265	$213.3 \pm 49.2$
41.9	0.0658	116.2	0.273	$214.7 \pm 47.7$
53.7	0.0747	101.6	0.266	$292.3 \pm 45.5$
62.8	0.0758	91.3	0.250	$334.2 \pm 50.2$

Table B.9:  $(\gamma, pd)$  cross sections for  $E_\gamma = 325 \text{ MeV}$  and  $E_m = 44\text{-}70 \text{ MeV}$

$$E_\gamma = 375 \pm 10 \text{ MeV}$$

TOF side deuteron		PIP side proton		result
theta(deg)	solid angle(sr)	theta(deg)	solid angle(sr)	$d^2\sigma/d\Omega_n d\Omega_p (nb/sr^2)$
102.8	0.0722	52.2	0.268	$292.8 \pm 66.4$
111.7	0.0722	45.3	0.257	$426.0 \pm 82.1$
122.7	0.0638	37.2	0.239	$412.2 \pm 81.1$
51.9	0.0733	101.5	0.269	$212.5 \pm 38.6$
63.5	0.0653	88.3	0.276	$282.7 \pm 42.2$
72.0	0.0654	79.5	0.273	$330.7 \pm 37.3$
82.9	0.0749	69.1	0.258	$303.0 \pm 49.2$
92.0	0.0747	61.1	0.238	$407.1 \pm 58.9$
22.9	0.0739	141.5	0.240	$142.2 \pm 34.9$
33.3	0.0657	125.9	0.268	$156.8 \pm 45.9$
41.9	0.0658	114.0	0.274	$66.0 \pm 31.6$
53.7	0.0747	99.3	0.263	$121.1 \pm 33.9$
62.8	0.0758	89.1	0.245	$243.5 \pm 46.1$

Table B.10:  $(\gamma, pd)$  cross sections for  $E_\gamma=375 \text{ MeV}$  and  $E_m=44-70 \text{ MeV}$

# Bibliography

- [1] N. d'Hose *et al.*, Phys. Rev. Letters 63 (1989) 856
- [2] G. Audit *et al.*, Phys. Lett.B 227 (1989) 331
- [3] G. Audit *et al.*, Nucl. Phys. 614 No.4 (1997) 461-471
- [4] A.J. Sarty *et al.*, Phys. Rev. C 47 (1993) 459
- [5] V. Isbert *et al.*, Nucl. Phys. 578 (1994) 525
- [6] J.S. Levinger, Phys. Rev. 84 (1951) 43.
- [7] D. Walker, Phys. Rev. 81 (1951) 634.
- [8] S. Kikuchi, Phys. Rev. 80 (1950) 492.
- [9] C. Levinthal and A. Silverman, Phys. Rev. 82 (1951) 822.
- [10] M.Q. Barton and J.H. Smith, Phys. Rev. 110 (1958) 1143.
- [11] J. Garvey *et al.*, Nucl. Phys. 70 (1965) 241.
- [12] I.L. Smith, J. Garvey, J.G. Rutherglen and G.R. Brookes, Nucl. Phys. B1  
(1967) 483.
- [13] P.C. Stein *et al.*, Phys. Rev. 119 (1960) 348.
- [14] I.L. Smith *et al.*, Nucl. Phys B1 (1967) 483-493

- [15] A. Stadler *et al.*, Phys. Rev. C 51 (1995) 2896.
- [16] K. Gottfried, Nucl. Phys. 5 (1958) 557.
- [17] S.N. Dancer *et al.*, Phys. Rev. Lett. 61 (1988) 1170.
- [18] I.J.D. MacGregor *et al.*, Nucl. Phys. A533 (1991) 269.
- [19] J.C. McGeorge *et al.*, Phys. Rev. C51 (1995) 1967.
- [20] S.M. Doran *et al.*, Nucl. Phys. A559 (1993) 347.
- [21] S. Klein, Universität Tübingen PhD Thesis (1990).
- [22] P.D. Harty *et al.*, Phys. Lett. B 380 (1996) 247-252.
- [23] J. Ryckebusch *et al.* Nucl.Phys. A568 (1994) 828.
- [24] P.D. Harty *et al.*, Phys. Rev. C 47 (1993) 2185.
- [25] J. Ryckebusch *et al.*, Phys. Lett. B 291 (1992) 213.
- [26] H. Hartmann *et al.* Conference Proceedings...
- [27] D.I. Sober *et al.*, Phys. Rev. C 28 (1983) 2234
- [28] P.E. Argan *et al.*, Nucl. Phys. 237 (1975) 447
- [29] H.J. Gassen *et al.*, Z. Phys. 303 (1981) 35
- [30] P. Picozza *et al.*, Nucl. Phys. 157 (1970) 190
- [31] J.P. Didelez *et al.*, Nucl. Phys. 143 (1970) 602
- [32] M.A. Pickar *et al.*, Phys. Rev. C 35 (1987) 37
- [33] J.M. Cameron *et al.*, Nucl. Phys. 424 (1984) 549

- [34] W.J. Briscoe *et al.*, Phys. Rev. C 32 (1985) 1956
- [35] N.R. Kolb, Phys. Rev. C 49 (1993) 2586.
- [36] C.A. Heusch *et al.*, Phys. Rev. Lett 37 (1976) 405.
- [37] J.M. Laget, Phys. Rev. C 38 (1988) 2993.
- [38] J.M. Laget, New Vistas in Electro-Nuclear Physics, Vol 142 of Nato Advanced study Institute, Series B
- [39] J.K.A. Aniol *et al.*, Phys. Rev. C 33, 1714 (1986)
- [40] K. Baba, Nucl. Phys. 444 (1986) 578.
- [41] J. Ahrens, Nucl. Phys. A446 (1985) 229c.
- [42] I. Anthony *et al.*, NIM A301 (1991) 230.
- [43] S.J. Hall, G.J. Miller, R. Beck and P. Jennewein, NIM A368 (1996) 698.
- [44] S.J. Hall and G.J. Miller, Kelvin Lab Annual Report 1990, pp 35-38.
- [45] I.J.D. MacGregor *et al.*, NIM A382 (1996) 470-489
- [46] J.R.M. Annand *et al.*, NIM A368 (1996) 385-391
- [47] T. Hehl *et al.*, NIM A354 (1995) 505
- [48] G.E. Cross University of Glasgow, PhD Thesis (1994)
- [49] W. Braunschweig *et al.*, NIM 134 (1976) 261.
- [50] G.J. Miller *private communication.*
- [51] T.H. Yau, University of Glasgow, PhD Thesis (1996)
- [52] S.N Dancer, University of Glasgow, PhD Thesis (1987).

- [53] R. Madey, Phys. Rev. 85 (1952) 410.
- [54] D.P. Watts, PhD Thesis to be submitted
- [55] T. Hehl *private communication*.
- [56] T. Lamparter *private communication*
- [57] D.F. Measday and C. Richard-Serre, CERN 69-17 (1969).
- [58] D.F. Measday and R.J. Schneider, NIM 42 (1966) 26
- [59] R. Schneider *private communication*
- [60] S. Franczuk *private communication*.
- [61] P.D. Harty *private communication*.
- [62] K. Watson, Phys. Rev. 88 (1952) 1163

